Dynamic Contact and Friction Study of Homogeneous and Layered Media

by

Jian Yang

BS (Beijing University, China) 1995
MS (Peking University, China) 1998

A dissertation submitted in partial satisfaction of the

requirements of the degree of

Doctor of Philosophy
in

Engineering–Mechanical Engineering

in the

GRADUATE DIVISION

of the

UNIVERISTY OF CALIFORNIA, BERKELEY

Committee in charge:

Professor Kyriakos Komvopoulos, Chair
Professor Panayiotis Papadopoulos
Professor Robert O. Ritchie

Fall 2004

The dissertation of Jian Yang is approved:

_____

Chair Date

_____

Date

_____

Date

University of California, Berkeley

Fall 2004

Dynamic Contact and Friction Study of Homogeneous and Layered Media

by

Jian Yang

Abstract

Dynamic Contact and Friction Study of Homogeneous and Layered Media

by

Jian Yang

Doctor of Philosophy in Engineering–Mechanical Engineering

University of California, Berkeley

Professor Kyriakos Komvopoulos, Chair

The principal objective of this dissertation was to develop both analytical and finite element models of contact and friction phenomena encountered over a broad range of length scales, from the atomic level to the macroscopic level. This was accomplished by developing continuum and discrete material models of the deforming media (homogeneous or layered) and the use of scale-invariant (fractal) parameters for the description of the interface topography to preserve self-affinity throughout the range of lengths where a probabilistic (fractal) approach was employed. The specific accomplishments of this work are the following.

Dynamic contact and friction analyses of homogeneous and/or layered media were performed using numerical and analytical methods. The dynamic response of homogeneous and layered media subjected to contact loads and the dependence of the coefficient of friction on load, contact geometry, and material parameters were examined. Most studies were based on continuum mechanics models, while atomic-scale friction

was studied by molecular dynamics simulations, suitable for atomic-/nano-scale mechanics analysis.

Using the finite element method and a dimensional analysis, dynamic impact of an elastic homogeneous medium by a rigid sphere (3-D axisymmetric analysis) or cylinder (2-D plane-strain analysis) moving at a constant speed was studied. The various waves propagating in the media were considered in the dynamic contact simulations. An abrupt increase in the mean contact pressure was found at the time of initial contact. The corresponding initial mean contact pressure was found to be proportional to the indentation speed. Similar results were obtained for a layered medium within a short period after initial contact (i.e., small interference), provided the wave fronts were confined within the first layer, in which case the medium behaves like a homogeneous one.

Finite element solutions of a multi-layered medium subjected to dynamic contact loads were also performed for relatively large interferences. The indenter profile was characterized by either a smooth, cylindrical (chapter 3) or rough, fractal (chapter 4) surface. The requirement for the finite element mesh size in order to obtain results that are not biased by the waves reflected from the artificial boundaries of the half-space was studied. The dependence of the contact force/pressure and subsurface stress/strain fields on the indentation speed, indenter radius (or radius of curvature of the asperities), and overcoat thickness is elucidated. The possibility for excessive plastic flow and crack initiation is examined in terms of the maximum equivalent plastic strain and maximum tensile (first principal) stress. The effect of the surface-layer thickness and cyclic loading

is also investigated for the case of a multi-layered medium subjected to dynamic contact with a rough (fractal) surface.

Static friction between rough surfaces was studied based on an analytical approach. The surface profiles were characterized by fractal geometry, and a theoretical treatment was developed using a piece-wise power-law size distribution and a normal slope distribution of the asperity contacts. Normal and friction forces were obtained for constant interfacial shear strength and negligible interaction between neighboring contact spots. The variation of the static coefficient of friction with normal load is interpreted in the context of analytical results. The dependence of the friction coefficient on interfacial shear strength and surface topography parameters is discussed, and the regime where the friction coefficient assumes a minimum is determined from simulation results.

Molecular dynamic simulations were performed in order to examine the friction coefficient dependence on the tip-substrate interference and tip shape and size. For simplicity, a diamond tip and a face-centered-cubic copper-like substrate were employed. The friction coefficient was found to be quite sensitive to the tip-substrate interference for a prismatic flat tip, but relatively insensitive for a pyramidal sharp tip. In addition, lower friction coefficients were obtained with a larger tip-base area and for edge-front tip sliding.

The findings of this dissertation provide new insight into the tribological behavior of homogeneous and multi-layered media. In particular, the dynamic response of homogeneous and multi-layered media subjected to contact loads, the dependence of the friction coefficient on surface topography and material properties, and the tip size and shape effects on atomic-scale friction anisotropy were examined in light of finite element,

analytical, and molecular dynamics results. Most results are relevant to general engineering components, especially those for multi-layered media are of particular significance to thin-film media used in hard disk drives.

_____

Professor Kyriakos Komvopoulos

Dissertation Chair

TABLE OF CONTENTS

LIST OF FIGURES

Chapter 2

Chapter 3

Chapter 4

Chapter 5

Chapter 6

LIST OF TABLES

ACKNOWLEDGEMENTS

I would like to express my most sincere gratitude to my advisor and dissertation committee chair, Professor Kyriakos Komvopoulos, for his guidance, encouragement, and support throughout my graduate studies. His technical and editorial advice was essential to the completion of this dissertation and has taught me a lot about academic research. I will benefit from what I learned from him throughout my life.

My great appreciation also goes to the members of my dissertation committee, Professor Panayiotis Papadopoulos and Professor Robert O. Ritchie for providing many valuable comments to this dissertation and correcting major and minor inaccuracies in text. I am grateful to the members of my qualifying exam committee, Professor Panayiotis Papadopoulos, Professor David J. Steigmann, Professor C. K. Hari Dharan and Professor Jan M. Rabaey for helping in my academic progress in Berkeley.

I would thank my friends and labmates, Dr. Wentao Yan, Dr. Wei Lu, Dr. Ning Ye, Dr. Lior Kogut, Dr. Zhing-Qing Gong, Dujiang Wan, Rui Xu, Jing Zhou and Dr. Xinjiang Shen for valuable discussions on my research and/or course work.

Last, but not least, I would like to thank my wife Ru Ye for her understanding, patience and love and my parents for their moral and financial support for many years. I hope this is my first step of fulfilling the wishes of my family members.

This research is supported in part by the National Science Foundation, the Computer Mechanics Lab at the University of California, Berkeley, and the National Storage Industry Consortium (NSIC), Extremely High Density Recording (EHDR) program.

CHAPTER 1

Introduction

The study of contact and friction of interacting bodies is a traditional field in continuum mechanics and of critical importance in many engineering applications, especially those involving components undergoing intimate surface interactions, such as gears, bearings, breaks, switches, relays, and guidewires. Contact analysis is advantageous for understanding the tribological behaviors (including wear, friction, and lubrication) of these components. The first seminal contact analysis of elastic curved bodies was presented by Hertz in 1882. Since then, significant progress has been encountered in static contact mechanics for both elastic and elastic-plastic media. However, mechanics studies of dynamic contact problems are relatively limited and most of them have been performed in recent years, presumably due to the complexity of analytical and numerical treatments. Beginning from 1970's, the emergence of high-performance computers in conjunction with advances in numerical methods, mainly finite element method, has provided powerful computational tools for contact studies. Numerical analyses greatly improved the understanding of the dynamic response of contacting media including the subsurface stress and strain fields and contact pressure distribution.

One of the most important findings is that contact loading can produce rather high stresses in a region near the surface, which may lead to mechanical failure due to excessive plastic flow, fracture, or cyclic fatigue. Consequently, in modern engineering

applications, hard and tough overcoat layers are generally used to improve the tribological properties of interacting surfaces and protect the components from excessive inelastic deformation and cracking. This resulted in the divergence of the research attention to contact problems involving layered medium. These problems are quite complex, and analytical solutions are cumbersome to obtain, especially for elastic-plastic contact behaviors involving both geometry and material nonlinearities.

The problems become even more complex in micro-/nano- scale studies, since all solid surfaces, no matter how they are formed, are rough, and the roughness effect cannot be ignored in contact analyses performed at the micro-/nano-scale. Traditionally, rough surfaces have been characterized by statistical parameters, such as surface height variance, skewness, and kurtosis. However, a major disadvantage in these approaches is the use of statistical parameters that are scale-dependent. In recent years, lots of engineering surfaces have been found to exhibit random and self-affine features. Consequently, in contemporary contact mechanics analyses, fractal geometry, which is based on scale-independent parameters, has been used to describe the surface topography.

When two bodies are brought into contact, a finite lateral force is required to initiate relative motion in the horizontal direction. This is known as friction, which can be classified into two categories (i.e., dynamic and static friction) depending on whether relative displacement occurs at the contact interface. This force inhibits the relative movement between the contacting bodies and is referred to as the friction force. The ratio of the friction and normal forces is termed the coefficient of friction, and its magnitude depends on adhesion, surface roughness, deformation, and sliding speed (for dynamic friction only). Friction behavior is rather complex due to the interdependence of the

previous mechanisms. Only limited analytical models have been implemented, and all involve major simplifications in the theoretical treatments.

In view of recent advances in nanotechnology, the demand for fundamental understanding of material behavior at the nanoscale has increased considerably. Since the scale approaches the dimension of atoms, continuum mechanics cannot be used in nanoscale mechanical analyses. Molecular dynamics (MD) is a powerful computational tool for studying nanoscale surface phenomena and instantaneous material properties. It has been used in nano (atomic)-scale contact and friction analyses with great success and has led to fundamental understanding of surface interaction at the atomic (molecular) level.

The objectives of this dissertation were to develop comprehensive dynamic contact analyses for elastic/elastic-plastic homogeneous and/or multi-layered media using the finite element method, and to study the micro-, and nano (atomic)-scale friction behavior of materials by developing a mechanics approach and performing molecular dynamics simulations. A summary of the content of chapters 2-7 is given in the following paragraphs.

Chapter 2 presents a finite element analysis of the impact of a rigid sphere/cylinder moving at a constant velocity on an elastic homogeneous half-space. Frictionless dynamic contact was modeled with special contact elements at the half-space surface. A dimensionless parameter, β, was introduced to study the effect of wave propagation on the deformation behavior. Similar results were obtained for both axisymmetric (spherical indenter) and plane strain (cylindrical indenter) analysis. It is shown that, for small surface interference ($\beta \leq 1$), the front of the faster propagating

dilatational waves extends up to the contact edge, the real contact area is equal to the truncated area, and the contact pressure distribution is uniform. However, for large surface interference ($\beta > 1$), the dilatation wave front extends beyond the contact edge, the real contact area is less than the truncated area, and the contact pressure exhibits a Hertzian-like distribution. The mean contact pressure increases abruptly at the instant of initial contact, remains constant for $\beta \leq 1$, and increases gradually for $\beta > 1$. Based on finite element results for the subsurface stress, strain, and velocity fields, a simple theoretical model that yields approximate closed-form relationships for the mean contact pressure and kinetic and strain energies of the half-space was derived for small surface interference ($\beta \leq 1$), and its validity was confirmed by favor comparisons with finite element results.

A plane-strain analysis of dynamic indentation of an elastic-plastic multi-layered medium by a rigid cylinder is presented in chapter 3. Conversely to plane-strain static contact analysis, the solutions of a dynamic contact analysis within a subsurface domain adjacent to the contact region are independent of mesh size, provided the mesh dimensions are sufficiently large such that the propagating waves reflected from the artificial mesh boundaries do not reach the domain of interest during the analysis. Simulation results for the normal force, contact pressure distribution, subsurface stresses, and evolution of plasticity in a multi-layered medium are presented in terms of the speed and radius of the rigid indenter. The likelihood of mechanical failure due to excessive plastic deformation and cracking is interpreted in terms of finite element results for the von Mises equivalent stress, first principal stress, and equivalent plastic strain obtained for different values of the indenter speed and radius of curvature.

Chapter 4 consists of a finite element analysis of dynamic indentation of an elastic-plastic multi-layered medium by a rigid, rough surface exhibiting fractal behavior. Simulation results illustrate the effects of the layer thickness and indentation speed on the contact load, contact pressure distribution, and subsurface stress and strain fields. The possibility of elastic shakedown is discussed in terms of the evolution of plasticity in the multi-layered medium during repeated loading. The finite element analysis provides insight into the importance of indentation speed, overcoat thickness, and surface topography on the mechanical response of multi-layered media subjected to dynamic contact by rough surfaces.

In chapter 5, a theoretical treatment of static friction is developed for rough surfaces with topographies exhibiting fractal behavior, which is characterized by a piece-wise power-law size distribution and a normal slope distribution of the asperity contacts. Solutions for the normal and friction forces are obtained for constant interfacial shear strength and negligible interaction between neighboring contact spots. The variation of the static coefficient of friction with normal load is interpreted in the context of analytical results. For light loads, deformation at contact spots is predominantly plastic and the friction coefficient decreases with the increase of the normal load. Alternatively, for high loads, the majority of asperity contacts deform elastically and the friction coefficient increases with normal load. The dependence of the static coefficient of friction on interfacial shear strength and surface topography parameters is discussed, and the regime where the friction coefficient assumes a minimum is determined from simulation results.

Chapter 6 presents molecular dynamics simulations of a diamond tip sliding on a face-centered-cubic, copper-like substrate, illustrating the friction coefficient dependence

on the tip-substrate interference and tip shape and size. For a prismatic flat tip, the friction force is mainly due to interactions of atoms at the front face of the tip and substrate atoms ahead of the tip, while the normal force is due to interactions of atoms on the flat surface of the tip and substrate atoms under the tip. However, for a pyramidal sharp tip, both normal and friction forces are mainly due to interactions between atoms at the front surface of the tip and substrate atoms in the vicinity of the sliding tip. Consequently, the friction coefficient is either sensitive (prismatic flat tip) or insensitive (pyramidal sharp tip) to the tip-substrate interference distance. In addition, tip size and orientation effects on the friction coefficient were observed with the prismatic flat tip. Lower friction coefficients were obtained with a larger tip-base area and edge-front tip sliding. Simulation results provide insight into the tip size and shape effects on atomic-scale friction anisotropy.

Finally, chapter 7 provides a summary of the main findings reported in chapters 2-6.

CHAPTER 2

Impact of a Rigid Sphere and Rigid Cylinder on an Elastic Homogeneous Half-Space

2.1 Introduction

Since the seminal elastic contact analysis of curved bodies presented by Hertz (1882), significant progress has been encountered in elastostatic contact mechanics (Johnson, 1985). However, mechanics studies of dynamic contact problems have been mostly performed in recent years, presumably due to the complexity of analytical treatments and the intensive numerical calculations requiring powerful computers. Previous dynamic studies provided insight into the movement and adhesion of impinging particles and information about the coefficient of restitution and the energy dissipated due to particle impact. For instance, Brach and Dunn (1992) presented a mathematical study of the impact and adhesion of microspheres, Wall et al. (1990) measured the kinetic energy loss for particles impacting a surface, and Rogers and Reed (1984) and Johnson and Pollock (1994) investigated adhesion effects in the impact of particles and elastic spheres, respectively. Despite valuable information derived from earlier dynamic studies, very little is known about the evolution of the subsurface stresses and strains, especially in the early stage of impact when the indentation depth is small.

Analytical approaches for dynamic contact problems are quite complex and closed-form solutions are cumbersome. Nevertheless, Bedding and Willis (1973) obtained analytical solutions for the elastodynamic mixed boundary value problem of an elastic half-space indented by a conical or wedge-shaped rigid indenter. The same authors

also examined the problem of a fast moving indenter causing the contact area to expand faster than the propagating dilatational waves (Bedding and Willis, 1976). Brock (1978) studied frictionless indentation of an elastic half-space by an elastic and relatively blunt punch under the assumption of subcritical and constant growth rate of the contact strip. Brock and Georgiadis (1994) presented a dynamic analysis of a linear-elastic half-plane indented by a rapidly moving parabolic or wedge-shaped rigid punch and obtained numerical results for the tangential displacement along the interface and the growth rate of the contact zone.

In addition to analytical methods, numerical and experimental approaches have also been used to study wave propagation in dynamic contacts and to determine the stress and strain fields in impacting bodies. Aboudi (1977) presented a two-dimensional numerical analysis of dynamic contact between a rigid indenter and an elastic half-space, and derived solutions for a wedge-shaped die and a smooth parabolic punch. Using dynamic photoelasticity, Shukla and Rossmanith (1986) investigated experimentally wave propagation across dynamic contacts. Streator (2003) performed a numerical dynamic analysis of adhesive contact between a rigid sphere and an elastic half-space and observed a non-Hertzian contact pressure distribution with peak pressure significantly higher than that predicted by the Hertz theory.

Although comprehensive analyses of dynamic contact was performed in previous studies, subsurface stress and strain solutions for small interferences, i.e., within a short time after the establishment of contact, have not been reported yet. Hence, the main objective here is to analyze impact of an elastic half-space by a rigid sphere using the finite element method and to obtain solutions for the contact area, contact pressure, and

subsurface stresses and strains for small surface interferences. Since surface adhesion is not considered in this analysis, the obtained results are relevant to contact interfaces characterized by weak adhesion forces (e.g., low surface energy materials and boundary-lubricated interfaces) and/or macroscopic contacts for which the effect of surface adhesion forces is secondary. To accomplish the previous objectives, axisymmetric and plane-strain contact models (i.e., spherical and cylindrical indenter, respectively) were developed. Approximate relationships for the mean contact pressure and the strain and kinetic energies of the half-space are derived from a dimensional analysis and an energy-based analytical approach, respectively. Results from the approximate analysis are contrasted with finite element solutions in order to evaluate the accuracy of the analytical relationships and to check the validity of the basic assumptions. It is worthwhile to point out that the results obtained with axisymmetric and plane-strain models exhibit strong similarity for small surface interferences.

2.2 Dimensional Impact Analysis

The solutions of dynamic elastic contact problems depend on the elastic modulus, E, Poisson ratio, ν, and density, ρ, of the half-space. In view of the marginal effect of friction in normal contact (Komvopoulos, 1988), frictionless impact was modeled for simplicity. Based on dimensional analysis (Barenblatt, 1987; Cheng and Cheng, 1998), the mean contact pressure, p_m, can be related to the material properties (E, ν, and ρ), sphere (cylinder) radius, R, indentation speed, V_i, and surface interference, δ, i.e., $p_m = \phi(E, \nu, \rho, V_i, \delta, R)$ or $p_m = \psi(\lambda + 2G, \nu, c_P, V_i, \delta, R)$, where λ and G are the Lamé constants ($\lambda = E\nu/[(1+\nu)(1-2\nu)]$ and $G = E/[2(1+\nu)]$), and c_P is the speed of the plane

dilatational wave propagating in the elastic half-space ($c_P = [(\lambda + 2G)/\rho]^{1/2}$). Three of the governing parameters, λ+2G, c_P, and R, have independent dimensions. The dimensions of p_m, ν, V_i, and δ are:

$[p_m] = [\lambda + 2G]$,

$[\nu] = [\lambda + 2G]^0 [c_P]^0 [R]^0$,

$[V_i] = [c_P]$,

$[\delta] = [R]$,

where [..] indicates dimension. Based on the Π-theorem of dimensional analysis (Barenblatt, 1987), the following relationship was obtained:

$$\frac{p_m}{\lambda + 2G} = \Pi_1\left(\frac{V_i}{c_P}, \frac{\delta}{R}, \nu\right). \tag{2.1}$$

A similar relationship was derived for the real contact radius (half contact length), a, i.e.,

$$\frac{a}{R} = \Pi_2\left(\frac{V_i}{c_P}, \frac{\delta}{R}, \nu\right) \tag{2.2}$$

In the following sections, Π_1 and Π_2 functions are determined for small surface interference from finite element results.

2.3 Finite Element Model

Wave propagation in elastic media plays an important role in dynamic contact analysis. Both bulk and surface waves can propagate in semi-infinite solids. Bulk waves include dilatational waves (characterized by a volume change) and shear waves (Pollard,

1977). The propagation speeds of plane dilatational and shear waves, c_P and c_S, respectively, are related to the material properties of the elastic half-space by

$$c_P = \left(\frac{\lambda + 2G}{\rho} \right)^{1/2} \quad \text{and} \quad c_S = \left(\frac{G}{\rho} \right)^{1/2} .$$

For steels and copper, c_P is equal to 5900 and 4600 m/s, respectively, while c_S is equal to 3200 and 2300 m/s, respectively (Johnson, 1985). Obviously, plane dilatational waves propagate faster than plane shear waves. In addition, surface waves, such as Rayleigh and Love waves, may propagate along the free surface of the half-space. In general, surface waves propagate at speeds comparable to those of plane shear waves (Beltzer, 1988).

Figure 2.1 shows schematically global dilatational wave fronts, which are envelopes of a series of spherical (cylindrical) dilatational wave fronts. These spherical (cylindrical) waves initiate at surface nodal points at the instant of initial contact with the rigid sphere (cylinder). The newly established contact points become centers of spherical wave fronts. As shown in Fig. 2.1(a), for small surface interference, the dilatational wave front is confined below the contact region. Since the displacement at any material point ahead of the wave front is zero, the contact radius (half-contact length), a, is equal to the truncated radius (half-truncated length), a', which can be approximated by $a' \approx (2R\delta)^{1/2}$ when $\delta << R$. A dimensionless parameter, β, is defined as

$$\beta \equiv \frac{c_P}{V_i} k \approx \frac{c_P}{V_i} \left(\frac{2\delta}{R} \right)^{1/2} , \tag{2.3}$$

where $k \approx a'/R$ is the tangent slope of the rigid sphere (cylinder) at the edge of the truncated contact area. When $\beta < 1$, the contact area spreads faster than the dilatational wave (Fig. 2.1(a)), whereas the opposite occurs when $\beta > 1$ (Fig. 2.1(b)), i.e., the

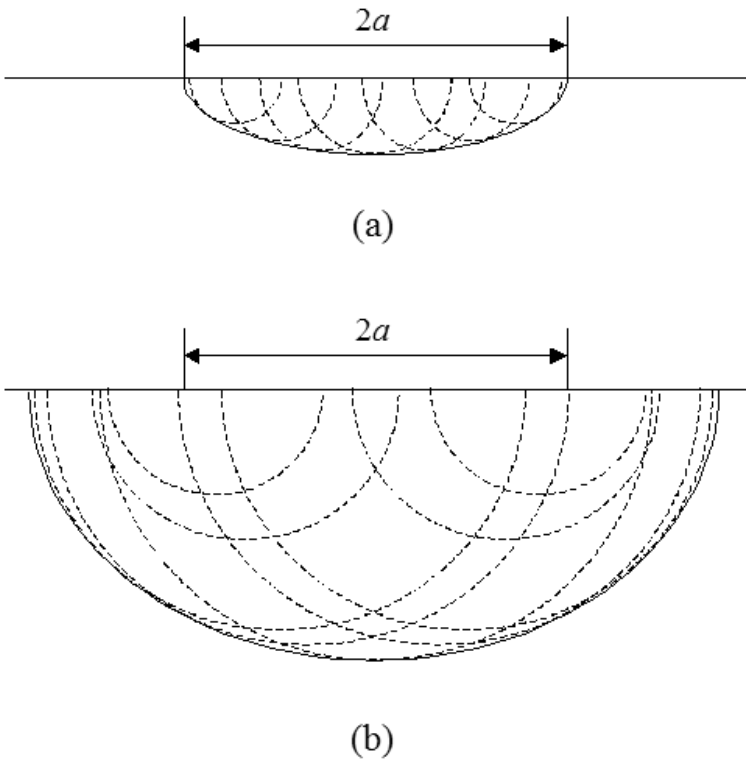

Fig. 2.1 Schematic representation of propagation of dilatation waves in a semi-infinite half-space due to impact of a rigid sphere (cylinder) for (a) small and (b) large surface interference. The solid curves are envelopes of the spherical wave fronts.

dilatational wave front is no longer confined below the contact region. When $\beta > 1$, the real contact area is smaller than the truncated contact area due to the downward movement of the surface in the vicinity of the contact edge. In the special case of quasi-static contact ($V_i \to 0$), $\beta \to \infty$ and the real contact area is less than the truncated contact area.

In view of the previous discussion, it may be inferred that a layered medium impacted by a rigid sphere (cylinder) should yield a behavior similar to that of a homogeneous medium with material properties those of the surface layer of the layered

medium only during the time that the dilatational wave front resides within the surface layer. Therefore, the present analysis for small interference distances is also applicable to elastic layered media.

Impact simulations were performed with the finite element code ABAQUS. For increased accuracy and better convergence, the ABAQUS/Standard package (i.e., implicit integration) rather than the generally faster ABAQUS/Explicit package (i.e., explicit integration) was used. Contact of the rigid sphere (cylinder) with the elastic homogeneous half-space was modeled by a rigid surface and special contact elements, i.e., first-order, axisymmetric (plane-strain), rigid-surface elements, which are suitable for modeling contact between axisymmetric (plane-strain) elements and a rigid surface. The contact elements were assigned to a common reference node in order to define the motion of the rigid surface. Impact was modeled by advancing the rigid surface against the deformable mesh at constant speed using a displacement-control incremental scheme. The time increment was automatically adjusted in order to satisfy the convergence requirement. Because of this scheme and the assumption of a rigid sphere (cylinder), the effects of the sphere (cylinder) mass and wave propagation in the sphere medium on the simulation results were neglected.

The elastic half-space was discretized by four-node, bi-linear, axisymmetric (plane-strain) elements with a 2×2 Gaussian integration scheme. To obtain unbiased dynamic solutions, a sufficiently large mesh must be used in order for the waves reflected from the artificial boundaries not to reach the domain of interest during the time of analysis. In dynamic contact, the displacement at any material point ahead of the dilatational wave front is equal to zero. Since dilatational waves propagate faster than

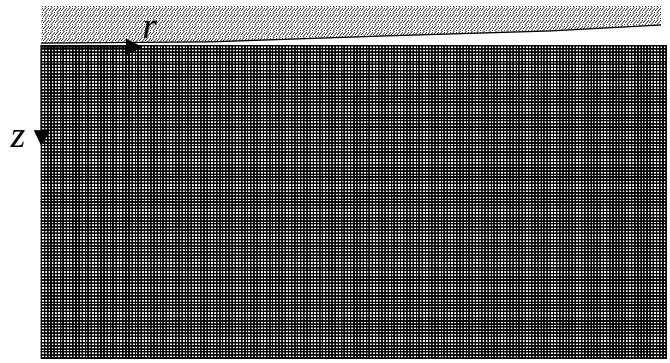

(a)

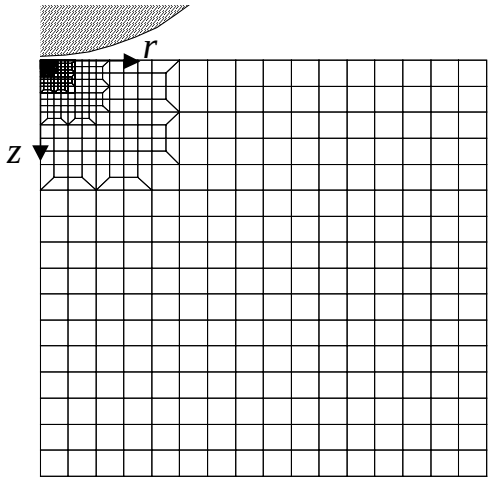

(b)

Fig. 2.2 Finite element meshes of elastic homogeneous half-space impacted by a rigid sphere (cylinder) used in the (a) small and (b) large surface interference simulations.

shear and surface waves, only the dilatational waves were considered in the determination of the appropriate mesh size. However, shear and surface waves were present in the finite element simulations discussed in the following section. Two different finite element meshes were used to perform impact simulations of small ($\beta \leq 1$) and large ($\beta > 1$) surface interferences. Figure 2.2(a) shows the fine mesh used to model a

relatively small domain of the half-space where impact commences ($\beta \leq 1$), and Fig. 2.2(b) shows the mesh used to model a much larger domain, which is less refined in the vicinity of the contact region ($\beta > 1$). The nodes on the symmetry axis ($r = 0$ for axisymmetric and $x = 0$ for plane-strain analysis respectively) and the bottom boundary of the meshes were constrained against displacement in the r (x) and z directions, respectively, while the nodes of the right boundary of the meshes were allowed to move freely. In view of the sufficiently large dimensions of the finite element meshes shown in Fig. 2.2, the effect of the boundary conditions on the results was secondary.

2.4 Results and Discussion for Axisymmetric Analysis

To enable the interpretation of a large number of dynamic contact problems with the same values of important dimensionless parameters, such as $\tilde{V}_i = V_i / c_P$, $\tilde{\delta} = \delta / R$, ν, and β, the finite element and analytical results discussed in this section are presented in dimensionless form. Unless otherwise stated, the solutions discussed in this section are for $\nu = 0.3$. The dilatational wave front, contact pressure distribution, and subsurface stress, strain, and velocity fields are interpreted in the context of finite element and dimensional analysis results.

2.4.1 Dilatational Wave Front and Contact Radius

As mentioned earlier, dilatational waves propagate much faster than shear and surface waves, and therefore all material points ahead of the dilatational wave front are in equilibrium. Insight into the dilatational wave front characteristics can be obtained by examining the displacement contours in the proximity of the contact region. Figure 2.3 shows contours of normalized displacement u_z/δ for different values of β. The

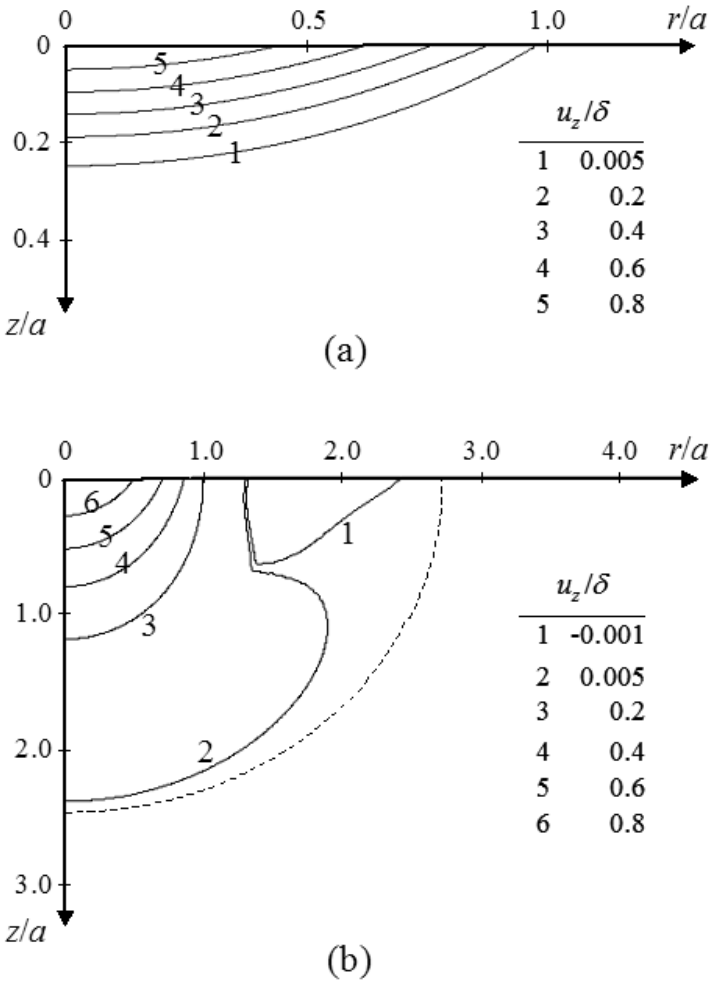

Fig. 2.3 Contours of dimensionless u_z displacement in an elastic homogeneous half-space impacted by a rigid sphere: (a) $\beta = 0.5$ ($\tilde{V}_i = 1 \times 10^{-2}$ and $\tilde{\delta} = 1.25 \times 10^{-5}$) and (b) $\beta = 4.47$ ($\tilde{V}_i = 1 \times 10^{-2}$ and $\tilde{\delta} = 1 \times 10^{-3}$). The dashed curves are envelopes of the spherical wave fronts.

discontinuous lines represent envelopes of the spherical wave fronts, as shown in Fig. 2.1. These envelopes enclose the displacement contours obtained from the finite element analysis. Figure 2.4 presents contours of normalized displacement u_r/δ, which also show that the displacements at material points ahead of the wave front are essentially zero. It

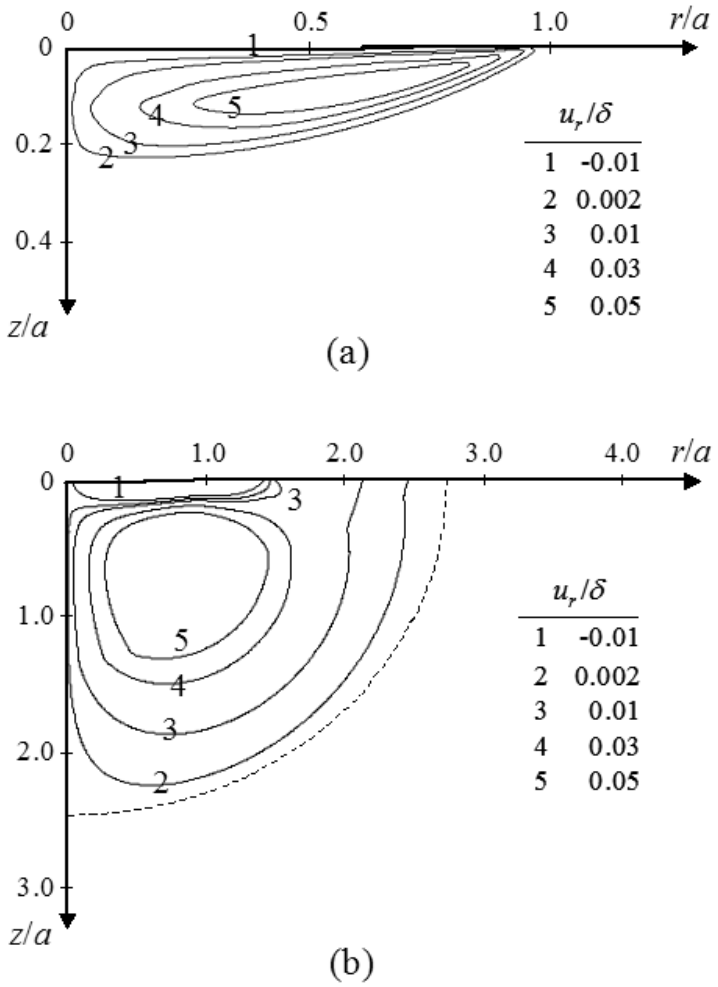

Fig. 2.4 Contours of dimensionless u_r displacement in an elastic homogeneous half-space impacted by a rigid sphere: (a) $\beta = 0.5$ ($\widetilde{V}_i = 1 \times 10^{-2}$ and $\widetilde{\delta} = 1.25 \times 10^{-5}$) and (b) $\beta = 4.47$ ($\widetilde{V}_i = 1 \times 10^{-2}$ and $\widetilde{\delta} = 1 \times 10^{-3}$). The dashed curves are envelopes of the spherical wave fronts.

can be concluded that when the wave front terminates at the contact edge (Figs. 2.3(a) and 2.4(a)) the real contact area is equal to the truncated area, while when the wave front spreads outside the contact region (Figs. 2.3(b) and 2.4(b)) the real contact area is less than the truncated area due to the downward movement of the free surface in the vicinity of the contact edge. Figure 2.5 shows the real-to-truncated contact radius ratio, a/a', as a

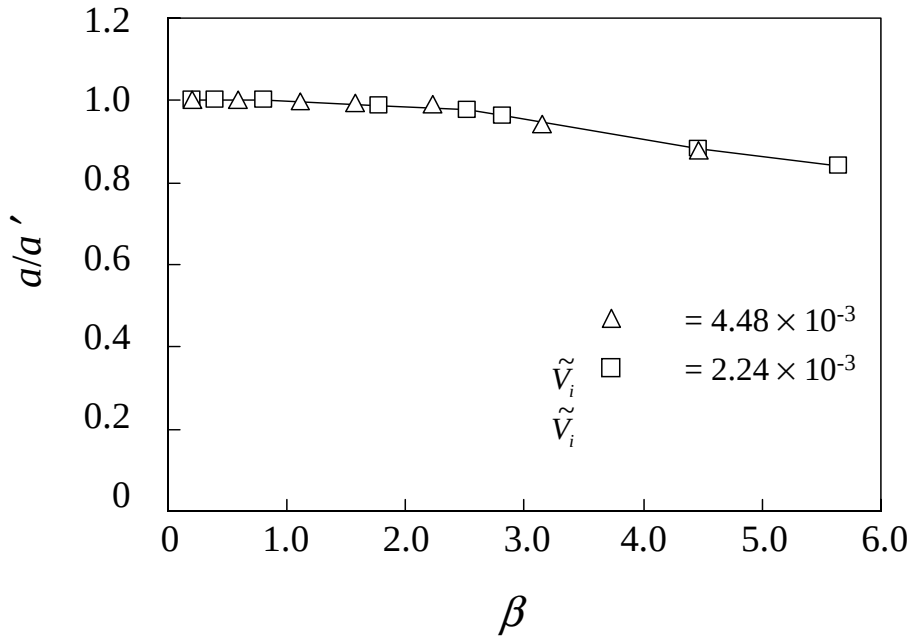

Fig. 2.5 Ratio of real-to-truncated contact radius a/a' versus β for dimensionless indentation velocity $\tilde{V}_i = 2.24 \times 10^{-3}$ and 4.48×10^{-3}.

function of β. It is noted that $a = a'$ when $\beta \leq 1$ and $a < a'$ when $\beta > 1$. In view of the close agreement of the results obtained for $\tilde{V}_i = 4.48 \times 10^{-3}$ and 2.24×10^{-3}, it may be inferred that the area ratio is predominantly affected by β. Therefore, when $\beta \leq 1$ (i.e., small surface interference), Eq. (2.2) can be written as

$$\frac{a}{R} \cong \left(\frac{2\delta}{R} \right)^{1/2} .$$

The results shown in Figs. 2.3-2.5 demonstrate a dependence of the deformation response on the magnitude of β.

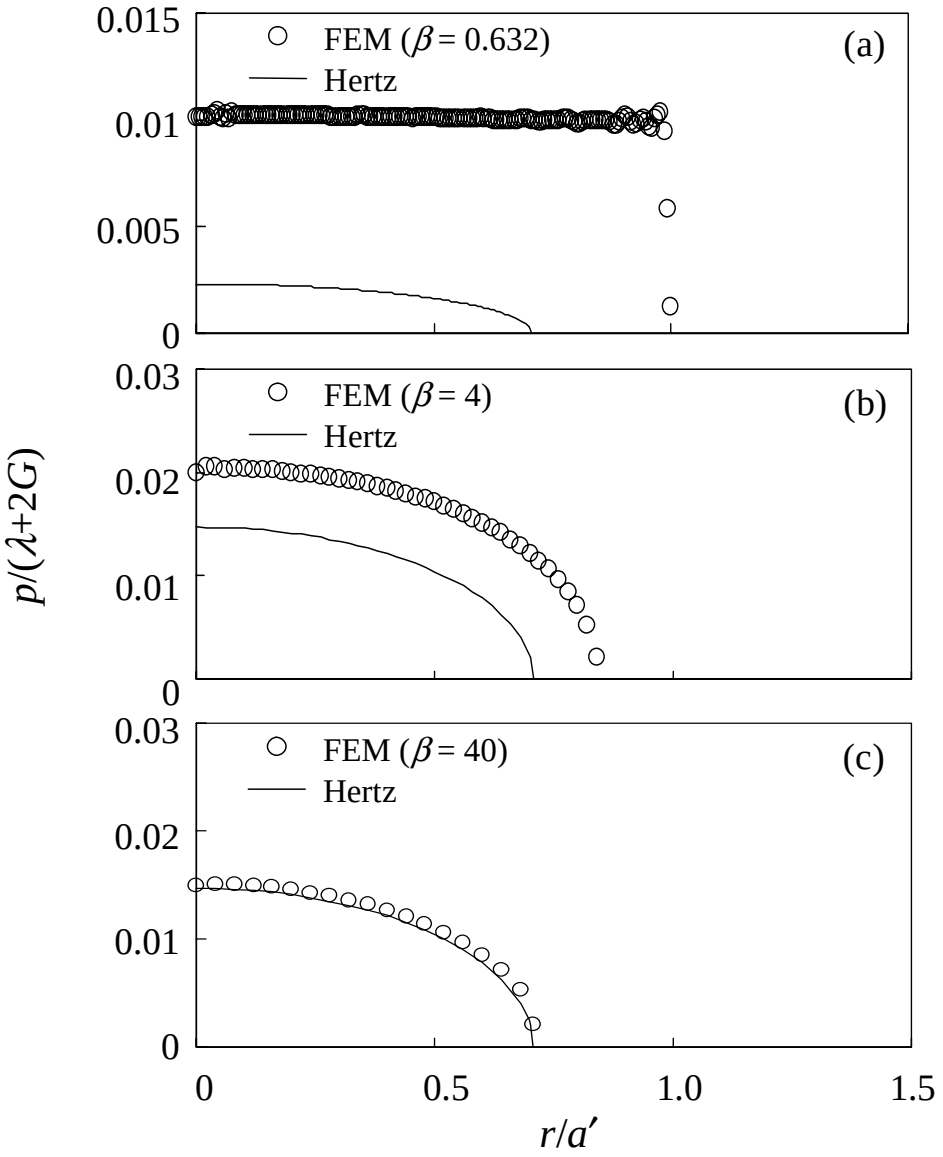

Fig. 2.6 Dimensionless contact pressure distribution for (a) $\beta = 0.632$ ($\tilde{V}_i = 1 \times 10^{-2}$ and $\tilde{\delta} = 2 \times 10^{-5}$), (b) $\beta = 4$ ($\tilde{V}_i = 1 \times 10^{-2}$ and $\tilde{\delta} = 8 \times 10^{-4}$), and (c) $\beta = 40$ ($\tilde{V}_i = 1 \times 10^{-3}$ and $\tilde{\delta} = 8 \times 10^{-4}$). For each pressure distribution, the Hertzian pressure profile obtained for the same surface interference is also shown for comparison.

2.4.2 Contact Pressure

Figure 2.6 shows the dimensionless contact pressure, $p/(\lambda+2G)$, for different values of β. For relatively low β (i.e., $\beta = 0.632$), the contact pressure is fairly uniform

within the contact region and decreases abruptly at the contact edge (Fig. 2.6(a)). This pressure distribution is significantly different from that obtained from the Hertz theory, for the same surface interference. In addition, the real contact radius for dynamic contact, $a \approx (2R\delta)^{1/2}$, is larger than that predicted by the Hertz theory, $a = (R\delta)^{1/2}$. Figure 2.6(a) also shows that the dynamic contact pressure is significantly higher than the static contact pressure (Hertz). Streator (2003) has reported similar findings for dynamic contact of adhesive surfaces. However, the contact pressure distribution in that study exhibited significant fluctuations, presumably due to the adhesive forces at the contact interface, while the pressure profiles shown in Fig. 2.6 are smooth. For relatively high β (i.e., β = 4), the contact pressure exhibits a Hertzian-like distribution; however, the pressure and the contact radius are still larger than those obtained from the static analysis (Fig. 2.6(b)). For very high β (e.g., β = 40), the contact pressure distribution is in good agreement with that predicted by the Hertz theory (Fig. 2.6(c)). Hence, for $\beta >> 1$ (i.e., low indentation speed and/or large surface interference), the dynamic solution approaches the static solution. Figure 2.7 shows the variation of the normalized mean contact pressure, $p_m/(\lambda+2G)$, with β and $\tilde{V}_i$. The mean contact pressure increases abruptly at the instant of contact for both indentation speeds, remains constant for $\beta \leq 1$, and increases gradually with the increase of β in the range of $\beta > 1$. Hereafter, the mean contact pressure upon initial contact will be denoted by p_{m0}. From dimensional analysis (Eq. (2.1)), it is found that

$$\frac{p_{m0}}{\lambda + 2G} = \Pi_3\left(\tilde{V}_i, \nu\right). \tag{2.4}$$

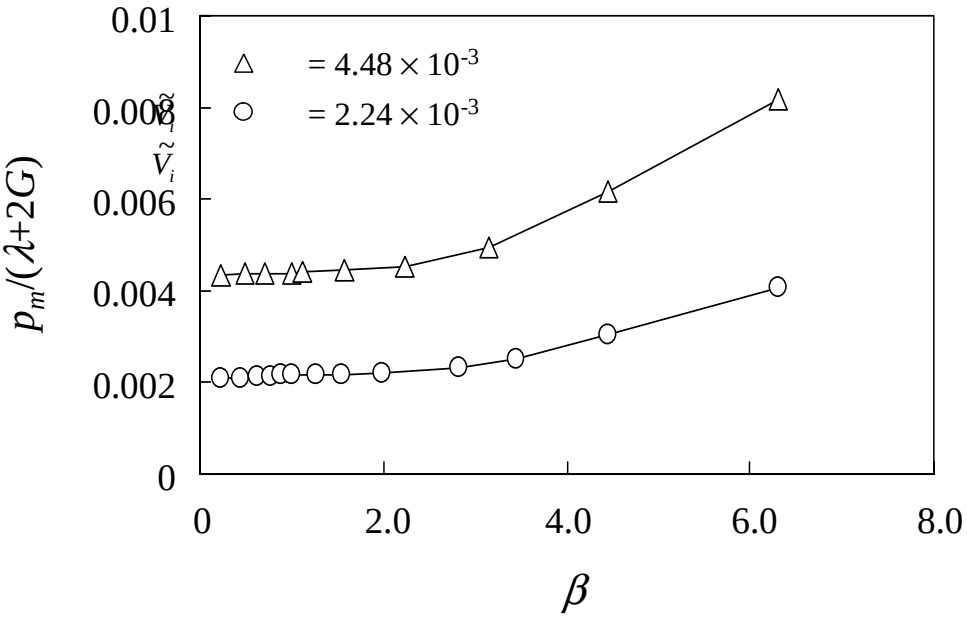

Fig. 2.7 Dimensionless mean contact pressure p_m versus β for dimensionless indentation velocity $\tilde{V}_i$ = 2.24 × 10^{-3} and 4.48 × 10^{-3}.

Because Eq. (2.4) is derived for the instant of impact (i.e., $\tilde{\delta}$=0+), Π_3 is not a function of $\tilde{\delta}$. Since p_m is nearly constant for $\beta < 1$, in the finite element simulations, p_{m0} can be approximated by the value of p_m obtained for small β values ($\beta < 1$). Figure 2.8 shows the dimensionless mean contact pressure at the instant of impact, $p_{m0}/(\lambda+2G)$, as a function of $\tilde{V}_i$ for different values of Poisson ratio. The fact that all the results follow closely the same line with a slope of ~0.97 indicates that p_{m0} is explicitly independent of the Poisson ratio. Therefore,

$$\frac{p_{m0}}{\lambda+2G} \approx 0.97\tilde{V}_i \ , \qquad \text{for } 0.1 \le \nu \le 0.4. \tag{2.5}$$

Since $p_m \approx p_{m0}$ when $\beta \le 1$ (Fig. 2.7), it follows from Eq. (2.5) that

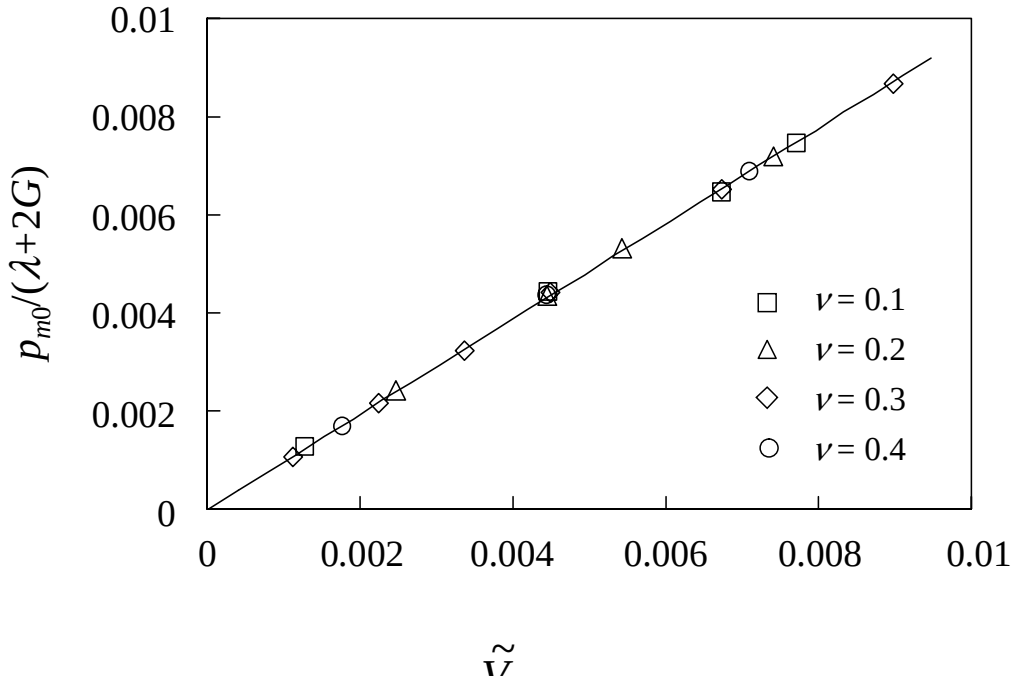

Fig. 2.8 Dimensionless mean contact pressure at the instant of initial contact p_{m0} versus dimensionless indentation velocity $\tilde{V}_i$ for different values of Poisson ratio, ν.

$$\frac{p_m}{\lambda + 2G} \approx 0.97\tilde{V}_i, \qquad \text{for } \beta \le 1. \tag{2.6}$$

2.4.3 Subsurface Stress, Strain, and Velocity Fields

Figures 2.9(a) and 2.9(b) show contours of dimensionless stress σ_{zz}/p_{m0} and strain $\varepsilon_{zz}/\tilde{V}_i$, respectively, for β = 0.447 ($\tilde{V}_i$ = 1 × 10^{-2} and $\tilde{\delta}$ = 1 × 10^{-5}). Both σ_{zz} and ε_{zz} decrease abruptly across the wave front. In the region enclosed by the wave front, σ_{zz} and ε_{zz} are nearly constant and their magnitudes can be approximated by $-p_{m0}$ and $-\tilde{V}_i$, respectively. A similar trend is shown in Fig. 2.10 for the contours of dimensionless velocity $\dot{u}_z/V_i$. In the region near the wave front, $\dot{u}_z$ decreases abruptly, while in the region enclosed by the wave front, $\dot{u}_z$ is uniform and can be approximated by V_i.

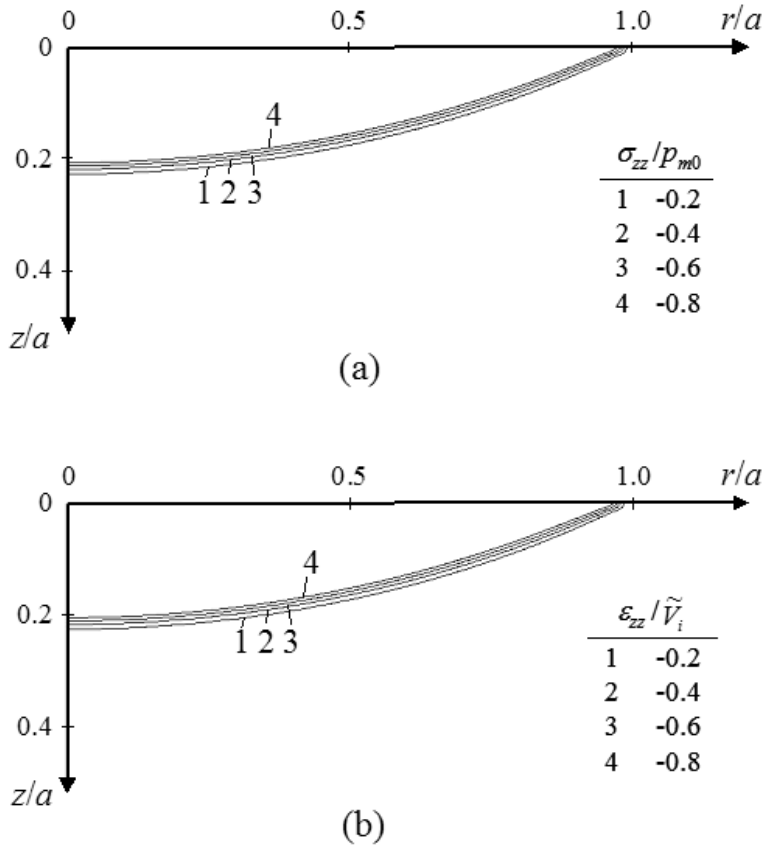

Fig. 2.9 Contours of dimensionless (a) σ_{zz} stress and (b) ε_{zz} strain in an elastic half-space impacted by a rigid sphere for $\beta = 0.447$ ($\tilde{V}_i = 1 \times 10^{-2}$ and $\tilde{\delta} = 1 \times 10^{-5}$).

2.4.4 Approximate Theoretical Model

An approximate energy-based analysis of the impacted elastic half-space is derived in this section for small surface interference ($\beta \leq 1$). According to the finite element results (Figs. 2.9 and 2.10), in the region surrounded by the dilatational wave front, ε_{zz} and $\dot{u}_z$ are approximately equal to $-\tilde{V}_i$ and V_i, respectively. Since impact occurs in the z direction and for small surface interference the waves propagate in a small subsurface region adjacent to the contact interface, it may be assumed that, among all the

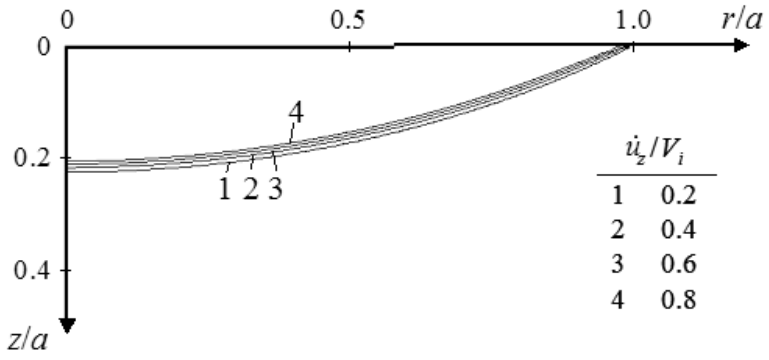

Fig. 2.10 Contours of dimensionless $\dot{u}_z$ velocity in an elastic half-space impacted by a rigid sphere for $\beta = 0.447$ ($\tilde{V}_i = 1 \times 10^{-2}$ and $\tilde{\delta} = 1 \times 10^{-5}$).

strain components, ε_{zz} exhibits the most significant contribution to the strain energy stored in the elastic half-space. The validity of the previous assumptions is demonstrated below. Consequently, if the contribution of all the other strain components is neglected as secondary, the strain energy per unit volume, e_S, in the region where wave propagation occurs can be written as

$$e_S = \frac{1}{2}(\lambda + 2G)\tilde{V}_i^2 . \tag{2.7}$$

The kinetic energy per unit volume is given by

$$e_K = \frac{1}{2}\rho V_i^2 . \tag{2.8}$$

Since $c_P = [(\lambda + 2G)/\rho]^{1/2}$, it can be shown that $e_S = e_K$. The total volume of the region where wave propagation occurs, *U*, can be expressed as $U \approx \pi(R\delta^2 - \delta^3/3)/\tilde{V}_i$. This is because wave propagation in the *z* direction occurs at a speed equal to ~$1/\tilde{V}_i$ times the indentation speed. For $\delta << R$, it follows that $U \approx \pi R\delta^2/\tilde{V}_i$, and the total strain and kinetic energy of the half-space are given by

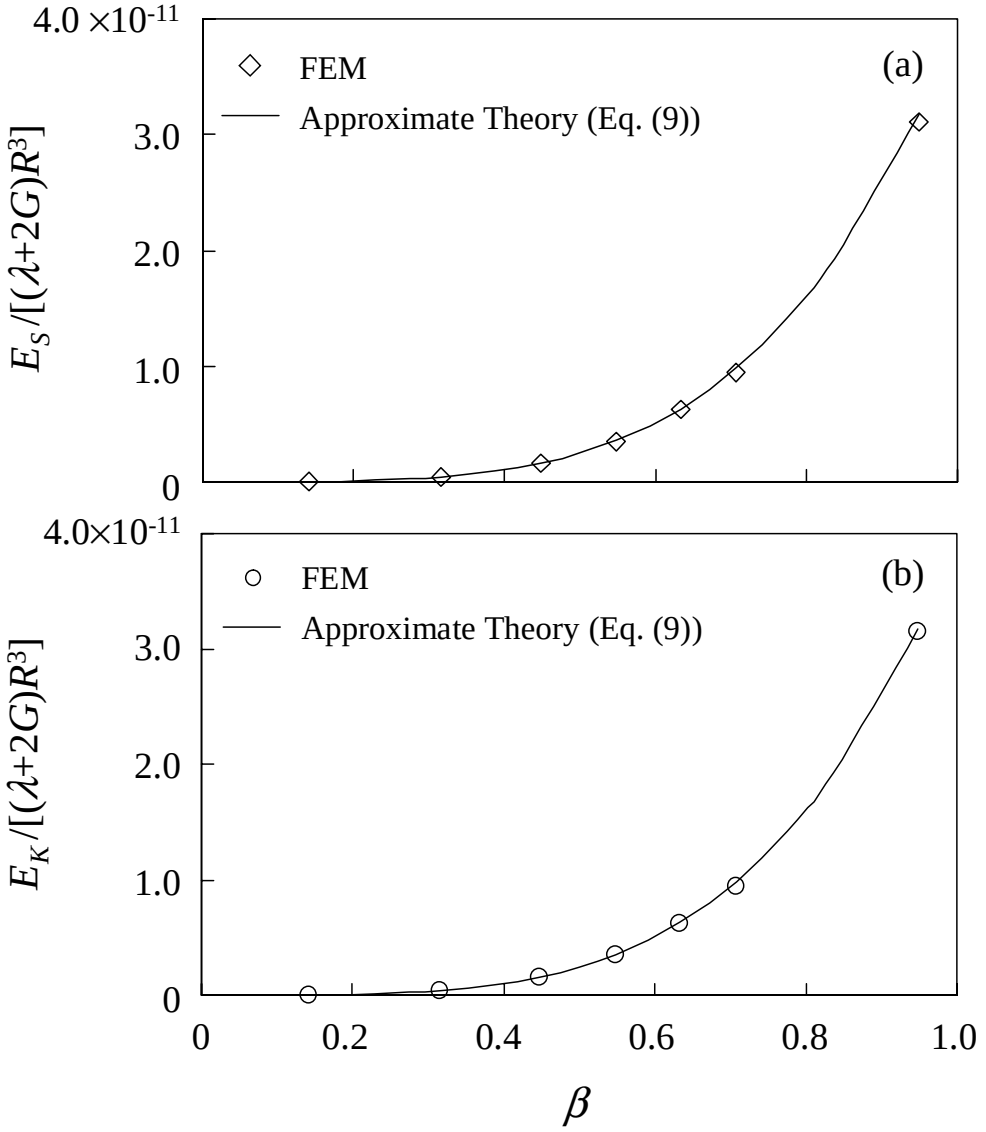

Fig. 2.11 Comparison of finite element method (FEM) results and approximate theory solutions of (a) dimensionless strain energy E_S and (b) dimensionless kinetic energy E_K of an elastic half-space impacted by a rigid sphere versus β for dimensionless indentation velocity $\tilde{V}_i = 1 \times 10^{-2}$.

$$E_S = E_K = \frac{1}{2}(\lambda + 2G)\tilde{V}_i \pi R \delta^2 = \frac{\pi}{8}(\lambda + 2G) R^3 \tilde{V}_i^5 \beta^4 . \tag{2.9}$$

Figure 2.11 shows a comparison between finite element results of total strain and kinetic energy for $\tilde{V}_i = 1 \times 10^{-2}$ and analytical results obtained from Eq. (2.9). The good

agreement indicates that the assumptions invoked in the approximate theoretical model are reasonable and that the simple analysis provides accurate estimates of the total strain and kinetic energy of the half-space for small surface interference.

Based on energy balance considerations, the following relationship must be satisfied,

$$p_m(2\pi R\delta) = \left(\frac{dE_S}{d\delta} + \frac{dE_K}{d\delta} \right). \tag{2.10}$$

Substitution of Eq. (2.9) in Eq. (2.10) gives,

$$\frac{p_m}{\lambda + 2G} = \tilde{V}_i. \tag{2.11}$$

It is interesting to note that Eq. (2.11) is in good agreement with Eqs. (2.5) and (2.6) that were obtained from the finite element analysis.

2.5 Results and Discussion for Plane-Strain Analysis

Finite element solutions for an elastic homogeneous half-space impacted by a rigid cylinder (i.e., plane-strain analysis) are reported in this section. Strong similarity between the results of plane-strain and axisymmetric analyses were found for $\beta < 1$. The dynamic contact analysis results were not compared with those of the static analysis because the plane-strain displacement field for (quasi-) static contact conditions exhibits logarithmic singularity (Johnson, 1985) and, hence, it is not possible to compare the results with those of a dynamic analysis. This will be further discussed in chapter 3 (section 3.2.1).

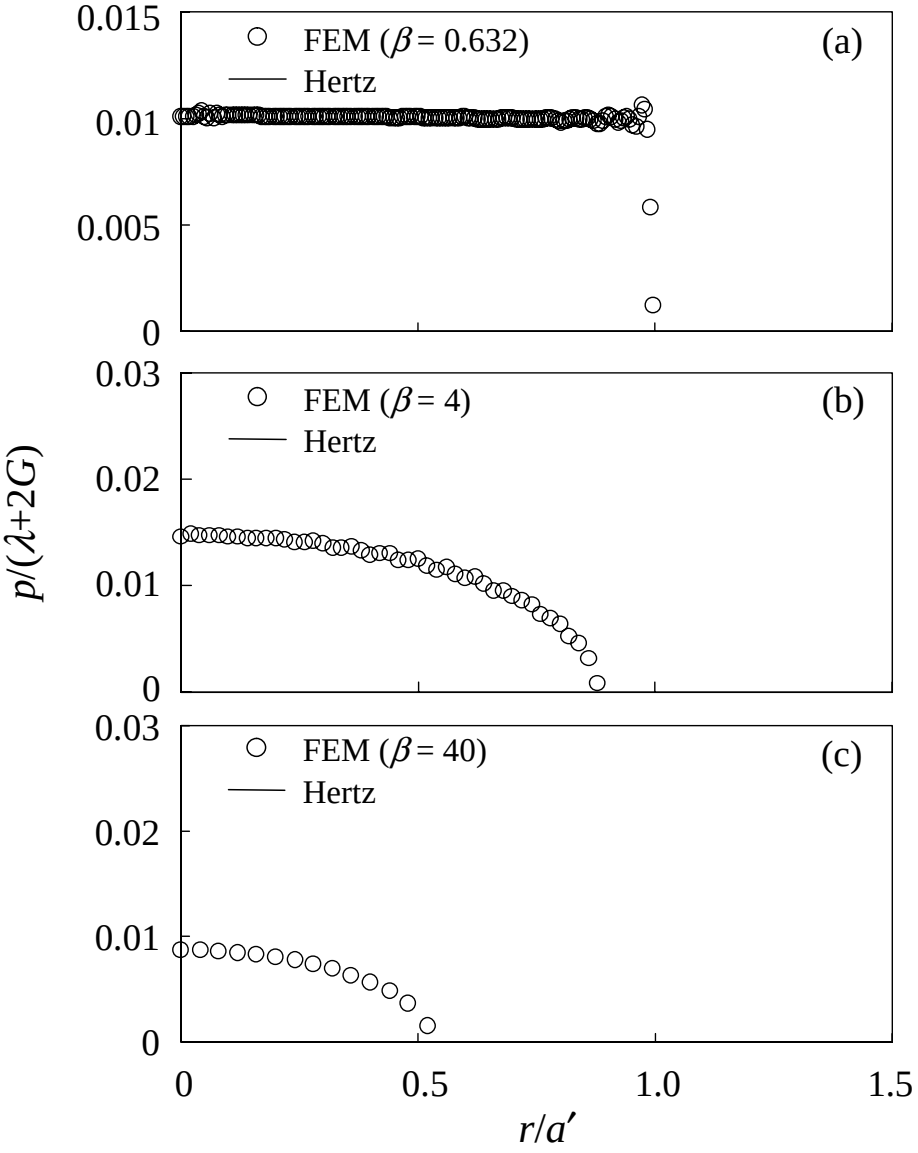

Fig. 2.12 Dimensionless contact pressure distribution along the surface of elastic half-space impacted by a rigid cylinder for (a) $\beta = 0.632$ ($\tilde{V}_i = 1 \times 10^{-2}$ and $\tilde{\delta} = 2 \times 10^{-5}$), (b) $\beta = 4$ ($\tilde{V}_i = 1 \times 10^{-2}$ and $\tilde{\delta} = 8 \times 10^{-4}$), and (c) $\beta = 40$ ($\tilde{V}_i = 1 \times 10^{-3}$ and $\tilde{\delta} = 8 \times 10^{-4}$).

2.5.1 Contact Pressure

The dimensionless contact pressure, $p/(\lambda+2G)$, for different values of β is shown in Fig. 2.12. Similar to axisymmetric analysis, for relatively low β (i.e., $\beta = 0.632$), the

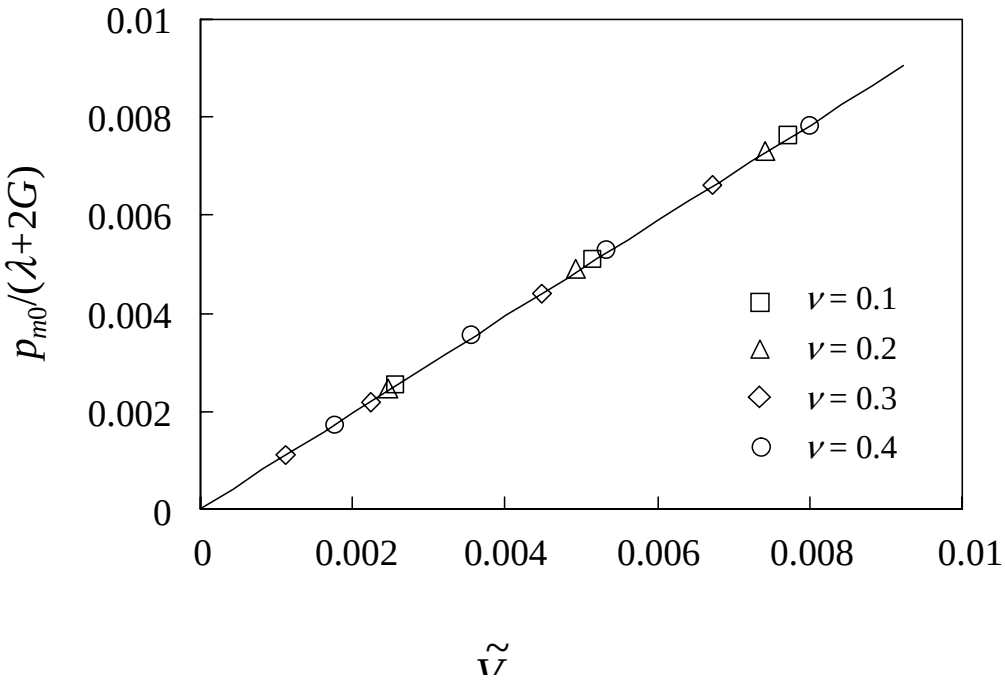

Fig. 2.13 Dimensionless mean contact pressure at the instant of initial contact p_{m0} an obtained for elastic half-space impacted by a rigid cylinder versus dimensionless indentation velocity $\tilde{V}_i$ for different values of Poisson ratio, ν.

contact pressure is fairly uniform within the contact region and decreases abruptly at the contact edge, and the real contact radius is approximately equal to the truncated contact radius (Fig. 2.12(a)). However, for relatively high β values (i.e., β = 4 and 40), the contact pressure exhibits an elliptic distribution, and the real contact radius is smaller than the truncated contact radius (Figs. 2.12(b) and 2.12(c)). Figure 2.13 shows the dimensionless initial mean contact pressure, $p_{m0}/(\lambda+2G)$, as a function of $\tilde{V}_i$ for different values of Poisson ratio. All the results follow closely the same line with a slope of ~0.98 indicating that under plane-strain condition, p_{m0} is also explicitly independent of Poisson ratio. Therefore, under plane-strain condition:

$$\frac{p_{m0}}{\lambda + 2G} \approx 0.98\tilde{V}_i \ , \qquad \text{for } 0.1 \le \nu \le 0.4. \tag{2.12}$$

Equation (2.12) is almost identical to Eq. (2.5).

2.5.2 Subsurface Stress, Strain, and Velocity Fields

Figures 2.14(a), 2.14(b) and 2.14(c) show contours of dimensionless stress σ_{zz}/p_{m0}, strain $\varepsilon_{zz}/\tilde{V}_i$, and velocity $\dot{u}_z/V_i$ respectively, for $\beta = 0.447$ ($\tilde{V}_i = 1 \times 10^{-2}$ and $\tilde{\delta} = 1 \times 10^{-5}$). All of them decrease abruptly across the wave front. In the region enclosed by the wave front, σ_{zz}, ε_{zz} and $\dot{u}_z$ are nearly constant and their magnitudes can be approximated by $-p_{m0}$, $-\tilde{V}_i$, and V_i respectively. Again the close agreement of the results shown in Figs 2.9 and 2.10 and Fig. 2.14 is noted.

2.5.3 Approximate Theoretical Model

Similar to the axisymmetric analysis, it is assumed that in the region surrounded by the dilatational wave front, ε_{zz} and $\dot{u}_z$ are approximately equal to $-\tilde{V}_i$ and V_i, respectively (according to Figs. 2.14), and among all the strain components, ε_{zz} exhibits the most significant contribution to the strain energy stored in the elastic half-space. Consequently, the strain energy per unit volume, e_S, in the region where wave propagation occurs can be written as

$$e_S = \frac{1}{2}(\lambda + 2G)\tilde{V}_i^2 . \tag{2.13}$$

The kinetic energy per unit volume is given by

$$e_K = \frac{1}{2}\rho V_i^2 . \tag{2.14}$$

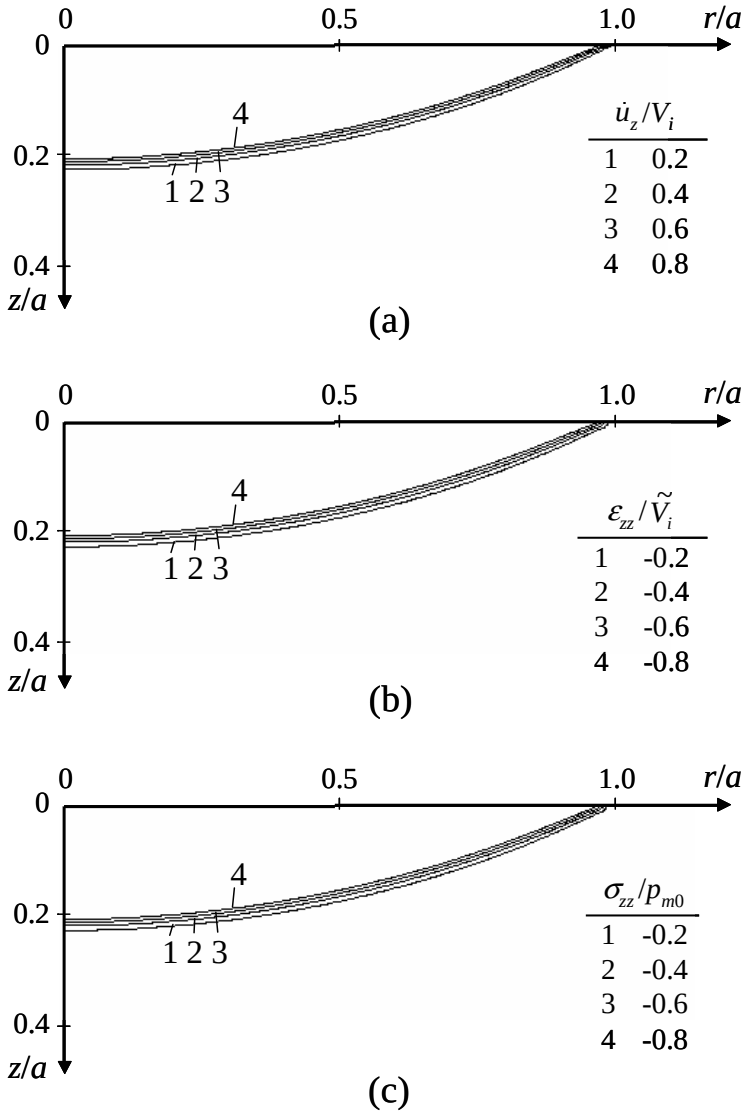

Fig. 2.14 Contours of dimensionless (a) σ_{zz} stress, (b) ε_{zz} strain and (c) $\dot{u}_z$ velocity in an elastic half-space impacted by a rigid cylinder for $\beta = 0.447$ ($\tilde{V}_i = 1 \times 10^{-2}$ and $\tilde{\delta} = 1 \times 10^{-5}$).

The total area of the region where wave propagation occurs, A, can be expressed as $A = R^2 \left[\arccos\left(1-\tilde{\delta}\right) - \left(1-\tilde{\delta}\right)\left(2\tilde{\delta} - \tilde{\delta}^2\right)^{1/2}\right] / \tilde{V}_i$. Therefore, the total strain and kinetic energy of the half-plane are given by

$$E_S = E_K = \frac{1}{2}(\lambda + 2G)\tilde{V}_i R^2 \left[\arccos(1-\tilde{\delta}) - (1-\tilde{\delta})(2\tilde{\delta} - \tilde{\delta}^2)^{1/2}\right]. \quad (2.15)$$

Figure 2.15 shows a comparison between finite element results of total strain and kinetic energy for $\tilde{V}_i = 1 \times 10^{-2}$ and analytical results obtained from Eq. (2.15). The good agreement indicates that the above-mentioned assumptions are also reasonable for plane-strain analysis.

Based on energy balance considerations, the following relationship must be satisfied,

$$p_m(2\pi R\delta) = \left(\frac{dE_S}{d\delta} + \frac{dE_K}{d\delta}\right). \quad (2.16)$$

Substitution of Eq. (2.15) in Eq. (2.16) gives,

$$\frac{p_m}{\lambda + 2G} = \tilde{V}_i \sqrt{1 - \frac{\tilde{\delta}}{2}}\,. \quad (2.17)$$

Therefore, for $\tilde{\delta} << 1$, $\frac{p_m}{\lambda + 2G} \approx \tilde{V}_i$, which is in good agreement with Eq. (2.11).

It is interesting to note that, for small β value ($\beta \leq 1$), the results obtained for axisymmetric (spherical indenter) and plane-strain (cylindrical indenter) analysis show strong resemblance, and the results of normalized contact pressure and subsurface stress, strain and velocity fields are independent to the indenter's radius, *R*, for both analyses, suggesting that similar results could be obtained for impact between any isotropic elastic bodies with smooth surfaces.

As mentioned in section 2.3, although the present analyses are for homogeneous half-space media, the obtained results are also applicable for elastic layered media,

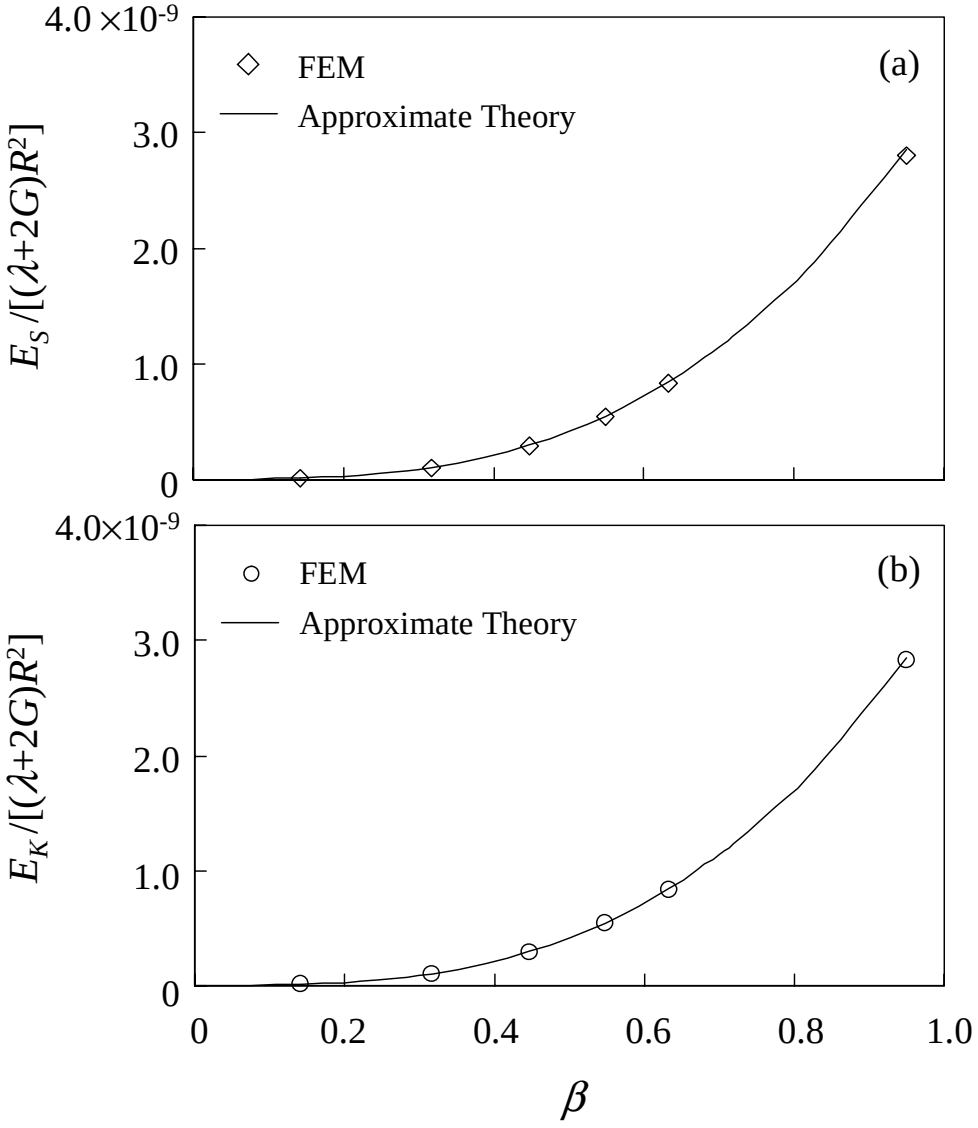

Fig. 2.15 Comparison of finite element method (FEM) results and approximate theory solutions of (a) dimensionless strain energy E_S and (b) dimensionless kinetic energy E_K of an elastic half-space impacted by a rigid cylinder versus β for dimensionless indentation velocity $\tilde{V}_i = 1 \times 10^{-2}$.

provided the dilatational wave front resides within the surface layer during the time of dynamic analysis. Moreover, the present analysis is suitable for dynamic contacts characterized by weak adhesion, such as those involving dissimilar materials and

lubricated interfaces, or macroscopic contacts for which the contribution of surface forces is negligible.

2.6 Conclusions

Impact of a rigid sphere or cylinder on elastic homogeneous half-space was examined in the context of results from a dimensional analysis and finite element simulations. A dimensionless parameter, β, was introduced in order to evaluate the effect of wave propagation on the deformation response. Finite element results for the contact radius, contact pressure, and subsurface stress, strain, and velocity fields were interpreted in terms of indentation speed, surface interference, and Poisson ratio. A general relationship for the mean contact pressure was derived for small surface interference ($\beta \leq 1$) using dimensional analysis and finite element results. An approximate theoretical model that yields accurate solutions for the contact pressure and strain and kinetic energy of the half-space was derived, and its validity was confirmed by finite element results. Based on the presented results and discussion, the following main conclusions can be drawn from this study.

(1) For small surface interference ($\beta \leq 1$), the dilatational wave front is confined within the contact region and the real contact area is equal to the truncated contact area. However, for relatively large surface interference ($\beta > 1$), the wave front extends beyond the contact edge and the real contact area is less than the truncated contact area.

(2) The mean contact pressure at the instant of initial contact increases linearly with the indentation speed. For small surface interference ($\beta \leq 1$), the contact pressure distribution is uniform and the mean contact pressure is constant. For large

surface interference ($\beta > 1$), the contact pressure distribution is elliptic and the mean contact pressure increases gradually with the surface interference. For axisymmetric analysis, when $\beta \to \infty$ (i.e., very large surface interference and/or very low indentation speed), the contact pressure distribution approaches the Hertz solution.

(3) In the small surface interference regime, the stresses, strains, and displacements in the subsurface decrease abruptly in the vicinity of the dilatational wane front. However, the material in the wake of the wave front is subjected to nearly uniform stress, strain, and velocity fields.

(4) An approximate energy-based analysis was developed for small surface interferences. Results for the strain and kinetic energy of the half-space and the mean contact pressure obtained from this analysis were found to be in good agreement with finite element results, confirming the validity of the assumptions in the approximate analysis.

(5) For $\beta \leq 1$, the results for the contact pressure and subsurface stress, strain, and velocity fields obtained from the axisymmetric (spherical indenter) and plane-strain (cylindrical indenter) analyses exhibited close similarities. The fact that these results are independent of the indenter radius in both analyses suggests that these results are generally applicable for impact between any isotropic elastic bodies with smooth surfaces.

CHAPTER 3

Dynamic Contact Between an Elastic-Plastic Multi-Layered Medium and a Rigid Cylinder

3.1 Introduction

Hard and tough surface layers are traditionally used in engineering components to improve the contact fatigue resistance and tribological properties of interacting surfaces and to protect the substrate from the accumulation of inelastic deformation and cracking. Fundamental knowledge of the stress and strain fields in layered media subjected to surface traction is critical to the endurance of electromechanical devices undergoing repetitive contact, such as relays, switches, vibromotors, and micromirror displays. Early studies dealing with normal contact of layered media provided analytical treatments for the elastic response due to indentation loading. Burmister (1945) obtained solutions for the stresses and displacements in an elastic single-layered medium subjected to axisymmetric surface loading. Dhaliwal and Rau (1970) analyzed the axisymmetric Boussinesq problem of an elastic layer on an elastic foundation. Gupta and Walowit (1974) developed a plane-strain elastic theory for a layered medium under both normal and tangential surface loadings, and King and O'Sullivan (1987) extended the previous theory to obtain analytical solutions for an elastic layered medium subjected to sliding contact loading. Brock and Georgiadis (1994) presented a dynamic analysis of a linear-elastic half-plane indented by either a wedge or a parabolic rigid indenter.

Despite valuable insight into the mechanics of indented media derived from previous analytical studies, it is difficult to apply the approaches of these works to the

analysis of elastic-plastic contact of layered media. Consequently, numerical techniques based mainly on the finite element method were advanced in order to account for more complicated contact geometries and more realistic constitutive laws. One of the first finite element analysis of elastic-plastic indentation of a layered medium is attributed to Kennedy and Ling (1974) who investigated the effects of layer thickness, mechanical properties of the layer and substrate materials, and interfacial contact conditions on the plastic deformation of the layered medium. Komvopoulos (1989) investigated the plane-strain problem of a rigid cylinder indenting an elastic-plastic substrate coated with a harder and stiffer layer using the finite element method. Plastic deformation was found to initiate at the layer/substrate interface and the contact pressure profile was significantly flattened with increasing plastic deformation. In a finite element analysis of an elastic-plastic layered medium penetrated by an elastic indenter performed by Montmitonnet et al. (1993) the stress field in the layered medium was interpreted in terms of the layer thickness, and the highest tensile stress was reported to occur at the surface of the medium. Kral et al. (1995a, 1995b) presented a finite element contact analysis of a layered medium, exhibiting either perfectly plastic or isotropic strain hardening post-yield behavior, which was repeatedly indented by a rigid sphere and interpreted the propensity for crack initiation during the first indentation cycle in the context of the obtained finite element results.

More recently, Gan and Ben-Nissan (1997) examined the influence of the mechanical properties of a ductile substrate coated with a hard layer on the indentation load and reported a significant effect of the yield strength and strain hardening properties and a minor effect of the elastic modulus on the applied normal load. Faulkner et al.

(1998) compared finite element results for an elastic-plastic layered medium in contact with either a rigid or a deformable indenter and observed higher contact pressures in the elastic regime and lower peak radial tensile stress in the case of the rigid indenter. Sen et al. (1998) used the finite element technique to model indentation of an elastic, work hardening layered medium by an elastic sphere and obtained elastic and elastic-plastic solutions for the contact pressure distribution. Souza et al. (1999) reported a greater likelihood for film cracking in systems with elastic-plastic substrates coated with thin layers of higher elastic modulus. Stephens et al. (2000) obtained finite element results for the initial yield behavior of a hard coating/soft substrate system subjected to elliptical normal and friction forces that revealed a significant increase in the durability of the layered system when the interface possessed graded mechanical properties.

The review of the literature indicates that the majority of the analytical and numerical solutions of various indentation problems involving elastic and elastic-plastic layered media have been restricted to quasi-static contact conditions. Although important insight into the mechanics of layered media has been derived from these studies, the obtained solutions might not be applicable to dynamic contact problems, e.g., nano-/microindentation testing where high adhesion forces (Landman et al., 1990) cause the indenting tip to “jump” into contact with the sample surface. Streator (2003) performed a numerical analysis of dynamic contact between a rigid sphere and an elastic half-space and reported that the produced maximum compressive force was appreciably higher than that obtained under quasi-static contact conditions, even for indentation speeds two orders of magnitude less than the dilatational wave speed. Consequently, the objective of this chapter was to develop a comprehensive finite element analysis of dynamic

indentation of elastic-plastic multi-layered media. According to the discussion in chapter 2, for small interferences (i.e., during the short time period that the dilatational wave front resides within the surface layer), a layered medium dynamically indented by a rigid cylinder (or sphere) yields a behavior similar to that of a homogeneous medium with material properties those of the surface layer of the layered medium. Therefore, the focus of this chapter is on relatively large interferences such that the dilatational wave front spreads over layers. In view of the effect of the waves reflected from the mesh boundaries, the mesh selection for unbiased contact analysis is described first, followed by finite element results demonstrating the effects of indentation speed and radius of the rigid cylindrical indenter on the normal force, contact pressure distribution, and subsurface stress-strain field in a multi-layered medium subjected to dynamic indentation loading.

3.2 Finite Element Mesh for Dynamic Contact Analysis

As discussed in chapter 2, two types of bulk waves can propagate in infinite solids: longitudinal waves (also known as dilatational waves because they are characterized by a volume change) and transverse (or shear) waves (Pollard, 1977). In seismology, these two types of waves are often referred to as P (primary) and S (secondary) waves, respectively. In isotropic elastic solids, the propagation speed of a plane dilatational wave, c_p, and a plane shear wave, c_s, are given by

$$c_P = \left[(\lambda + 2G)/\rho\right]^{1/2} \quad \text{and} \quad c_S = (G/\rho)^{1/2},$$

where ρ is the material density, and λ and G are the Lamé constants, expressed in terms of the elastic modulus, E, and Poisson's ratio, ν, as

$\lambda = E\nu/[(1+\nu)(1-2\nu)]$ and $G = E/[2(1+\nu)]$.

It is obvious from the above relations that a plane dilatational wave propagates much faster than a plane shear wave. In addition to these two types of bulk waves, surface waves, such as Rayleigh and Love waves, may be encountered in the case of bounded solids. In general, the propagation speeds of these surface waves are comparable to those of shear waves (Beltzer, 1988). Therefore, the attention in this analysis is restricted to the faster propagating dilatational waves.

3.2.1 Finite Element Mesh for Homogeneous Medium.

In static analysis of infinite half-space media subjected to surface (contact) loads, a reference point is needed in order to obtain the displacements due to the singularity of the displacement field under plane strain conditions (Johnson, 1985). This reference point is usually selected to be far away from the contact region. Hence, in plane-strain static contact analyses the solution depends on the location of the reference point. However, in dynamic contact analyses, if the displacements in a given region occur within a certain time t_o, then at a fixed point remote from this region a disturbance does not occur before the arrival of the propagating waves, i.e., the displacement at any material point ahead of the wave front is zero (Johnson, 1985). Therefore, in dynamic plane-strain contact analysis, if the reference point is selected to be sufficiently remote from the contact region, such that the waves do not reach this point during the analysis, the numerical results will be independent of the location of the reference point. Figure 3.1 shows schematically a propagating dilatational wave in a semi-infinite homogeneous solid.

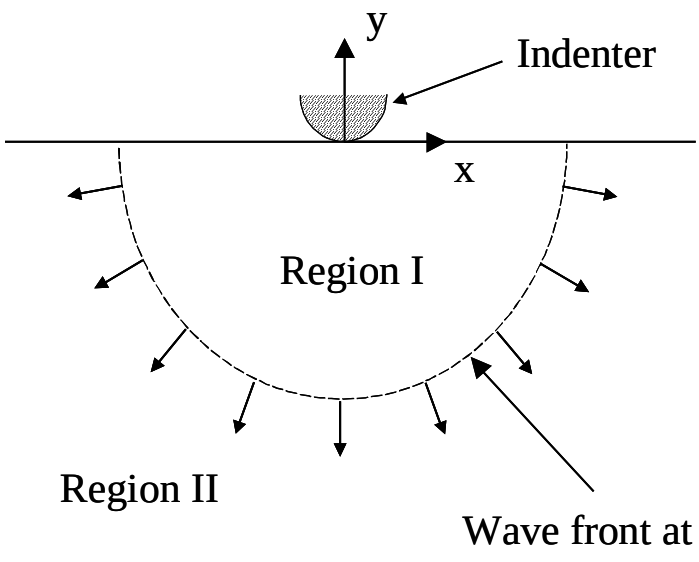

Fig. 3.1 Schematic representation of wave propagation in a semi-infinite half-space.

Contact is first established at the origin ($x = y = 0$) at time t_o. The discontinuous curve represents the dilatational wave front at time t_1. There is no disturbance in the region ahead of the wave front (region II). Thus, choosing any point in region II as the reference point yields identical results throughout region I if the analysis is performed during period [t_o, t_1]. In finite element analyses, a finite mesh is used to simulate the semi-infinite half-space. If waves are not generated from the artificial boundaries (i.e., fixed and/or free boundaries), any mesh larger than region I would produce identical results at each point of the mesh within a given time period. Furthermore, the simulation results would be independent of the forces and/or displacements applied to the artificial boundaries where the waves do not have enough time to propagate. In most applications, the region of interest is close to the contact interface, where the highest stresses and strains occur. In this subsurface region, unbiased simulation results can be obtained by

using a sufficiently large mesh such that the wave(s) reflected from the artificial boundaries do not reach this region before the analysis has been completed.

In view of the previous considerations, finite element simulations of dynamic contact were performed with the code ABAQUS using the four meshes shown in Fig. 3.2. For increased accuracy and better convergence, the ABAQUS/Standard package (implicit integration) rather than the generally faster ABAQUS/Explicit package (explicit integration) was used in this analysis. An elastic homogeneous half-space indented by a rigid cylinder at a constant speed of $1 \times 10^{-3}\, c_p$ was modeled in all simulations. The plane strain condition assumed in this analysis is suitable for surfaces possessing predominant texture in the direction perpendicular to the *xy* plane. The obtained results and trends should exhibit similarities with those of axisymmetric contacts. Special contact elements were used to model contact between the rigid indenter and the elastic medium. The dimensions of the four meshes, normalized by the radius of the rigid cylinder, *R*, were chosen to be equal to 6.4×6.4, 12.8×6.4, 6.4×12.8, and 12.8×12.8. Because the left boundary of each mesh is a symmetry axis, the nodes of this boundary ($x = 0$) were constrained against displacement in the *x*-direction. The nodes of the bottom boundary were constrained against displacement in the *y*-direction, while the nodes of the right boundary and the surface were allowed to move freely. The characteristic length of a mesh, l_c, is defined as the smallest mesh dimension. Thus, the characteristic length of the meshes shown in Figs. 3.2(a), 3.2(b), and 3.2(c) is equal to $6.4R$ and that of the mesh shown in Fig. 3.2(d) is equal to $12.8R$. In the following discussions, $l_c^{(i)}$ is used to denote the characteristic length of the i^{th} mesh. Obviously, $l_c^{(1)} = l_c^{(2)} = l_c^{(3)} < l_c^{(4)}$. Since far-field propagation of a cylindrical dilatational wave occurs at a speed comparable to that

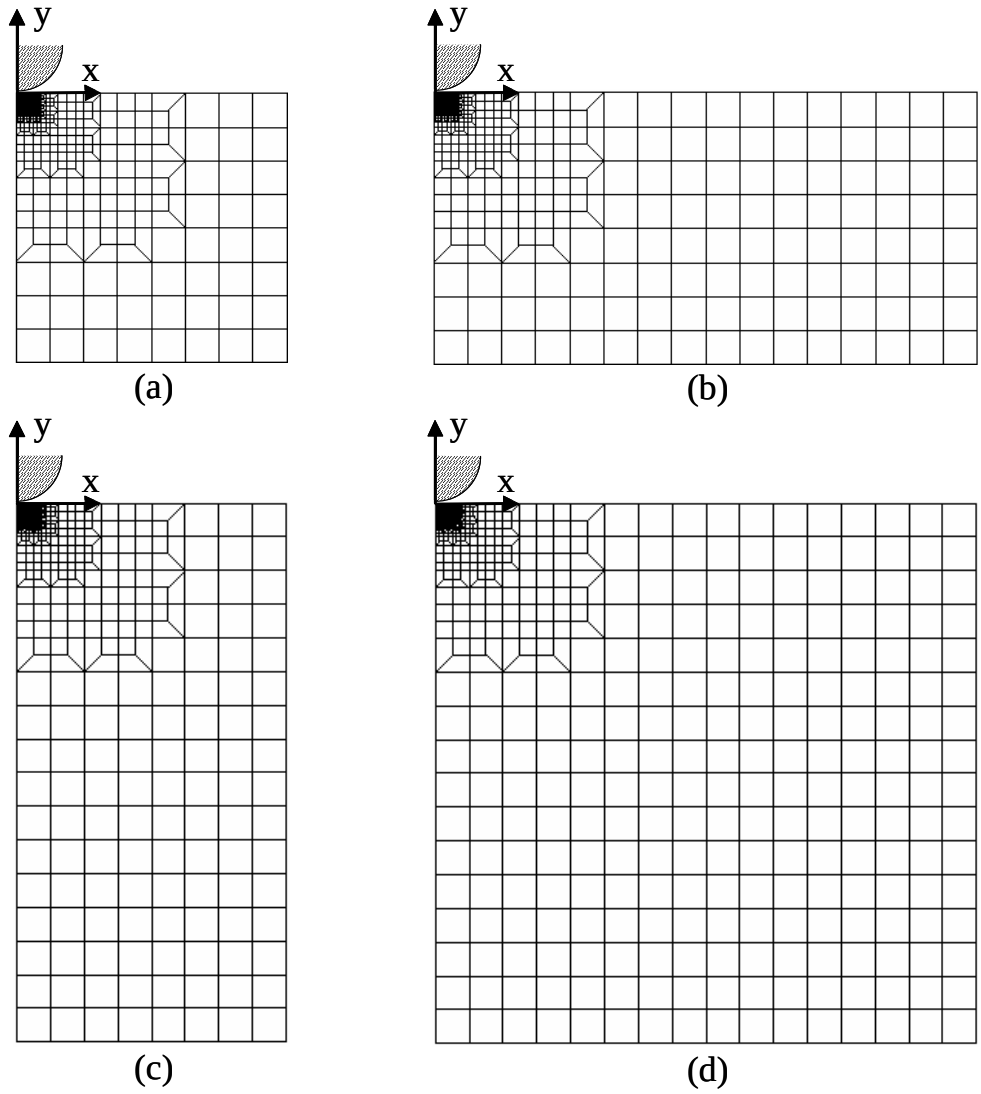

Fig. 3.2 Finite element models used to study the effect of the mesh size on the dynamic response of an elastic homogeneous half-space indented by a rigid cylinder. The mesh dimensions normalized by the indenter radius are (a) 6.4×6.4, (b) 12.8×6.4, (c) 6.4×12.8, and (d) 12.8×12.8.

of a plane dilatational wave, the critical time for a dilatational wave propagating from the origin ($x = y = 0$) to the nearest boundary of the meshes shown in Figs. 3.2(a)-3.2(c) can be estimated from relation $t_{cr}^{(1)} \approx l_c^{(1)}/c_p$. Then, the critical time for a wave reflected from the nearest boundary to reach a point in a region close to the origin is approximately equal to $2t_{cr}^{(1)}$.

Figure 3.3 shows the dimensionless contact load, P/ER, and maximum von Mises stress, $\sigma_M^{\max}/E$, in an elastic half-space as functions of dimensionless time, $t/t_{cr}^{(1)}$, from the onset of indentation, where E is the elastic modulus of the half-space. Since P and $\sigma_M^{\max}$ are mainly related to the stress field of the subsurface region close to the origin, the results would be independent of mesh size provided $t \leq 2t_{cr}^{(1)}$. This is confirmed by the results shown in Fig. 3.3. Indeed, for $t > 2t_{cr}^{(1)}$, the solutions begin to deviate. For the mesh shown in Fig. 3.2(c), the dilatational wave reflected from the free boundary at x/R = 6.4 propagated back first, while for the mesh shown in Fig. 3.2(b) the dilatational wave reflected from the fixed boundary y/R = -6.4 propagated back first. For the mesh shown in Fig. 3.2(a), the two dilatational waves reflected from the bottom and right boundaries propagated back to the origin at about the same time. The relatively small discrepancies in the results for the contact force and Mises stress obtained with the meshes shown in Figs. 3.2(a) and 3.2(b) and, similarly, those obtained with the meshes shown in Figs. 3.2(c) and 3.2(d) indicate that the wave reflected from the bottom boundary exhibits a dominant effect. Both Figs. 3.3(a) and 3.3(b) show that discrepancies in the results (compared to those obtained with the mesh shown in Fig. 3.2(d)) occur due to the reflected waves at about the same time for the meshes shown in Figs. 3.2(a) and 3.2(b) and a little later for the mesh shown in Fig. 3.2(c). This implies that the critical time of a mesh (i.e., t_{cr} or ~$2t_{cr}$ if the entire mesh or only a small region of the mesh close to the origin is of interest, respectively) yields a conservative estimate for the maximum time for dynamic contact analysis not affected by the reflected wave(s).

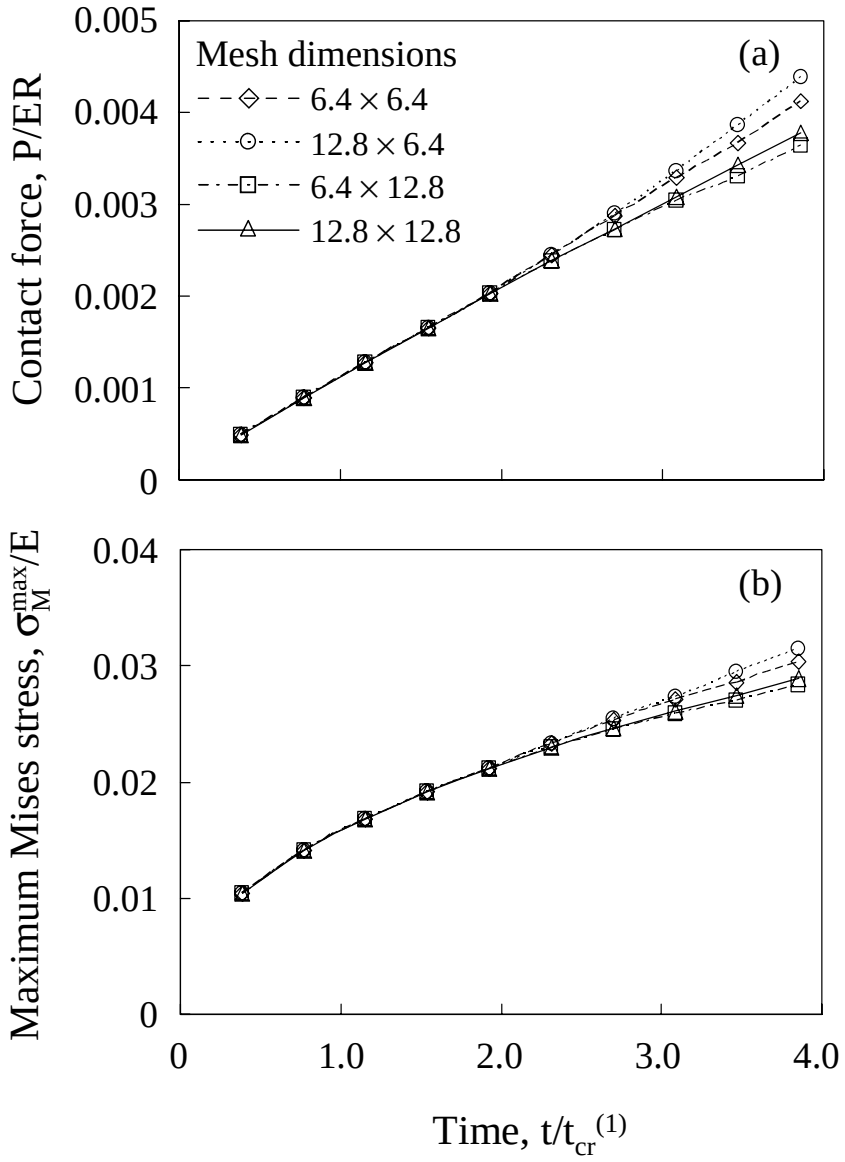

Fig. 3.3 (a) Contact force and (b) maximum von Mises equivalent stress versus time from the initiation of normal contact for an elastic homogenous half-space indented by a rigid cylinder moving at speed $V = 1 \times 10^{-3} c_p$.

3.2.2 Finite Element Mesh for Multi-Layered Medium.

Similar simulations were performed for an elastic-plastic multi-layered medium using the meshes shown in Fig. 3.4. The thickness (normalized by the indenter radius)

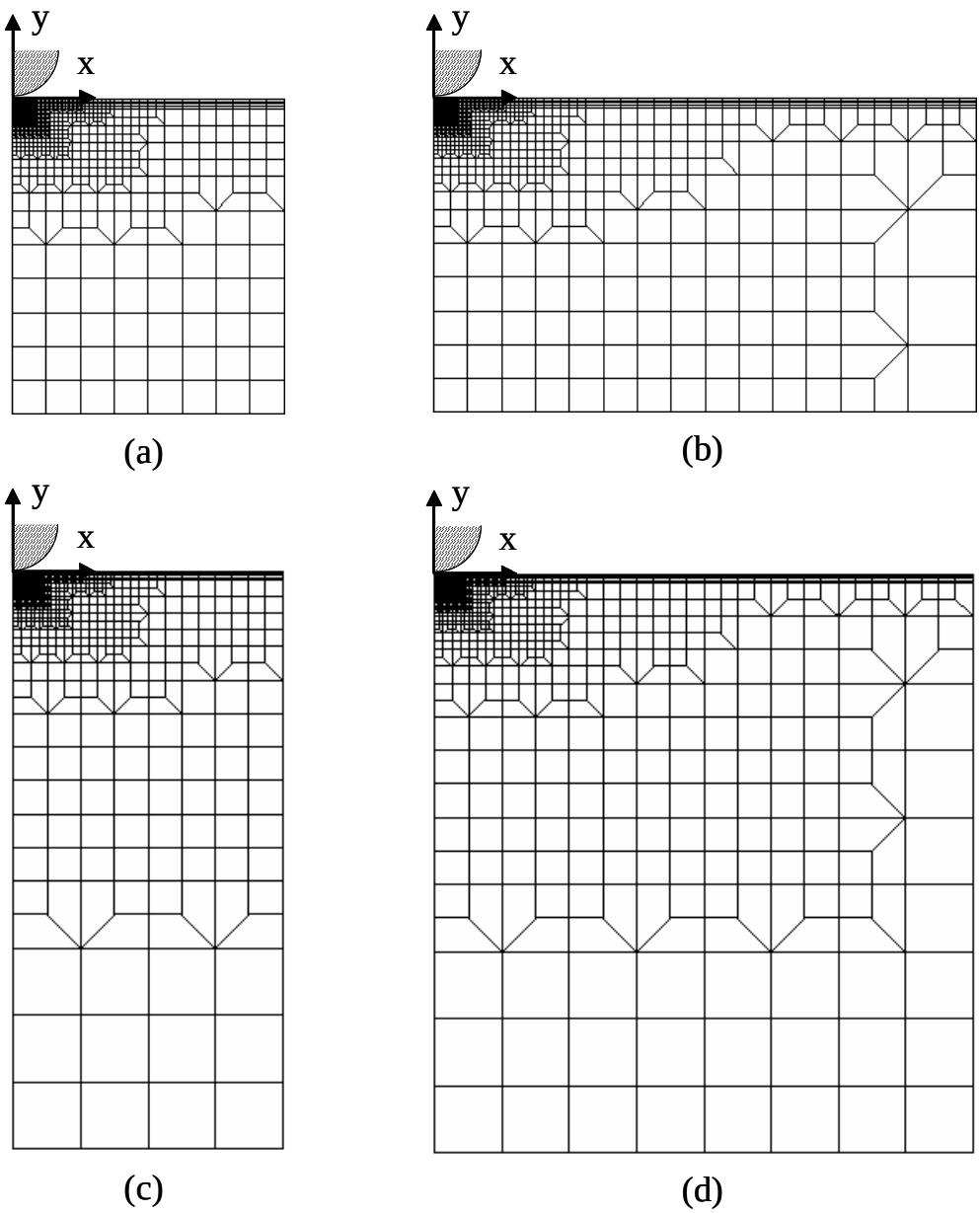

Fig. 3.4 Finite element models used to study the effect of the mesh size on the dynamic response of an elastic-plastic multi-layered medium indented by a rigid cylinder. The mesh dimensions normalized by the indenter radius are (a) 6.4×7.46, (b) 12.8×7.46, (c) 6.4×13.86, and (d) 12.8×13.86.

and material properties of the multi-layered medium given in Table 3.1 (Kaye, 1986; Komvopoulos, 2000) are representative of thin-film rigid disks used in magnetic

Table 3.1. Thickness and material properties of the elastic-plastic multi-layered medium subjected to dynamic indentation of a rigid cylinder

Medium	Normalized thickness (t/R)	Elastic modulus (GPa)	Yield strength (GPa)	Density (kg/m^3)
Layer 1	0.05	168	13.0	2266
Layer 2	0.156	130	2.67	8800
Layer 3	0.8	140	2.58	7000
Layer 4	6.4, 12.8, 51.2	160	2.67	8000

Sources: Kaye (1986) and Komvopoulos (2000).

recording. The material properties and size of the bottom (fourth) layer are identical to those of the homogeneous half-space discussed in the previous section. The normalized (by the indenter radius) dimensions of the meshes shown in Figs. 3.4(a)-3.4(d) are 6.4×7.46, 12.8×7.46, 6.4×13.86, and 12.8×13.86, respectively. Since for the load range analyzed in this analysis the plastic zone is predicted to be very small compared to the mesh dimensions, the elastic properties of the layered medium control the wave velocity. Figure 3.5(a) shows that the variation of $\sigma_M^{\max}$ in the surface layer with time and the critical time that the results begin to deviate from those corresponding to the mesh shown in Fig. 3.4(d) are similar to those obtained for the elastic homogeneous half-space (Fig. 3.3(b)). This suggests that wave propagation in the thick (fourth) layer plays a predominant role in the stress-strain calculations. Figure 3.5(b) reveals that the results for the maximum equivalent plastic strain, $\varepsilon_{eq}^{\max}$, in the second (soft) layer begin to deviate at approximately the same critical time as that of $\sigma_M^{\max}$. This is due to the fact that the

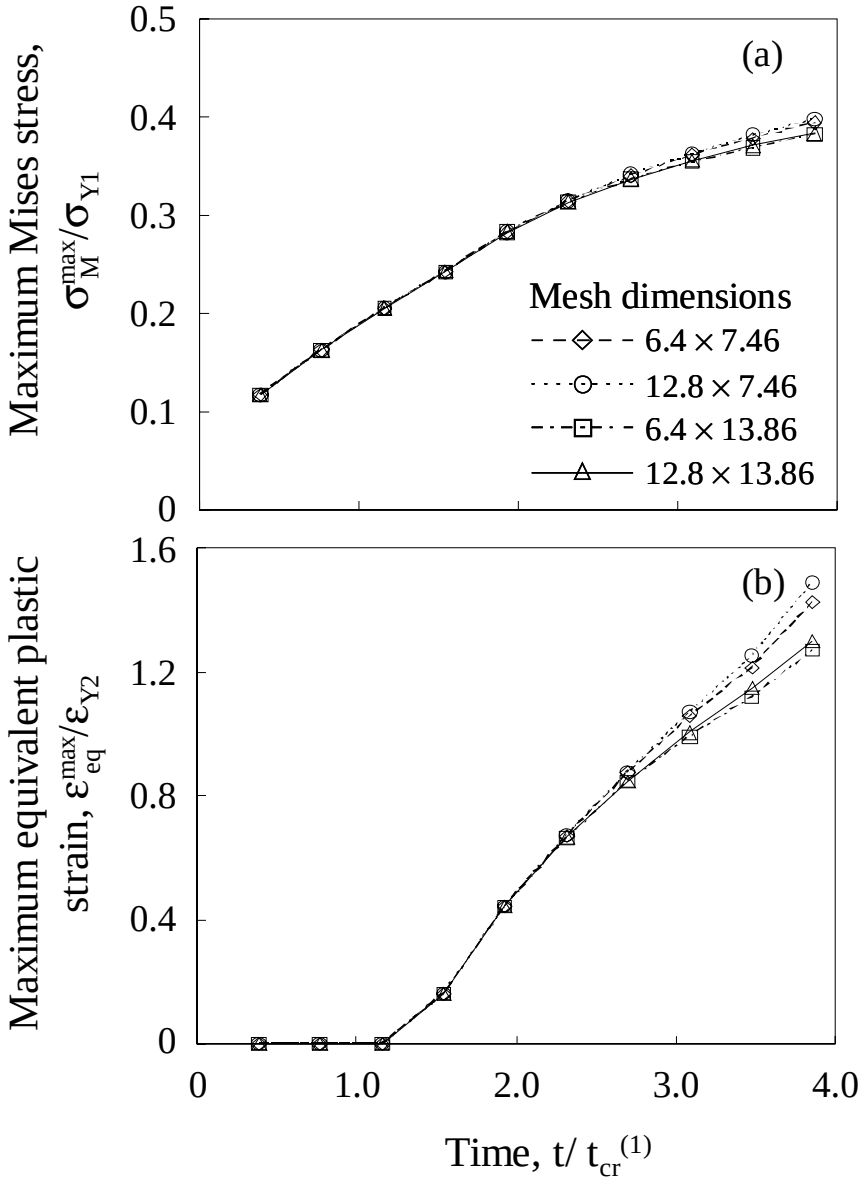

Fig. 3.5 (a) Maximum von Mises equivalent stress in the surface (hard) layer and (b) maximum equivalent plastic strain in the second (soft) layer versus time from the initiation of contact for an elastic-plastic multi-layered medium indented by a rigid cylinder moving at speed $V = 1 \times 10^{-3} c_P^{(4)}$, where $c_P^{(4)}$ is the propagation speed of the plane dilatational waves in the thick substrate (fourth layer).

locations of $\sigma_M^{\max}$ and $\varepsilon_{eq}^{\max}$ are close to each other and both occur in a subsurface domain adjacent to the contact region.

3.3 Dynamic Indentation of an Elastic-Plastic Multi-Layered Medium

3.3.1 Finite Element Modeling and Material Properties of Multi-Layered Medium.

Dynamic indentation of a multi-layered medium by a rigid cylinder was analyzed with the finite element code ABAQUS/Standard. Contact between the rigid indenter and the multi-layered medium was modeled with rigid surface and second-order contact elements, which were assigned a common reference node that defined the motion of the rigid surface. The rotational and horizontal displacements of the reference node were fully constrained. Indentation was modeled by advancing the rigid surface profile against the deformable mesh using a displacement-control incremental scheme. In view of the marginal effect of friction in normal contact (Komvopoulos, 1988), only frictionless indentations were considered in this chapter. Because of the displacement-control simulation scheme and the assumption of rigid indenter, the effect of the indenter mass on the simulation results was neglected. The multi-layered medium was modeled by eight-node, bi-quadratic, plane-strain elements. A 3×3 Gaussian integration was used in each element. Because of symmetry and the assumed boundary conditions, only one-half of the multi-layered medium (Fig. 3.6) was modeled, and the nodes on the symmetry axis ($x = 0$) were constrained against displacement in the x-direction. The nodes of the bottom boundary were constrained against displacement in the y-direction. The mesh near the surface was refined as shown in Fig. 3.6. The radius of the cylindrical indenter was selected to be equal to $0.2R$, $1.0R$, and $2.0R$, i.e., normalized indenter radius $\tilde{R} = 0.2$, 1.0, and 2.0. Hereafter, all the length parameters are normalized by the intermediate indenter radius, R, and are presented in dimensionless form. For greater numerical accuracy, the

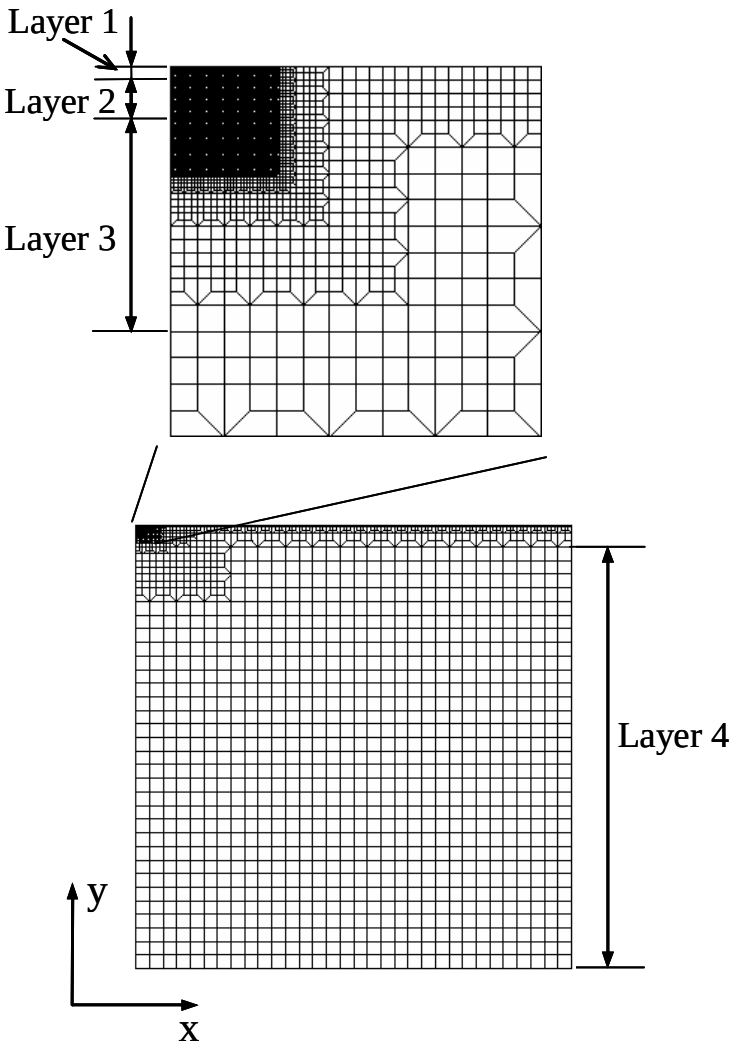

Fig. 3.6 Finite element mesh for dynamic contact analysis of an elastic-plastic multi-layered medium indented by a rigid cylinder.

smallest elements adjacent to the surface are squares of sides equal to 0.00625*R*, i.e., one-eighth of the thickness of the thinnest layer. This refinement of the mesh is for numerical purposes and does not imply the use of a continuum description for domains approaching the lattice dimensions. Therefore, caution should be exercised in selecting the thickness

of the surface layer. The mesh size ($51.2R \times 52.26R$) was selected such that during the analysis the reflected waves did not propagate back to the region of interest. The normalized thickness and material properties of the multi-layered medium are given in Table 3.1. These material properties are typical of magnetic rigid disks (Komvopoulos, 2000). For simplicity, all layers were assumed to have a Poisson's ratio equal to 0.3. For the selected properties, the speed of the plane dilatational waves in the fourth layer is about 5189 m/s. Each layer was modeled as an elastic-perfectly plastic material. The classical von Mises yield criterion was used throughout the dynamic contact simulations.

3.3.2 Simulation of Dynamic Indentation.

Dynamic indentation was modeled by applying incremental displacements to the rigid surface in a controlled fashion, which were identical for both loading and unloading. The speed of the indenter was constant throughout the loading and unloading simulation steps. Simulations were performed for indentation speed equal to $1 \times 10^{-3}\ c_P^{(4)}$, $2 \times 10^{-3}\ c_P^{(4)}$, and $4 \times 10^{-3}\ c_P^{(4)}$, where $c_P^{(4)}$ is the propagation speed of the plane dilatational waves in the thick substrate (fourth layer). Results are presented in terms of dimensionless indentation speed, $\tilde{V}$, obtained by dividing the indenter speed by $c_P^{(4)}$. The maximum indentation depth was selected to be equal to $0.02R$. While the damping effect was ignored in the simulations of indentation loading and unloading, to obtain solutions for the residual stress-strain field, dashpot elements were added to the mesh after full unloading. The damping coefficients of the dashpot elements were arbitrarily selected to achieve fast equilibrium.

3.4 Results and Discussion

Finite element solutions for the contact pressure distribution and subsurface stress and strain fields in the multi-layered medium are presented for different values of normalized indentation depth, $\tilde{\delta}$, indentation speed, $\tilde{V}$, and indenter radius of curvature, $\tilde{R}$. The propensity for plastic flow and cracking is interpreted in the context of results for the maximum von Mises stress, equivalent plastic strain, and maximum tensile stress in the multi-layered medium during loading and unloading.

3.4.1 Contact Force and Contact Pressure Distribution

Figure 3.7 shows the variation of the contact force, P, with indentation depth, δ, for different values of normalized indentation speed and indenter radius. The contact force is normalized by the critical load, P_Y, corresponding to the inception of yielding in the multi-layered medium due to indentation by a rigid cylinder of intermediate radius ($\tilde{R}$ = 1.0) penetrating at a relatively high velocity ($\tilde{V}$ = 4×10^{-3}). Figure 3.7(a) shows that the contact force increases monotonically with indentation depth and speed. In dynamic normal contact, a fraction of the external work is dissipated in the form of kinetic energy in the multi-layered medium. Consequently, the energy dissipated in the deforming medium increases with indentation speed. In addition, larger gradients in the displacement field occur at higher indentation speeds adjacent to the contact region. Therefore, the strains and strain energy intensify with the increase of the indentation speed. Consequently, a higher indentation speed produces a higher contact force for the

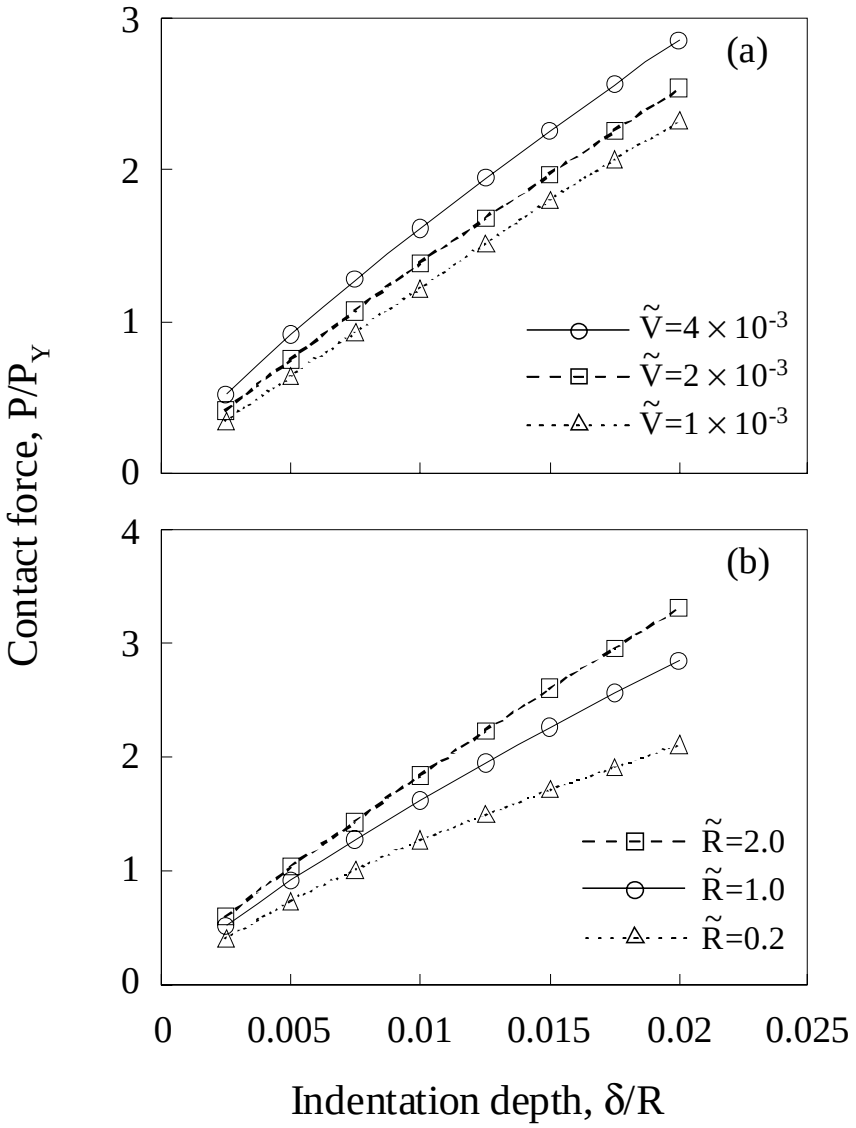

Fig. 3.7 Contact force on elastic-plastic multi-layered medium indented by a rigid cylinder versus indentation depth for (a) varying indentation speed and constant indenter radius ($\tilde{R}$ = 1.0) and (b) varying indenter radius and constant indentation speed ($\tilde{V}$ = 4×10^{-3}).

same surface penetration distance. Figure 3.7(b) demonstrates that, for a given indentation depth, a lower contact force is obtained with the sharper indenter, evidently

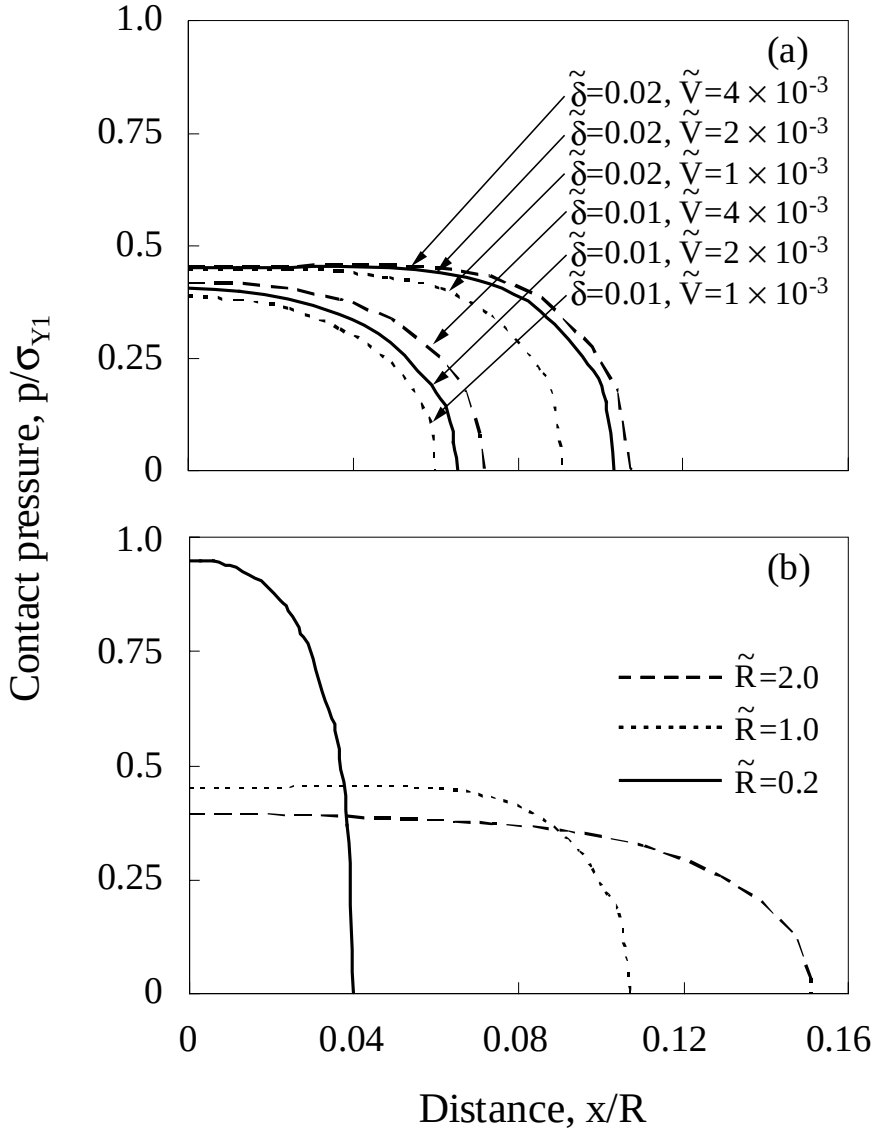

Fig. 3.8 Contact pressure distribution on elastic-plastic multi-layered medium indented by a rigid cylinder for (a) varying indentation depth and speed and constant indenter radius ($\tilde{R}$ = 1.0) and (b) varying indenter radius and constant indentation depth ($\tilde{\delta}$ = 0.02) and speed ($\tilde{V}$ = 4×10^{-3}).

due to the correspondingly smaller contact area.

Figure 3.8 illustrates the dependence of the contact pressure, *p,* on dimensionless indentation depth, speed, and radius of the rigid indenter. The contact pressure is

normalized by the yield strength of the surface layer, σ_{Y1}, and the distance x from the center of contact ($x = 0$) by the intermediate indenter radius, R. The effect of the various dimensionless parameters on the contact pressure distribution can be explained in terms of the dependence of subsurface plastic deformation on these parameters (discussed in detail in the following section). As shown in Fig. 3.8(a), increasing the indentation speed intensifies the contact pressure and increases the contact area, in accord with the contact force results shown in Fig. 3.7(a). The increase of the maximum contact pressure is a result of the larger strains occurring in a subsurface region adjacent to the contact interface, while the increase of the contact (width) area with indentation speed is a consequence of the slower downward movement of the surface of the deforming multi-layered medium compared to that of the penetrating indenter. Figure 3.8(b) shows the effect of the indenter radius on the contact pressure distribution for both constant indentation depth ($\tilde{\delta} = 0.02$) and speed ($\tilde{V} = 4 \times 10^{-3}$). As expected, a higher peak pressure and a smaller contact width were obtained with the sharper indenter. In the case of the indenter with intermediate radius ($\tilde{R} = 1.0$), the peak pressure shifts toward the contact edge due to the excessive plastic deformation in the soft second layer, conversely to the relatively blunt ($\tilde{R} = 2.0$) and sharp ($\tilde{R} = 0.2$) indenters producing a peak pressure at the center of the contact region. This trend is also associated with the effect of the indenter radius on the subsurface stress-strain field. It will be shown later that, due to the much higher yield strength of the surface layer (Table 3.1), plastic deformation is encountered only in the second (soft) layer. For the larger indenter radius, the small value of δ/R produces less plastic deformation. Regarding the smaller indenter radius (sharp indenter), the high ratio of the thickness of the surface layer to the contact width ($t_1/a > 1$)

promotes the dominance of elastic deformation in the multi-layered medium and, thus, the peak pressure arises at the center of the contact region.

3.4.2 Subsurface Stresses and Evolution of Plasticity

Contours of normalized von Mises equivalent stress, σ_M/σ_{Y1}, in the multi-layered medium obtained from high-indentation speed ($\tilde{V} = 4 \times 10^{-3}$) simulations with an indenter of intermediate radius ($\tilde{R} = 1.0$) are shown in Fig. 3.9. In this figure, as well in subsequent stress (strain) contour figures, stress (strain) contours are shown within the first two layers, where the higher stresses (strains) occurred in all the simulation cases. Stress discontinuities arise at the interface due to the material property mismatch between the first and second layer. For the simulated range of indentation depth ($\tilde{\delta} \leq 0.02$), the hard surface layer exhibited purely elastic deformation. For relatively small indentation depth ($\tilde{\delta} = 0.0025$), $\sigma_M^{\max}$ occurs in the surface layer at a depth approximately equal to half of the contact width (Fig. 3.9(a)). However, increasing the indentation depth causes $\sigma_M^{\max}$ to shift toward the interface (Fig. 3.9(b)). After yielding in the soft layer ($\tilde{\delta} > 0.005$), $\sigma_M^{\max}$ arises always at the bottom of the hard surface layer near the interface with the plastically deformed soft layer (Figs. 3.9(b)-3.9(d)).

Figure 3.10 illustrates the effects of indentation speed and indenter radius on the evolution of $\sigma_M^{\max}/\sigma_{Y1}$ in the surface layer during the advancement of the rigid indenter into the multi-layered medium. As expected, the Mises stress intensifies with increasing indentation depth, indicating a higher likelihood for yielding in the multi-layered medium, specifically in the soft layer possessing a relatively low yield strength. The trend for $\sigma_M^{\max}$ to increase with indentation speed (Fig. 3.10(a)) is similar to that observed for

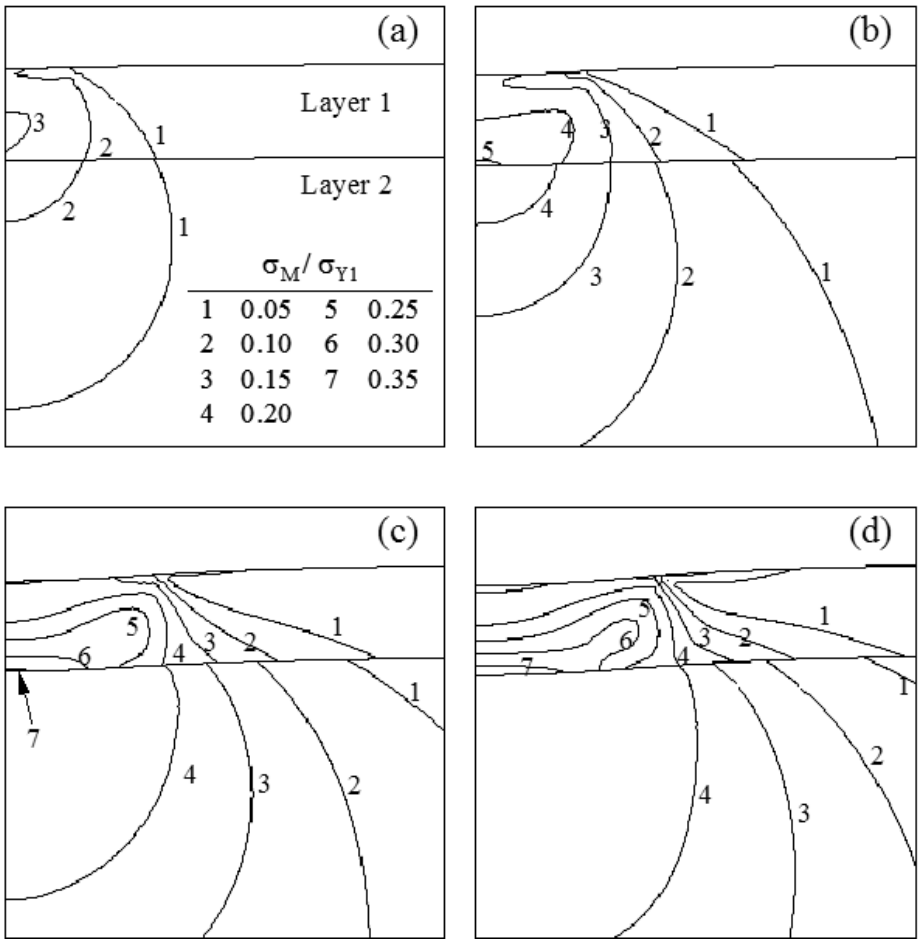

Fig. 3.9 Contours of von Mises equivalent stress in elastic-plastic multi-layered medium indented by a rigid cylinder of intermediate radius ($\tilde{R}$ = 1.0) at constant indentation speed ($\tilde{V}$ = 4×10^{-3}) for indentation depth (a) $\tilde{\delta}$ = 0.0025, (b) $\tilde{\delta}$ = 0.0075, (c) $\tilde{\delta}$ = 0.015, and (d) $\tilde{\delta}$ = 0.02.

the contact force (Fig. 3.7(a)). The higher values of $\sigma_M^{\max}$ produced with the relatively sharp indenter (Fig. 3.10(b)) are associated with the high values of δ/R and the more pronounced bending effect on the deformation of the surface layer.

To further interpret the likelihood of subsurface cracking under both loading and unloading, contours of the normalized first principal (maximum tensile) stress, σ_1/σ_{Y1}, in

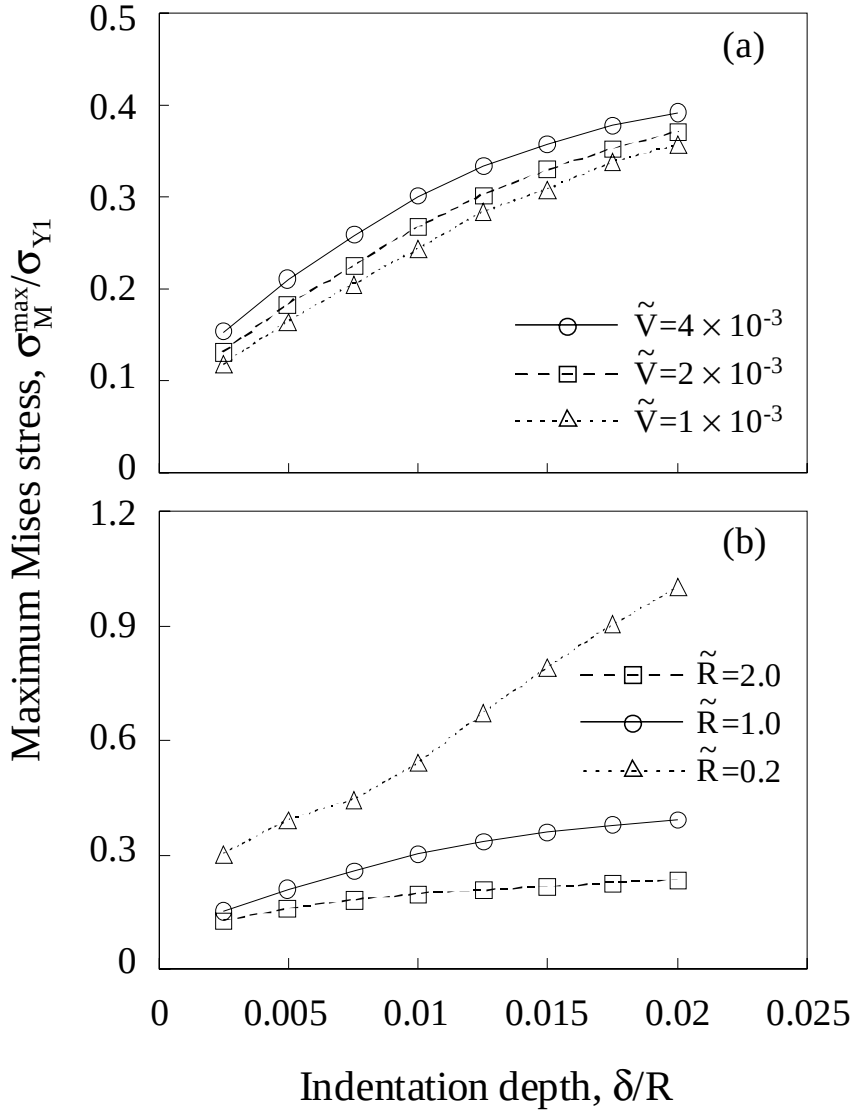

Fig. 3.10 Maximum von Mises equivalent stress in the surface (hard) layer of an elastic-plastic multi-layered medium indented by a rigid cylinder versus indentation depth for (a) varying indentation speed and constant indenter radius ($\tilde{R}$ = 1.0) and (b) varying indenter radius and constant indentation speed ($\tilde{V}$ = 4×10^{-3}).

the multi-layered medium are plotted in Fig. 3.11 for the case of relatively high indentation speed ($\tilde{V}$ = 4×10^{-3}) and intermediate indenter radius ($\tilde{R}$ = 1.0). Similar to the von Mises stress (Fig. 3.9), the maximum tensile stress occurs always in the surface

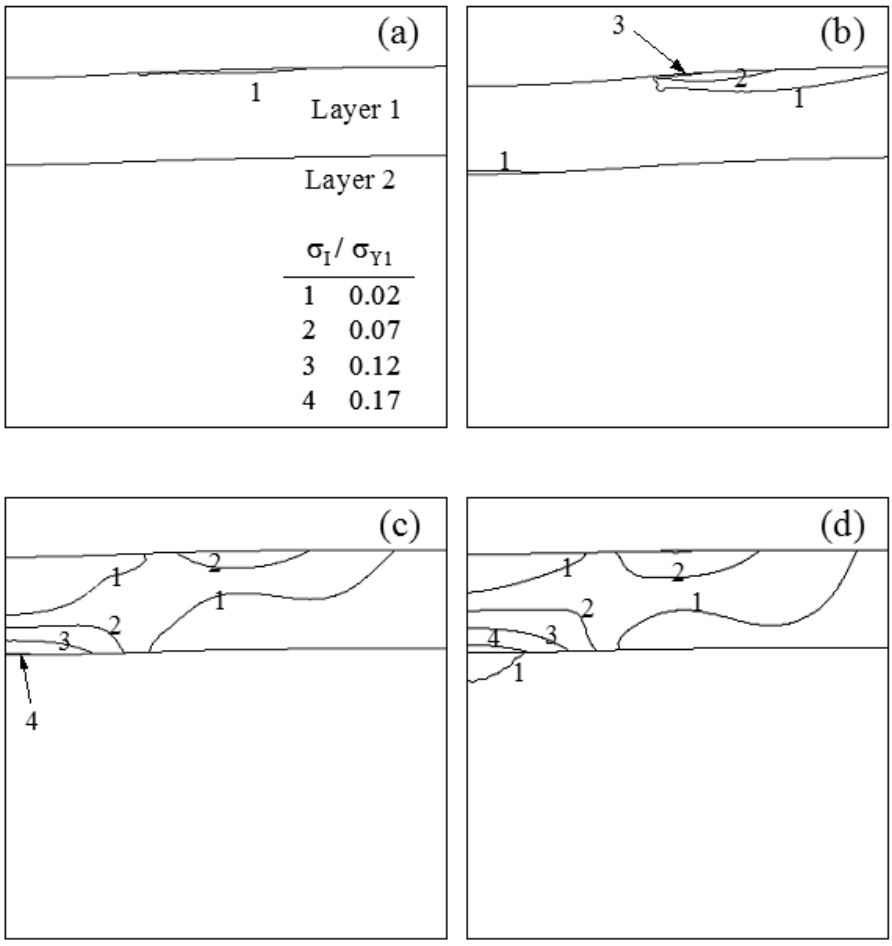

Fig. 3.11 Contours of first principal stress in elastic-plastic multi-layered medium indented by a rigid cylinder of intermediate radius ($\tilde{R}$ = 1.0) at constant indentation speed ($\tilde{V}$ = 4×10^{-3}) for indentation depth (a) $\tilde{\delta}$ = 0.01 (loading), (b) $\tilde{\delta}$ = 0.02 (loading), (c) $\tilde{\delta}$ = 0.01 (partial unloading), and (d) $\tilde{\delta}$ = 0 (full unloading).

layer. In particular, during indentation loading the maximum tensile stress arises at the surface near the contact edge (Figs. 3.11(a) and 11(b)), while during partial unloading (Fig. 3.11(c)) and full unloading (Fig. 3.11(d)) it occurs below the center of the contact region at the interface of the two layers. The results presented in Fig. 3.11 suggest a greater probability for surface and interfacial cracking during indentation loading and

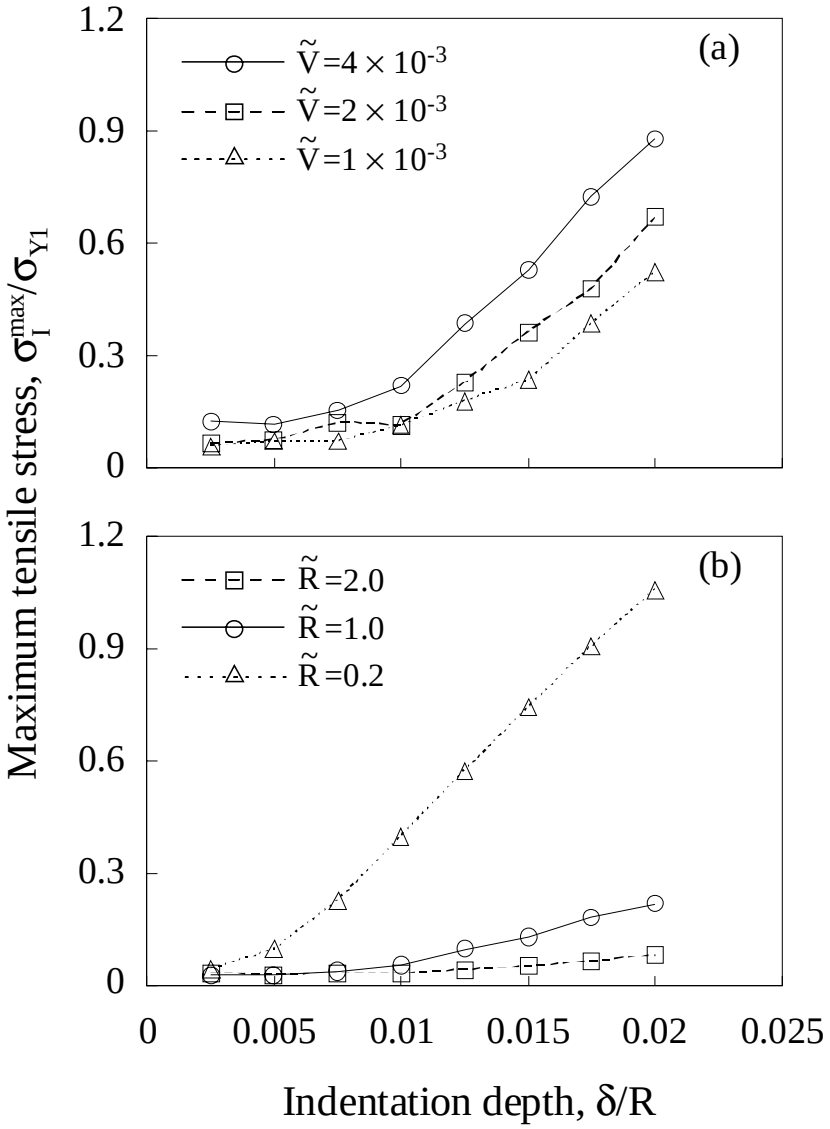

Fig. 3.12 Maximum tensile (first principal) stress in the surface (hard) layer of an elastic-plastic multi-layered medium indented by a rigid cylinder versus indentation depth for (a) varying indentation speed and constant indenter radius ($\tilde{R}$ = 1.0) and (b) varying indenter radius and constant indentation speed ($\tilde{V}$ = 4×10^{-3}).

unloading, respectively, depending on the fracture strength of the hard surface layer and the indentation speed and radius of the indenter that affect the magnitude of the maximum tensile stress. This is illustrated in Fig. 3.12 where the maximum tensile (first

principal) stress, $\sigma_I^{\max}$, in the surface layer is plotted as a function of indentation depth for different values of indentation speed and radius of the indenter. The effects of indentation speed and indenter radius on $\sigma_I^{\max}$ become significant at a critical indentation depth $\tilde{\delta} \geq 0.01$. The variation of $\sigma_I^{\max}$ reveals trends similar to those observed for $\sigma_M^{\max}$ (Fig. 3.10). As shown in Fig. 3.12(a), $\sigma_I^{\max}$ in the hard surface layer increases with indentation speed, suggesting a higher propensity for cracking in indentation experiments performed at relatively high loading rates. Cracking may also be promoted in indentation experiments involving relatively sharp indenters (Fig. 3.12(b)). Thus, caution should be exercised in nanoindentation hardness tests with thin and hard layers requiring ultra-sharp indenters to avoid the substrate deformation effect on the measurement of the layer hardness and elastic modulus.

The evolution of subsurface plasticity in the multi-layered medium may be studied in terms of the equivalent plastic strain, ε_{eq}, contours plotted in Fig. 3.13 for intermediate indenter radius ($\tilde{R}$ = 1.0), high indentation speed ($\tilde{V}$ = 4×10^{-3}), and different indentation depths. Due to the higher yield strength of the surface layer plastic deformation is confined only in the soft layer. At relatively small indentation depth ($\tilde{\delta}$ = 0.0075), a small plastic zone is produced in the soft layer at the interface with the hard surface layer below the center of contact (Fig. 3.13(a)). As the indenter advances deeper into the multi-layered medium ($\tilde{\delta}$ = 0.0125), the plastic zone grows downward into the soft layer, while $\varepsilon_{eq}^{\max}$ continues to occur along the axis of symmetry (Fig. 3.13(b)). Deeper penetration of the indenter ($\tilde{\delta}$ = 0.0175) causes further expansion of the plastic zone and a shift of $\varepsilon_{eq}^{\max}$ toward the interface with the hard surface layer (Fig. 3.13(c)). At

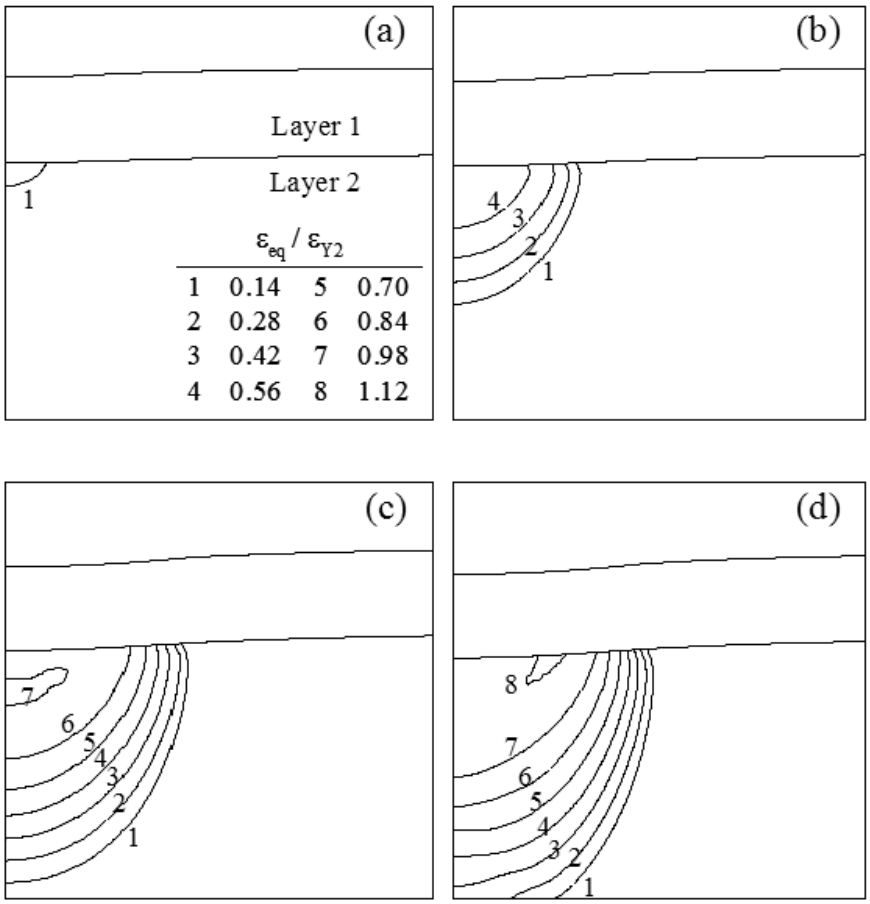

Fig. 3.13 Contours of equivalent plastic strain in elastic-plastic multi-layered medium indented by a rigid cylinder of intermediate radius ($\tilde{R}$ = 1.0) at constant indentation speed ($\tilde{V}$ = 4×10^{-3}) for indentation depth (a) $\tilde{\delta}$ = 0.0075, (b) $\tilde{\delta}$ = 0.0125, (c) $\tilde{\delta}$ = 0.0175, and (d) $\tilde{\delta}$ = 0.02.

even larger indentation depth ($\tilde{\delta}$ = 0.02), $\varepsilon_{eq}^{\max}$ commences at the interface of the two layers at a distance about one-third of the corresponding contact width (Fig. 3.13(d)). The evolution of $\varepsilon_{eq}^{\max}$ in the present dynamic contact analysis is qualitatively similar to that observed in quasi-static indentation simulations of a homogeneous half-space indented by a rigid sphere (Kral et al., 1993).

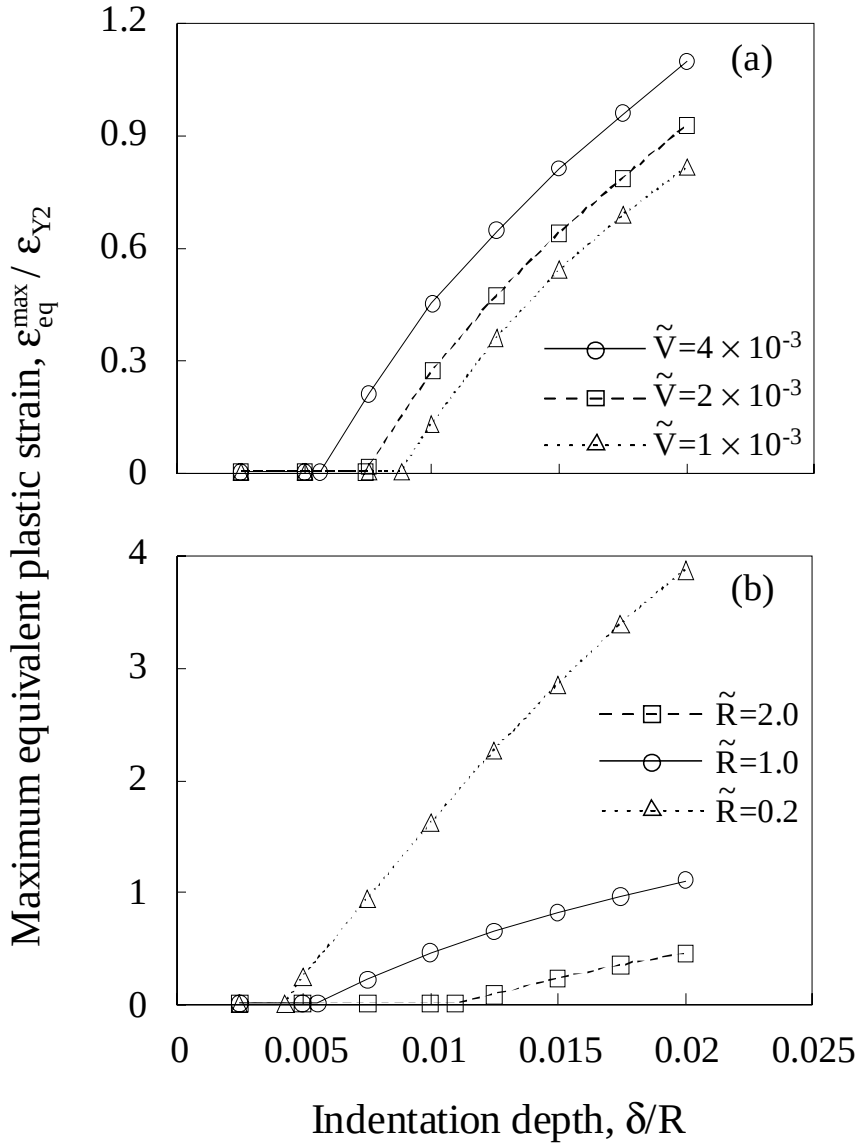

Fig. 3.14 Maximum equivalent plastic strain in the second (soft) layer of an elastic-plastic multi-layered medium indented by a rigid cylinder versus indentation depth for (a) varying indentation speed and constant indenter radius ($\tilde{R}$ = 1.0) and (b) varying indenter radius and constant indentation speed ($\tilde{V}$ = 4 × 10^{-3}).

To demonstrate the dependence of plasticity in the soft layer on indentation parameters, results for ε_{eq}^{max} obtained for different indentation depths during loading and unloading are plotted in Figs. 3.14 and 3.15, respectively. Increasing the indentation

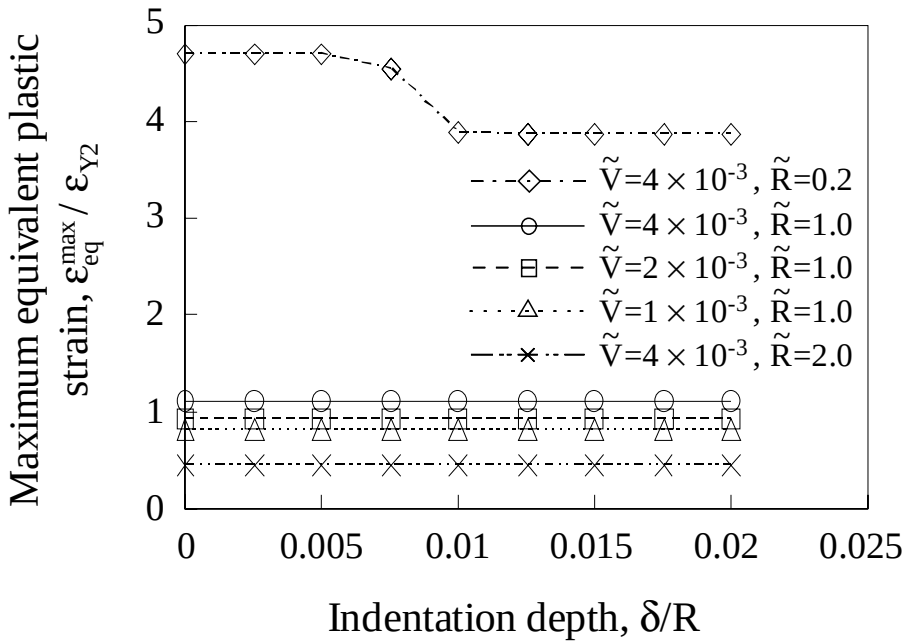

Fig. 3.15 Maximum equivalent plastic strain in the second (soft) layer of an elastic-plastic multi-layered medium indented by a rigid cylinder during unloading versus indentation depth for varying indentation speed and indenter radius.

speed and the sharpness of the indenter contributes to the premature yielding of the soft layer. For the range of parameters examined in this analysis, the critical indentation depth at the inception of yielding in the soft layer is predicted to be between 0.004 and 0.011, depending on the speed and radius of the indenter (Fig. 3.14). The dependence of $\varepsilon_{eq}^{\max}$ on indentation parameters (i.e., $\tilde{\delta}$, $\tilde{V}$, and $\tilde{R}$) exhibits trends similar to those observed for $\sigma_M^{\max}$ (Fig. 3.10) and $\sigma_I^{\max}$ (Fig. 3.12). Figure 3.15 shows that reyielding during unloading is controlled by the speed and radius of the indenter. Dynamic unloading from a maximum depth $\tilde{\delta}$ = 0.02 is shown to be fully elastic for all simulation cases except for that involving the relatively sharp indenter ($\tilde{R}$ = 0.2) and higher load/unload speed

($\tilde{V}$ = 4 × 10^{-3}). For this case, additional plastic deformation begins to accumulate in the soft layer as soon as the indenter is retracted to a depth $\tilde{\delta} \simeq 0.01$. The region where reyielding occurs in the soft layer is below the center of contact, close to the interface with the hard surface layer.

3.4.3 Residual Stress-Strain Field

As mentioned previously, damping was not included in the dynamic simulations of indentation loading and unloading. Consequently, after dynamic unloading, the multi-layered medium continued to oscillate without ever reaching equilibrium due to the reflection of the propagating waves from the boundaries. Therefore, as mentioned in section 3.2, to enable the analysis of the residual stress-strain field due to dynamic indentation, dashpot elements were added to the finite element mesh after full unloading. The damping coefficients of these elements were selected in order for the vibration of the unloaded medium to decrease within a short time. Since additional plastic deformation due to the vibration of the multi-layered medium does not occur, the residual stress-strain field can be obtained as soon as equilibrium is reached. Contours of residual σ_M and ε_{eq} are shown in Figs. 3.16 and 3.17, respectively, for different values of normalized indenter radius and indentation speed. The results obtained for the same indenter radius ($\tilde{R}$ = 1.0) reveal that increasing the indentation speed causes intensification of the residual stress in the hard surface layer, especially at the interface with the soft layer (Figs. 3.16(a)-3.16(c)), and promotes the development of higher residual plastic strains and a larger plastic zone in the soft layer (Figs. 3.17(a)-3.17(c)) below the center of contact. A comparison of Figs. 3.16(c) and 3.17(c) with Figs. 3.16(d) and 3.17(d),

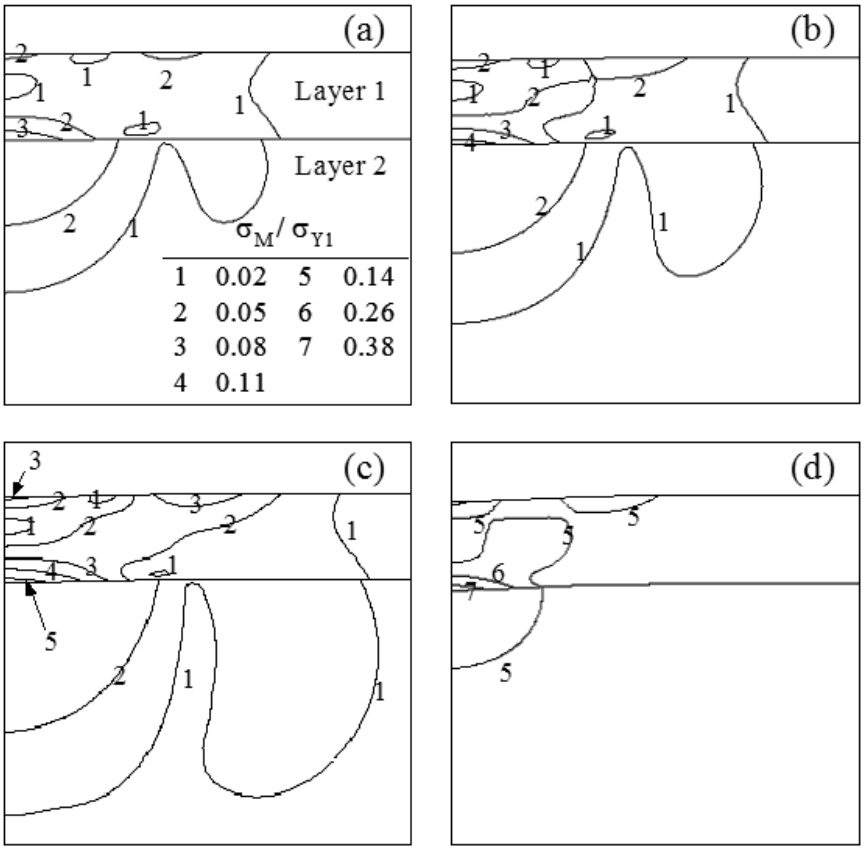

Fig. 3.16 Contours of residual von Mises equivalent stress in elastic-plastic multi-layered medium indented by a rigid cylinder after full unloading for different values of indentation speed and indenter radius: (a) $\tilde{V} = 1 \times 10^{-3}$, $\tilde{R} = 1.0$, (b) $\tilde{V} = 2 \times 10^{-3}$, $\tilde{R} = 1.0$, (c) $\tilde{V} = 4 \times 10^{-3}$, $\tilde{R} = 1.0$, and (d) $\tilde{V} = 4 \times 10^{-3}$, $\tilde{R} = 0.2$.

respectively, shows that the residual stresses and plastic strains in the hard and soft layers, respectively, increase significantly with the sharpness of the indenter, while the size of the plastic zone in the soft layer decreases slightly. The development of $\sigma_M^{\max}$ at the bottom of the hard layer below the center of contact is attributed to bending of the elastically deformed hard layer as the soft layer flows plastically. The resulting large stress gradients across the interface are associated with the occurrence of $\varepsilon_{eq}^{\max}$ in the soft

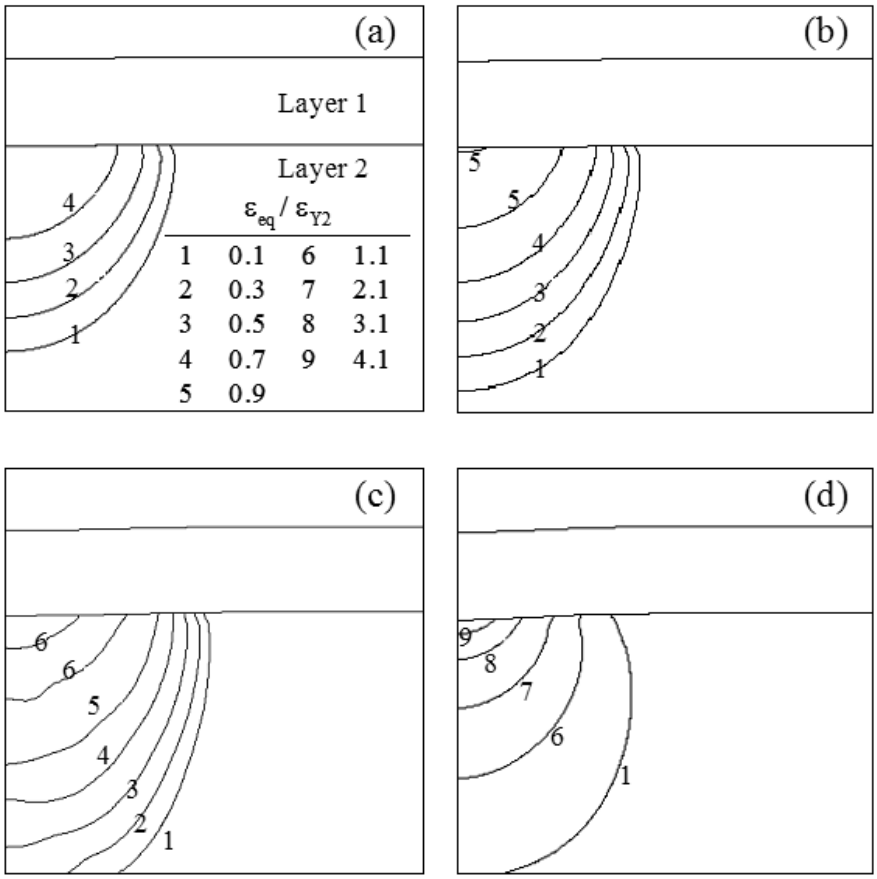

Fig. 3.17 Contours of residual equivalent plastic strain in elastic-plastic multi-layered medium indented by a rigid cylinder after full unloading for different values of indentation speed and indenter radius: (a) $\tilde{V} = 1 \times 10^{-3}$, $\tilde{R} = 1.0$, (b) $\tilde{V} = 2 \times 10^{-3}$, $\tilde{R} = 1.0$, (c) $\tilde{V} = 4 \times 10^{-3}$, $\tilde{R} = 1.0$, and (d) $\tilde{V} = 4 \times 10^{-3}$, $\tilde{R} = 0.2$.

layer adjacent to the region of $\sigma_M^{\max}$ at the bottom of the hard surface layer.

The results presented in this chapter demonstrate the effect of indentation depth, speed, and sharpness of the indenter on the elastic-plastic deformation and likelihood of cracking in multi-layered elastic-plastic media. The dynamic simulation results cannot be compared with those of a quasi-static plane strain analysis. This is because the latter analysis implies infinite simulation time and the results depend on the location of the

reference point. Alternatively, the dynamic results are obtained for a finite analysis time and are independent of a reference point. After a sufficiently long time the vibrations in the layered medium due to the reflected waves will be damped out (if damping is considered in the analysis) and the dynamic simulation results would approach those of a quasi-static analysis. To obtain such a comparison, the effects of the reflected waves and material damping, as well as the dependence of the results on the mesh size and boundary conditions, must be taken into account. However, this is beyond the scope of the present finite element analysis. The findings of this analysis provide explanation to phenomenological observations of mechanical failure in layered media due to excessive plastic flow and cracking in indentation experiments (e.g., Alfredsson and Olsson, 2000). The present finite element model can be easily extended to account for strain hardening and strain rate sensitivity effects under dynamic contact loading.

3.5 Conclusions

A plane-strain dynamic contact analysis for a multi-layered elastic-plastic medium indented by a rigid cylinder of varying radius of curvature was performed using the finite element method. Solutions for the contact force, contact pressure, and subsurface stresses and strains were obtained in terms of penetration depth, indenter radius, and indentation speed for both loading and unloading. Based on the presented results and discussion, the following main conclusions can be drawn.

(1) For dynamic contact analysis of semi-infinite half-spaces using the finite element technique, a sufficiently large mesh is required for the faster propagating dilatational waves that are reflected from the mesh boundaries not to reach the region of interest during the analysis. In this region, the simulation results are

independent of mesh dimensions, and specifying a reference point in order to obtain the displacement field (as in plane-strain quasi-static analyses) is not necessary.

(2) Wave propagation in the multi-layered medium examined in this analysis is dominated by the material properties of the thick substrate (fourth layer) of the half-space medium.

(3) The contact load, contact pressure, and subsurface stresses and plastic strains (both loading and residual) increase with indentation depth and speed. For the material properties and indentation parameters examined in this analysis, higher indentation speed leads to premature yielding and plastic zone formation in the second (soft) layer and higher tensile stresses in the elastically deformed surface (hard) layer.

(4) Smaller critical indentation depth at the inception of yielding, higher peak contact pressure, lower contact load, and intensified subsurface stress-strain field are obtained with a sharper indenter. Due to the relatively high yield strength of the surface layer, the peak value of the maximum von Mises equivalent stress occurs always in this layer, whereas the peak equivalent plastic strain arises always in the second layer.

(5) Results for the peak values and locations of the maximum von Mises equivalent stress, first principal stress, and maximum equivalent plastic strain, as well as the evolution of the plastic zone during indentation loading and unloading, were obtained in terms of indentation parameters. The finite element solutions provide insight into the propensity for plastic flow and cracking in dynamically indented multi-layered media.

CHAPTER 4

Dynamic Contact Between an Elastic-Plastic Multi-Layered Medium and a Rigid Fractal Surface

4.1 Introduction

The longevity of the protective hard and tough surface layers depends on the knowledge of the effects of the layer thickness and material properties on the deformation and stress fields due to surface traction. Contact stress analysis of elastic-layered media has received considerable research attention in the field of contact mechanics (Burmister (1945); Dhaliwal et al. (1970); Gupta and Walowit (1974); King and O'Sullivan (1987)). With the advent of numerical techniques, such as finite element method, and the increase of computational capabilities, significant advances in the study of elastic-plastic contact deformation were also encountered (Kennedy and Ling (1974); Komvopoulos (1989); Kral et al. (1995a and 1995b); Gan and Ben-Nissan (1997); Sen et al. (1998); Faulkner et al. (1998)).

The above-mentioned studies dealing with perfectly smooth contact interfaces are informative of the global deformation behavior, which is dictated by the macroscopic shape of the interacting solids. However, the local deformation behavior may differ significantly due to multi-scale roughness effects. For example, numerical simulations by Webster and Sayles (1986) have shown that the contact pressure distribution and the normal load versus real contact area relationship of rough surfaces markedly deviated from those of perfectly smooth surfaces. Thus, in order to capture the microscopic deformation occurring in the vicinities of the asperity contacts, where actual solid-solid

contact occurs, accurate representation of the surface topography over a wide range of length scales is essential. The dependence of surface topography parameters, such as variance, skewness, and kurtosis of the surface height distribution, on the sample size and resolution limit of the measuring device and the self-affinity behavior of many engineering surfaces have led to the characterization of the surface topography by fractal geometry (Majumdar and Tien, 1990; Majumdar and Bhushan, 1990). Majumdar and Bhushan (1991) developed a two-dimensional contact model of rough surfaces described by fractal geometry, and predicted that all the asperity contacts of area less than a critical value deform plastically. Yan and Komvopoulos (1998a) presented a three-dimensional contact analysis of elastic-plastic fractal surfaces that elucidated the effects of surface topography parameters and material properties on the evolution of elastic and plastic deformation at the contact interface. Later, Komvopoulos and Ye (2001) extended the previous analysis to include elastic, elastic-plastic, and fully plastic deformation of the asperity contacts, and obtained results illustrating the dependence of the normal load on fractal parameters. The same authors used fractal geometry to describe the equivalent surface topography of the head-disk interface and investigated the evolution of plasticity and likelihood of crack initiation in the multi-layered hard disk (Komvopoulos and Ye, 2002).

The knowledge derived from previous contact analyses dealing with homogeneous and layered media possessing either smooth or rough surface topographies has paved the way toward more accurate modeling of contact deformation. However, because most of these studies are limited to static or quasi-static contact loads, the reported solutions may not be applicable to dynamic contacts. For example, Streator

(2003) used a numerical model to analyze dynamic contact between a rigid sphere and an elastic half-space and found that the maximum contact load was significantly higher than that for quasi-static contact, even for indentation speeds much less than the speed of the dilatational waves. In chapter 3, a finite element analysis of dynamic indentation of a multi-layered medium by a rigid cylinder with a smooth surface profile is reported and the requirement for the finite element mesh size in order to obtain results that are not biased by the waves reflected from the artificial boundaries of the half-space is also discussed. The objective of this chapter is to extend the previous analysis to the more realistic case of an elastic-plastic layered medium in dynamic contact with a rough surface characterized by fractal geometry. The effects of the layer thickness and indentation speed on the contact pressure and subsurface stress/strain fields and the possibility of elastic shakedown during cyclic indentation are interpreted in the context of the obtained finite element results.

4.2 Rough-Surface Model and Finite Element Simulations

4.2.1 Rough-Surface Model.

For an unbiased description of the surface topography and in order to include multi-scale length effects in the present analysis, the equivalent surface topography was characterized by fractal geometry (Mandelbrot, 1967). The traditional approach in contact analyses of fractal surfaces is to represent a two-dimensional surface profile, $z(x)$, by an approximate (truncated) Weierstrass-Mandelbrot function (Berry and Lewis, 1980), which, for dimensional consistency, can be written as (Wang and Komvopoulos, 1994)

$$z(x) = L_x \left(\frac{G}{L_x} \right)^{(D-1)} \sum_{n=0}^{M} \frac{\cos\left(2\pi\gamma^n x / L_x\right)}{\gamma^{(2-D)n}}, \tag{4.1}$$

where x is the horizontal direction, L_x is the fractal sample length, G is the fractal roughness, D is the fractal dimension ($1 < D < 2$), γ ($\gamma > 1$) is a scaling parameter (typically, $\gamma = 1.5$ (Yan and Komvopoulos, 1998a)), which controls the relative phase differences between fractal modes, and M is the highest frequency index, which is related to the cut-off length, L_c, and the sample length by $M = \text{int}[\log(L_x/L_c)/\log\gamma]$.

The rough surface used in the finite element simulations was obtained from Eq. (4.1) using the fractal parameters of the equivalent surface of an ultra-smooth hard disk and a carbon-coated slider, $D = 1.44$ and $G = 9.46 \times 10^{-4}$ nm (Komvopoulos, 2000). Since modeling of the entire surface profile is impractical and computationally prohibitive, a segment of the profile was selected for dynamic contact analysis based on the procedure developed in a previous study (Komvopoulos and Ye, 2002). Since all the truncated segments of a surface profile exhibit self-affinity over ranges that include all the wavelengths comprising the surface profile (Eq. (4.1)), any segment of length several orders of magnitude larger than the simulated maximum interference should yield a similar deformation behavior (Komvopoulos and Ye, 2002). The critical surface segment was determined by truncating the entire surface profile (4379 nm in length) to a maximum interference of 2 nm. The profile segment determined from this procedure (Fig. 4.1) is about 100 times larger than the simulated local interference and contains the largest number of asperity contacts. The dashed line shown in Fig. 4.1 represents the undeformed surface of the multi-layered medium. The local interference, δ, is defined as

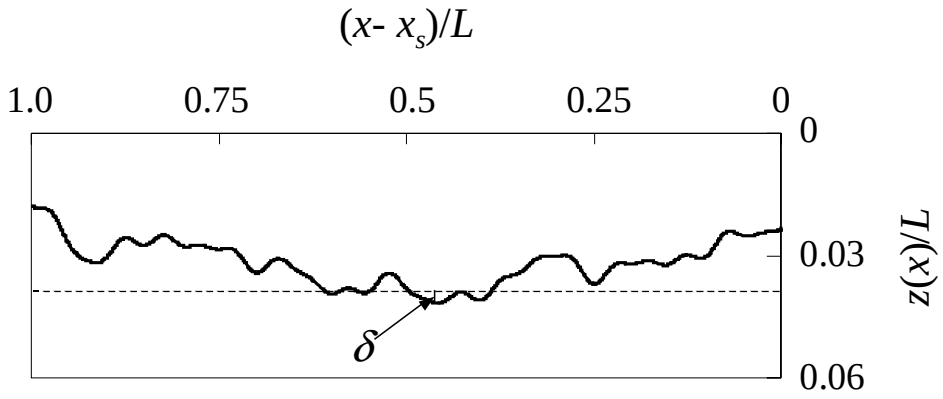

Fig. 4.1 Segment of a two-dimensional fractal profile generated from Eq. (1) using D = 1.44, $G = 9.46 \times 10^{-4}$ nm, γ= 1.5, L_x = 4379 nm, and L_c = 10 nm.

the maximum interference in this segment. The origin of the rough-surface segment is denoted by x_s. The segment length, L, was used to normalize all the length parameters. More details about the characterization of the surface topography by fractal geometry can be found in previous publications (Komvopoulos and Ye, 2002; Wang and Komvopoulos, 1994; Yan and Komvopoulos, 1998a).

4.2.2 Finite element mesh and material properties of the layered medium.

As discussed in chapter 2 and 3, wave propagation plays an important role in dynamic contact analysis. To avoid the effects of the mesh boundaries on the results, sufficiently large finite element meshes were used in order for the waves reflected from the artificial boundaries not to affect the results in the analyzed domain of the multi-layered medium (chapter 3). However, the effects of the waves reflected from the layer interfaces were included in the analysis because of their close proximity to the region of analysis. Figures 4.2(a) and 4.2(b) show the finite element meshes of multi-layered media

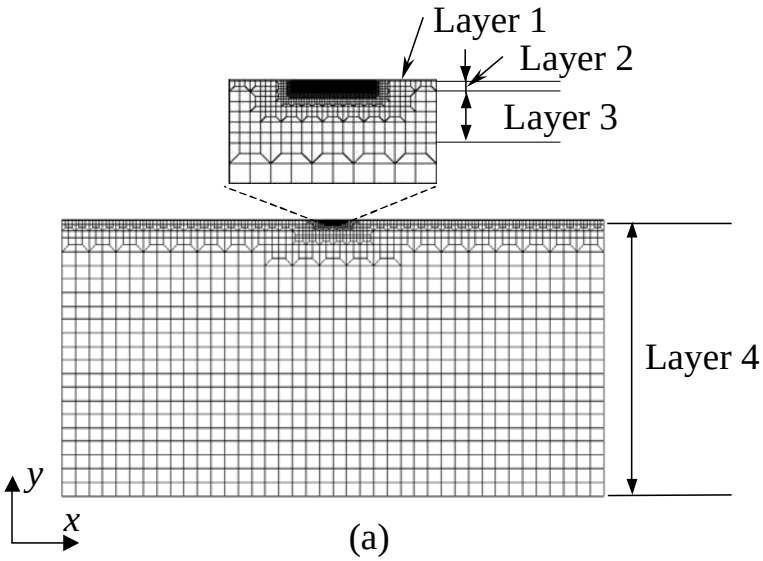

(a)

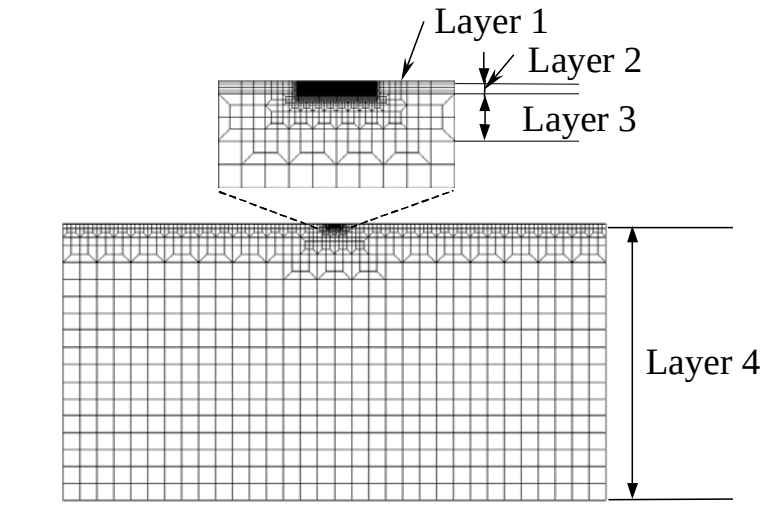

(b)

Fig. 4.2 Finite element mesh of a multi-layered medium with a surface-layer thickness (a) $\tilde{h}_1$ = 0.01 and (b) $\tilde{h}_1$ = 0.025.

Table 4.1. Thickness and material properties of the elastic-plastic multi-layered medium subjected to dynamic indentation of a rigid, rough surface

Layer	Normalized thickness (h/L)	Elastic modulus (GPa)	Yield strength (GPa)	Mass density (kg/m^3)	Poisson ratio
1	0.01, 0.025	168	13.0	2266	0.3
2	0.078	130	2.67	8800	0.3
3	0.40	140	2.58	7000	0.3
4	25.6	160	2.67	8000	0.3

Sources: Kaye (1986) and Komvopoulos (2000).

with surface-layer thickness equal to $0.01L$ and $0.025L$, consisting of 9270 and 7854 eight-node, bi-quadratic, plane-strain elements with a 3×3 Gauss integration scheme, respectively. For greater numerical accuracy, the near-surface regions of the meshes were refined with small square elements of size equal to $0.0025L$ and $0.003125L$, i.e., one-fourth and one-eighth of the thickness of the surface layer in Figs. 4.2(a) and 4.2(b), respectively. The size of the meshes shown in Figs. 4.2(a) and 4.2(b) are $51.2L \times 26.088L$ and $51.2L \times 26.103L$. All the nodes at the bottom boundary were constrained against displacement in the y direction. In addition, the middle-node at the bottom boundary was constrained against displacement in the x direction to prevent rigid body rotation. The normalized thickness and material properties of the multi-layered medium (Kaye, 1986; Komvopoulos, K., 2000) are listed in Table 4.1. The material properties are typical of magnetic thin-film disks. A Poisson ratio of 0.3 and elastic-perfectly plastic behavior was

assumed for all the layers. The classical von Mises yield criterion was used to determine whether yielding occurred at an integration point at different interferences.

4.2.3 Dynamic Contact Simulations.

Dynamic indentation was simulated in a fashion similar to chapter 3. Contact between the rough surface and the multi-layered medium was detected by second-order contact elements assigned to the surface of the deformable medium. In view of the secondary effect of friction in normal contact (Komvopoulos, 1988), frictionless contact was assumed in all the simulations. A node with a fixed *x* coordinate was used to control the vertical movement of the rough surface. This node was also used as the reference node of the contact elements. Based on a displacement-controlled scheme, an indentation cycle was modeled by displacing the rough surface toward the multi-layered medium at a constant velocity and, upon reaching the set interference, retracting it back to its original position by following the same steps as for the loading.

Simulations were performed for an indentation load/unload speed between $0.001\,c_P^{(4)}$ and $0.004\,c_P^{(4)}$, where $c_P^{(4)}$ is the propagation speed of the plane dilatational waves in the fourth layer. In the following section, results are presented in terms of dimensionless indentation speed, $\tilde{V}$, obtained by dividing the indentation speed by $c_P^{(4)}$. Although material damping was ignored in the loading and unloading phases of an indentation cycle, to determine the residual stresses and strains, dashpot elements were added to the mesh after the unloading phase of each indentation cycle. The damping coefficients of the dashpot elements were selected to achieve static equilibrium in a relatively short computation time. Subsequently, the dashpot elements were removed and the next indentation cycle was simulated in a manner identical to that of the previous

cycle. For increased accuracy and expeditious convergence, all the simulations were performed with the ABAQUS/Standard finite element package (implicit integration) instead of the generally faster ABAQUS/Explicit package (explicit integration). The typical CPU time for simulating indentation loading (or unloading) with a Pentium III 550 processor was equal to 13-14 hours, while the CPU time for a complete load/unload indentation cycle, including the time required to achieve equilibrium after full unloading, was of the order of ~56 hours.

4.3 Results and Discussion

Simulation results for the contact pressure distribution and subsurface stress and strain fields in the multi-layered medium are presented in this section in terms of normalized interference, $\tilde{\delta} = \delta / L$, indentation speed, $\tilde{V} = V / L$, and surface-layer thickness, $\tilde{h}_1 = h_1 / L$. As mentioned earlier, the length of the simulated profile segment, *L*, was used to normalize all the dimensional parameters. The likelihood for plastic deformation and crack initiation is discussed in terms of the von Mises equivalent stress, equivalent plastic strain, and first principal (maximum tensile) stress obtained in the loading and unloading phases of each indentation cycle. The possibility of elastic shakedown is also interpreted in the context of the reyielding behavior of the multi-layered medium due to cyclic indentation. Unless otherwise stated, the results discussed in the following section are for the loading and unloading phases of a single indentation cycle. However, it will be shown later that the single-indentation results obtained for the multi-layered medium with the relatively thicker surface layer ($\tilde{h}_1$ = 0.025) are also valid for cyclic indentation.

4.3.1 Single Indentation

4.3.1.1 Contact Force and Pressure Distribution

Figure 4.3 shows the variation of the contact force, P/P_Y, with the interference, $\tilde{\delta}$, for different values of the indentation speed, $\tilde{V}$, and surface-layer thickness, $\tilde{h}_1$. The (critical) contact load at the inception of yielding in the multi-layered medium with the thinner surface layer ($\tilde{h}_1$ = 0.01) for a relatively high indentation speed ($\tilde{V}$ = 0.004) is denoted by P_Y. In all the simulated cases, the contact force increases monotonically with the interference. The increase of the contact force with the indentation speed at a given interference indicates an enhancement of the penetration resistance at high loading rates. This can be explained by considering the dependence of the energy dissipated in the multi-layered medium on the indentation speed. In high-speed indentation, a larger fraction of the external work is converted to kinetic energy, and larger displacement gradients (i.e., higher strains and strain energy) develop in the vicinities of the asperity contacts. Consequently, a higher indentation speed produces a larger contact force at a given interference, in accord with the findings of chapter 3. The close agreement of the force-interference responses shown in Figs. 4.3(a) and 4.3(b) indicates that, for the ranges of the varied parameters, the contact force is relatively insensitive to the surface-layer thickness. This is attributed to the small thickness of the surface layer compared to those of the underlying layers. Thus, despite the significantly higher elastic modulus and yield strength of the surface layer, the effect of its mechanical properties on the global dynamic response of the multi-layered medium is secondary.

Figures 4.4 and 4.5 show the effects of the indentation speed, interference, and

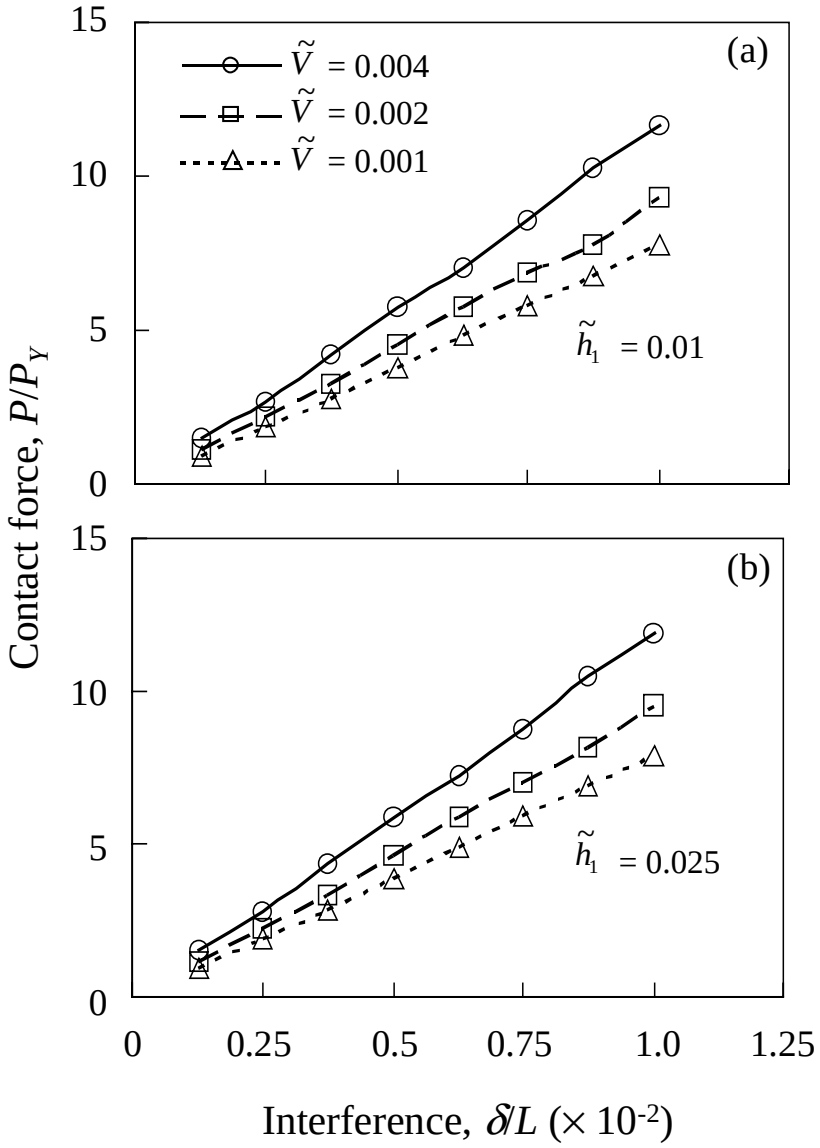

Fig. 4.3 Contact force versus interference for indentation speed $\tilde{V}$ = 0.001, 0.002, and 0.004 and surface layer thickness (a) $\tilde{h}_1$ = 0.01 and (b) $\tilde{h}_1$ = 0.025.

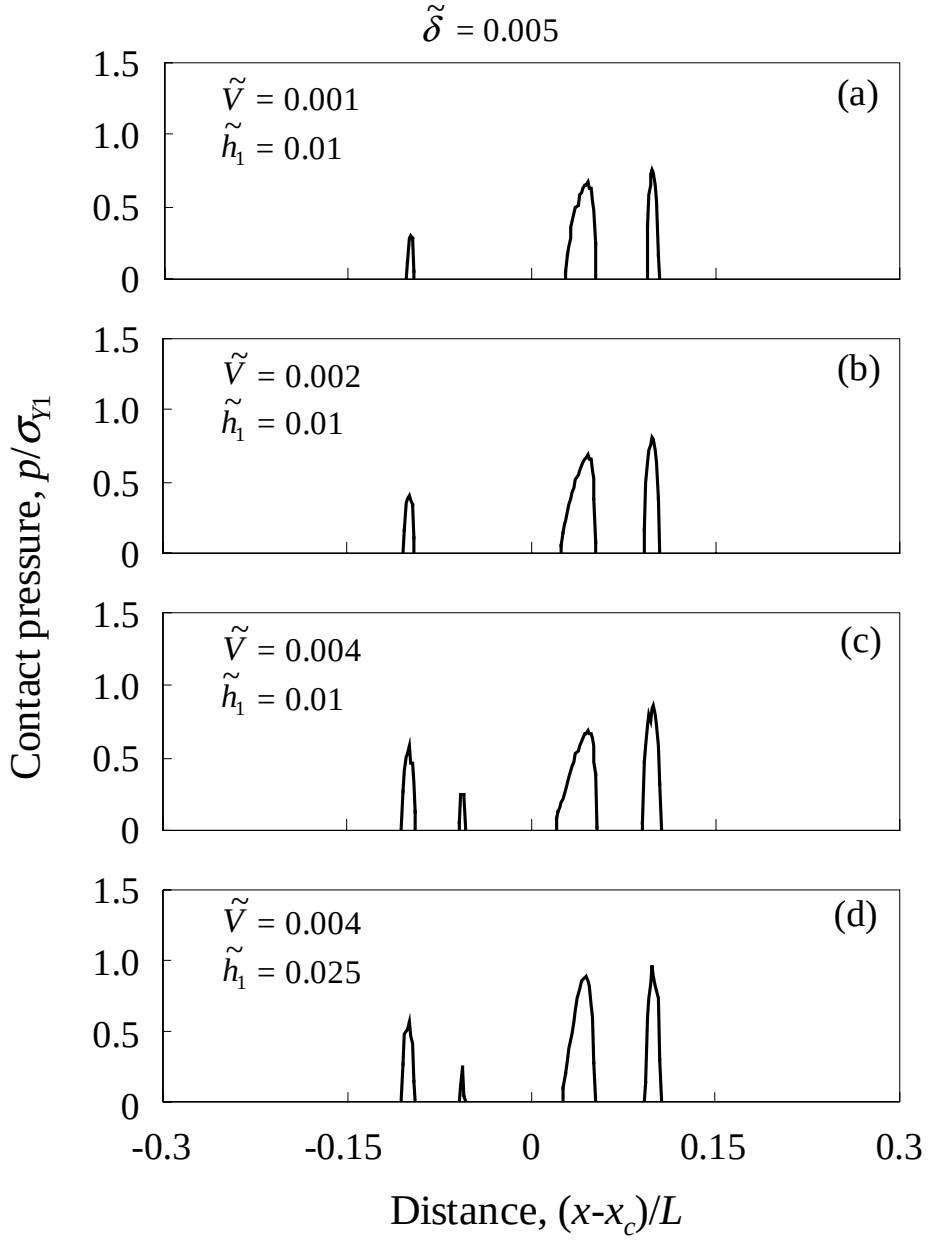

Fig. 4.4 Contact pressure distributions on an elastic-plastic multi-layered medium indented by a rigid and rough surface for interference $\tilde{\delta}$ = 0.005 and different indentation speed and surface-layer thickness: (a) $\tilde{V}$ = 0.001, $\tilde{h}_1$ = 0.01, (b) $\tilde{V}$ = 0.002, $\tilde{h}_1$ = 0.01, (c) $\tilde{V}$ = 0.004, $\tilde{h}_1$ = 0.01, and (d) $\tilde{V}$ = 0.004, $\tilde{h}_1$ = 0.025.

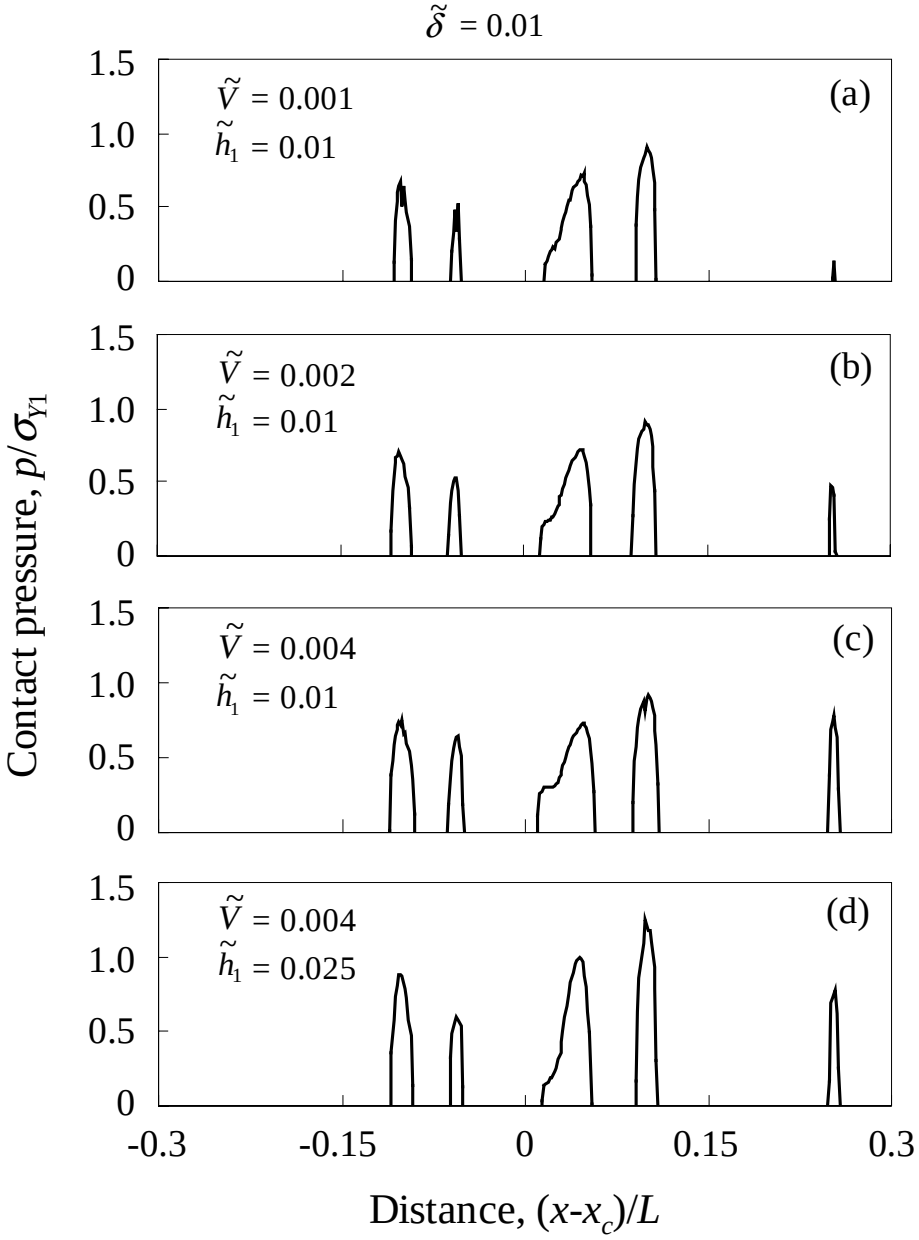

Fig. 4.5 Contact pressure distributions on an elastic-plastic multi-layered medium indented by a rigid, rough surface for interference $\tilde{\delta}$ = 0.01 and different indentation speed and surface-layer thickness: (a) $\tilde{V}$ = 0.001, $\tilde{h}_1$ = 0.01, (b) $\tilde{V}$ = 0.002, $\tilde{h}_1$ = 0.01, (c) $\tilde{V}$ = 0.004, $\tilde{h}_1$ = 0.01, and (d) $\tilde{V}$ = 0.004, $\tilde{h}_1$ = 0.025.

surface-layer thickness on the contact pressure distribution. The contact pressure, p, is normalized by the yield strength of the surface layer, σ_{Y1}, and the distance from the center of the modeled surface profile, $x - x_c$, by the length of the profile, L. The maximum contact pressure at each asperity contact intensifies with the increase of the interference. In addition, Figs. 4.4(a)-4.4(c) and Figs. 4.5(a)-4.5(c) show that, for a fixed interference and surface-layer thickness, both the real contact area and the maximum contact pressure increase with the indentation speed and, in the case shown in Fig. 4.4(c), more asperity contacts are established. These trends provide explanation for the variation of the contact force with the indentation speed for fixed interference and surface-layer thickness (Fig. 4.3). Moreover, a comparison of Figs. 4.4(c), 4.4(d), 4.5(c), and 4.5(d) shows that the increase of the surface-layer thickness intensifies the maximum contact pressure and decreases the real contact area. This is because the effect of the mechanical properties of the surface layer on the conformity of the multi-layered medium with the rough surface becomes more pronounced with the increase of the surface-layer thickness.

4.3.1.2 Subsurface Stresses

Figure 4.6 shows contours of normalized von Mises equivalent stress, σ_M/σ_{Y1}, in the multi-layered medium with the thinner surface layer ($\tilde{h}_1$ = 0.01) for a relatively high indentation speed ($\tilde{V}$ = 0.004). The high-magnification regions show the distribution of the von Mises stress in the highly stressed near-surface regions. The discontinuities of the stress contours at the layer interface are due to the mismatch of the material properties of the two layers. Similar discontinuities can be observed in the stress and strain contours of similar figures presented in following sections. For a relatively small interference $\tilde{\delta}$ =

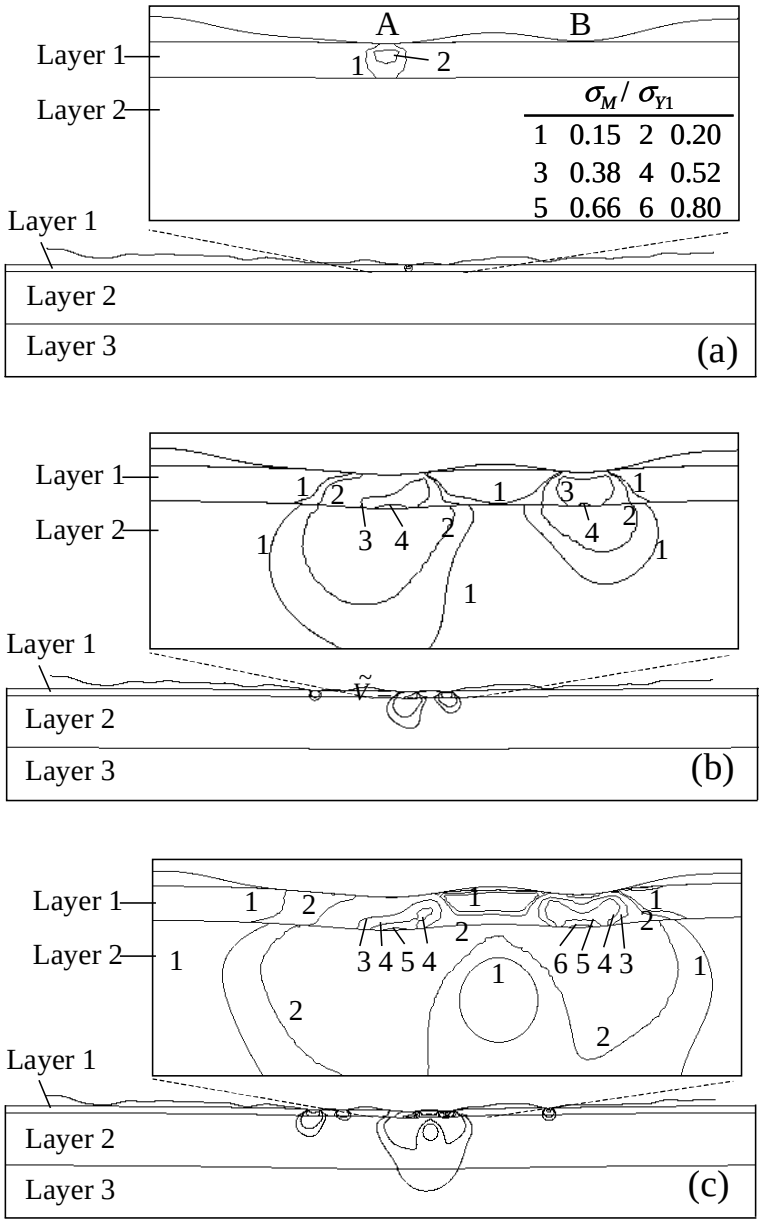

Fig. 4.6 Contours of von Mises equivalent stress in an elastic-plastic multi-layered medium with a surface-layer thickness $\tilde{h}_1$ = 0.01 indented by a rigid, rough surface for indentation speed $\tilde{V}$ = 0.004 and interference (a) $\tilde{\delta}$ = 0.0005, (b) $\tilde{\delta}$ = 0.005, and (c) $\tilde{\delta}$ = 0.01.

0.0005 (Fig. 4.6(a)), $\sigma_M^{\max}$ occurs in the surface layer below the first established asperity contact A, and is much higher than that below asperity contact B. New asperity contacts are produced at larger interferences (Figs. 4.6(b) and 4.6(c)), and the highest von Mises stresses occur at the bottom of the surface layer, adjacent to the interface with the second layer. It is noted that $\sigma_M^{\max}$ in the surface layer is always higher than that in the second layer. It can be seen that $\sigma_M^{\max}$ below asperity contact B increases faster than that below asperity contact A due to the grater sharpness of asperity B. For an intermediate interference ($\tilde{\delta}$ = 0.005), the values of $\sigma_M^{\max}$ below asperity A and B are similar. However, for a large interference ($\tilde{\delta}$ = 0.01), $\sigma_M^{\max}$ occurs below asperity contact B. Thus, for a large interference, the sharper asperity B produces a higher $\sigma_M^{\max}$ stress at the layer interface (Fig. 4.6(c)), while for a small interference, the blunt asperity A produces a higher $\sigma_M^{\max}$ stress in the first layer adjacent to the contact region (Fig. 4.6(a)). Qualitatively similar results were obtained from the low-speed indentation simulations (i.e., $\tilde{V}$ = 0.001), though the stresses were generally lower.

Figure 4.7 shows the variation of the normalized maximum von Mises stress, $\sigma_M^{\max}/\sigma_{Y1}$, in the surface layer with the interference for different values of indentation speed and surface-layer thickness. For both values of the surface-layer thickness, $\sigma_M^{\max}$ increases with the interference independent of indentation speed. In addition, $\sigma_M^{\max}$ intensifies with the increase of the indentation speed in a similar fashion as the contact force (Fig. 4.3). Although the effect of the surface-layer thickness on the magnitude of $\sigma_M^{\max}$ is negligible for interferences significantly less than the layer

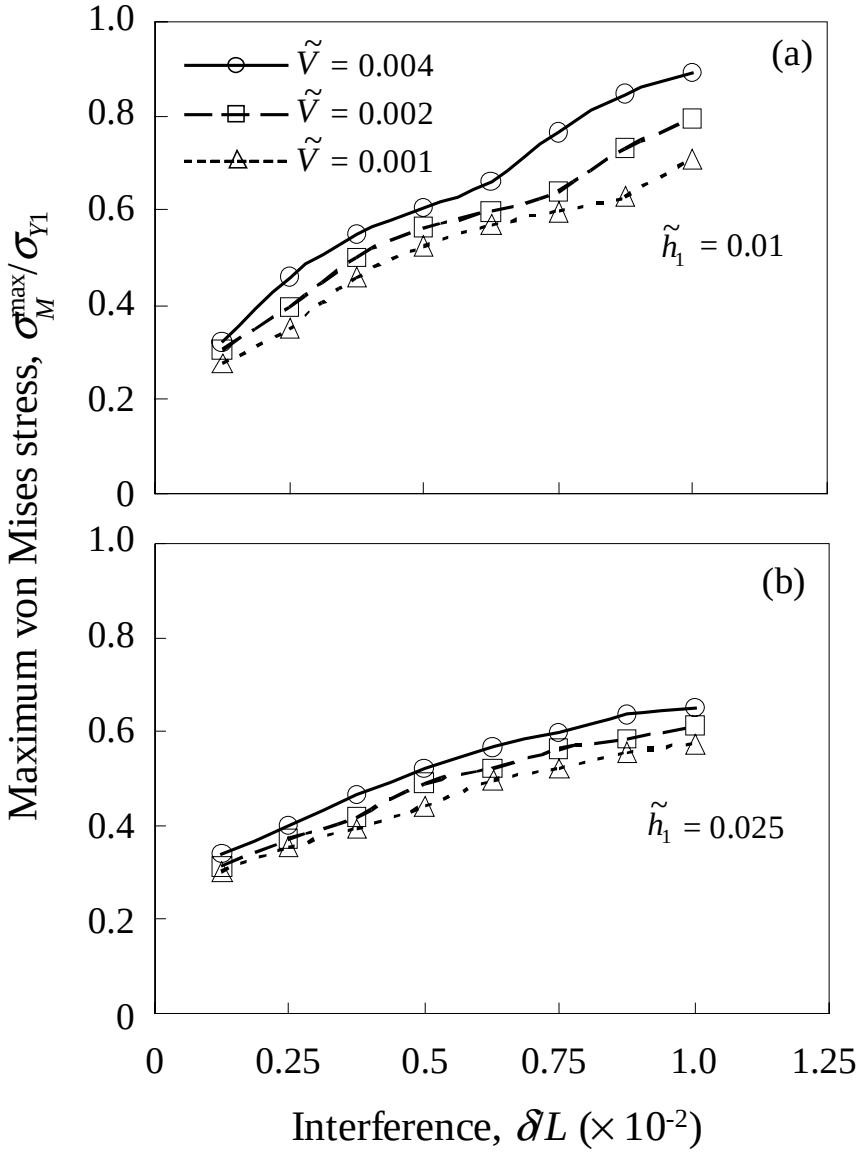

Fig. 4.7 Maximum von Mises equivalent stress in the first layer of an elastic-plastic multi-layered medium indented by a rigid, rough, surface versus interference for indentation speed $\tilde{V}$ = 0.001, 0.002, and 0.004 and surface-layer thickness (a) $\tilde{h}_1$ = 0.01 and (b) $\tilde{h}_1$ = 0.025.

thickness (e.g., $\tilde{\delta}$ < 0.0025 << $\tilde{h}_1$), a much lower $\sigma_M^{\max}$ stress is produced with the thicker layer at a relatively large interference (e.g., $\tilde{\delta}$ = 0.01). As discussed earlier, this result can be attributed to the exacerbated influence of the material properties of the surface layer on the mechanical response of the multi-layered medium when $\tilde{\delta}$ << $\tilde{h}_1$. It is also noted that even though the contact pressure may exceed the yield strength of the surface layer (e.g., Fig. 4.5(d)), the corresponding curve ($\tilde{V}$ = 0.004 and $\tilde{h}_1$ = 0.025), shown in Fig. 4.7(b), reveals that the surface layer deforms only elastically.

The likelihood of subsurface crack initiation can be interpreted in terms of the first principal (maximum tensile) stress, σ_I. Figure 4.8 shows contours of normalized first principal stress, σ_I / σ_{Y1}, in the first and second layers for different interferences and high indentation speed. Similar to $\sigma_M^{\max}$ (Fig. 4.6), $\sigma_I^{\max}$ always occurs in the surface layer below the asperity contacts. Therefore, domains around the location of $\sigma_I^{\max}$ are shown in Figs. 4.8(a)-4.8(d). For a small interference ($\tilde{\delta}$ = 0.00375), $\sigma_I^{\max}$ arises at the layer interface below asperity contact A (Fig. 4.8(a)). The increase of the interference intensifies the tensile stress and shifts the location of $\sigma_I^{\max}$ at the layer interface below the sharper asperity B (Figs. 4.8(b) and 4.8(c)). The contours of residual σ_I stress obtained after the first indentation cycle (Fig. 4.8(d)) illustrate an enlargement of the interface regions of tensile stress below the asperity contacts. The contour plots shown in Fig. 4.8 demonstrate a higher probability for crack initiation at the layer interface during the loading and/or unloading phases of dynamic indentation.

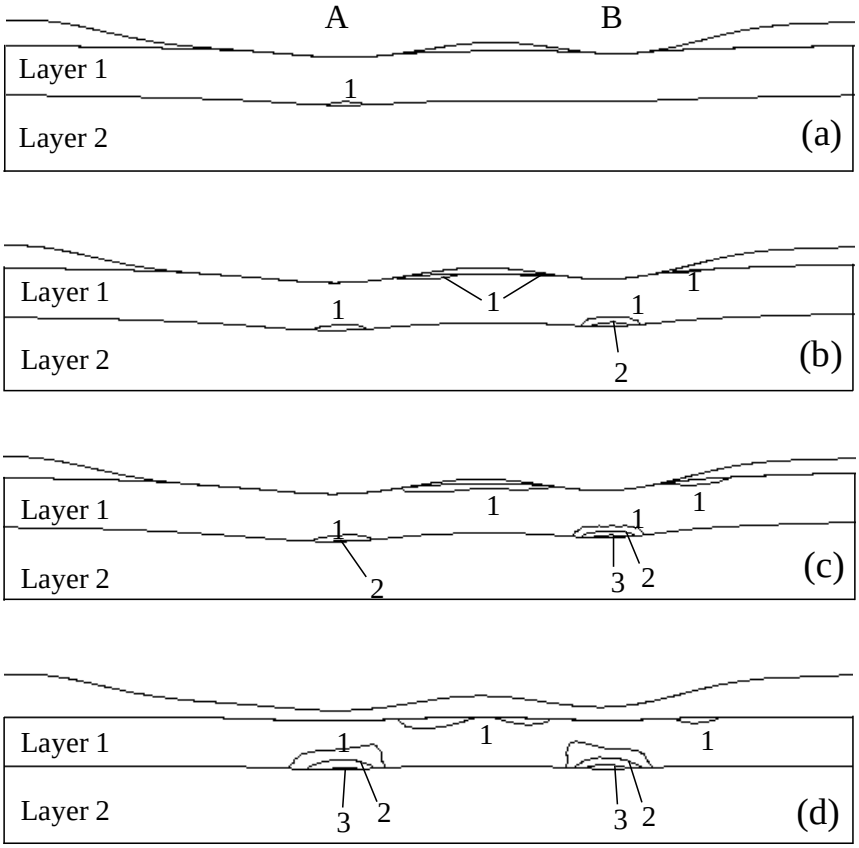

Fig. 4.8 Contours of first principal stress in the first and second layers of an elastic-plastic multi-layered medium with a surface-layer thickness $\tilde{h}_1$ = 0.01 indented by a rigid, rough surface for indentation speed $\tilde{V}$ = 0.004 and interference (a) $\tilde{\delta}$ = 0.00375, (b) $\tilde{\delta}$ = 0.0075, (c) $\tilde{\delta}$ = 0.01, and (d) $\tilde{\delta}$ = 0 (full unloading).

Figure 4.9 shows the dependence of $\sigma_I^{\max}$ on the indentation speed and surface-layer thickness. Although $\sigma_I^{\max}$ increases primarily with the interference and secondarily with the indentation speed similar to the $\sigma_M^{\max}$ stress (Fig. 4.7), the effect of the surface-layer thickness on $\sigma_I^{\max}$ is more pronounced compared to $\sigma_M^{\max}$. The markedly higher tensile stress at the bottom of the thinner ($\tilde{h}_1$ = 0.01) layer is due to the increase of bending deformation in the stiff surface layer with the decrease of its thickness, in accord

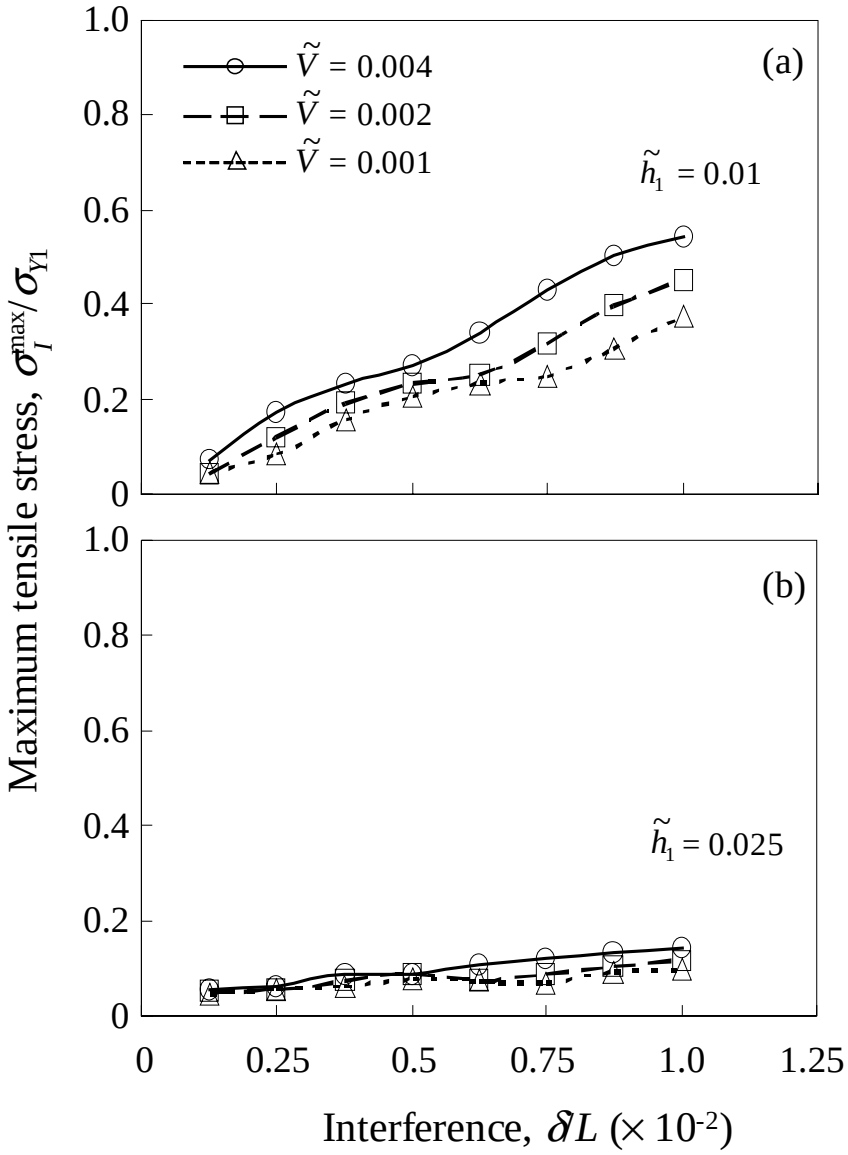

Fig. 4.9 Maximum first principal stress in the surface layer of an elastic-plastic multi-layered medium indented by a rigid, rough surface versus interference for indentation speed $\tilde{V}$ = 0.001, 0.002, and 0.004 and surface-layer thickness (a) $\tilde{h}_1$ = 0.01 and (b) $\tilde{h}_1$ = 0.025.

with the findings of chapter 3. This reveals a strong dependence of interface delamination on the thickness and elastic modulus of the surface layer.

4.3.1.3 Subsurface Plasticity.

The equivalent plastic strain can be used to quantify the effect of different parameters on the development of plasticity in the multi-layered medium. Figure 4.10 shows contours of normalized equivalent plastic strain, $\varepsilon_{eq}/\varepsilon_{Y2}$, below asperity contacts A and B for thin surface layer ($\tilde{h}_1$ = 0.01) and high indentation speed ($\tilde{V}$ = 0.004). Because of the higher yield strength of the surface layer, plasticity occurs only in the second (soft) layer. Plastic deformation commences at the layer interface below the larger (blunter) asperity A (Fig. 4.10(a)). The increase of the interference causes the plastic zone to grow only into the second layer and a new plastic zone to form below the smaller (sharper) asperity B (Fig. 4.10(b)). The peak value of ε_{eq} in the plastic zone below asperity B intensifies faster than that in the plastic zone below asperity A due to the greater sharpness of asperity B. For a larger interference (Fig. 4.10(c)), a new plastic zone develops at the interface, just below the newly established asperity contact to the left of asperity A, and $\varepsilon_{eq}^{\max}$ arises in the plastic zone below asperity B. This trend is similar to that of the von Mises equivalent stress (Fig. 4.6). However, regardless of the interference, the largest plastic zone always occurs below the relatively blunter asperity A. These results illustrate the significance of the asperity radius of curvature (sharpness) and contact size on the evolution of subsurface plasticity.

Figure 4.11 shows the dependence of the maximum equivalent plastic strain,

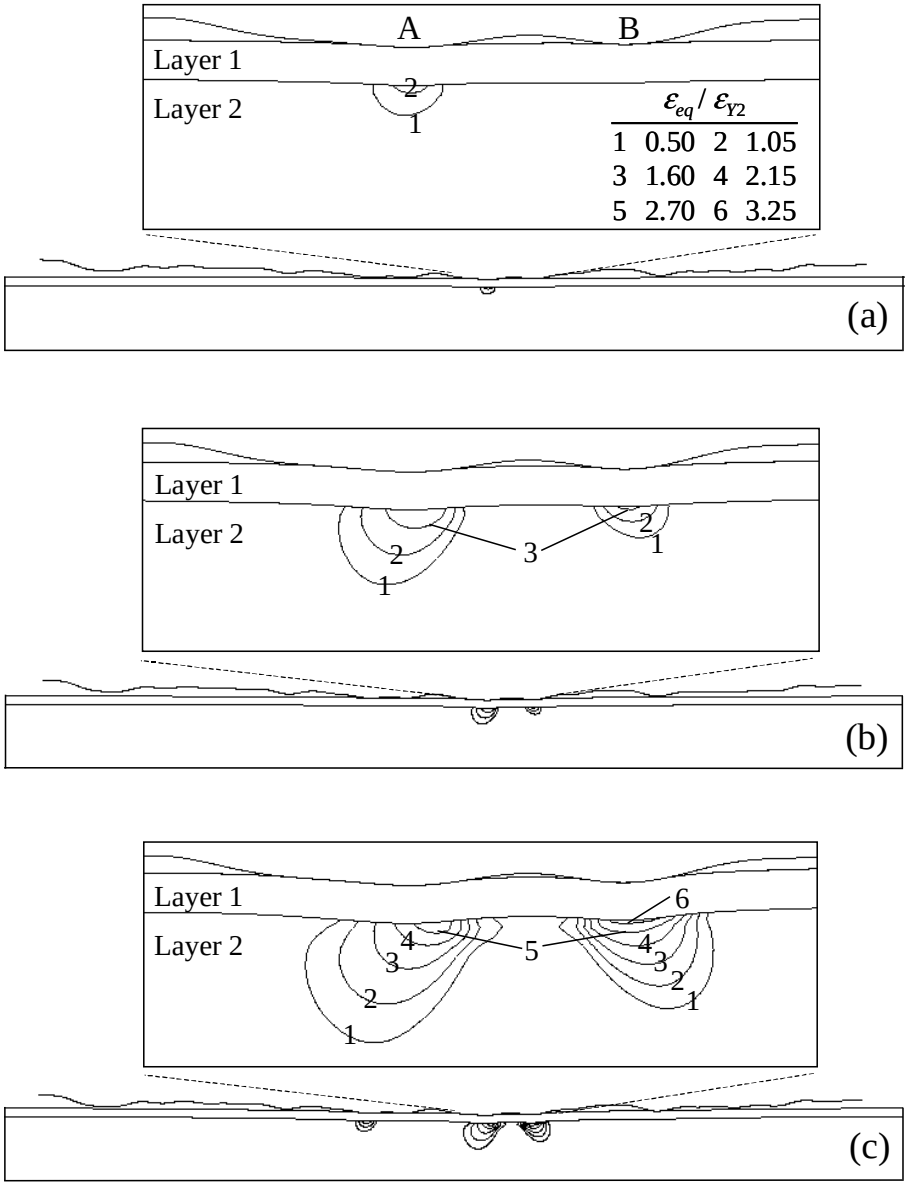

Fig. 4.10 Contours of equivalent plastic strain in the first and second layers of an elastic-plastic multi-layered medium with a surface-layer thickness $\tilde{h}_1$ = 0.01 indented by a rigid, rough surface for indentation speed $\tilde{V}$ = 0.004 and interference (a) $\tilde{\delta}$ = 0.0025, (b) $\tilde{\delta}$ = 0.005, and (c) $\tilde{\delta}$ = 0.01.

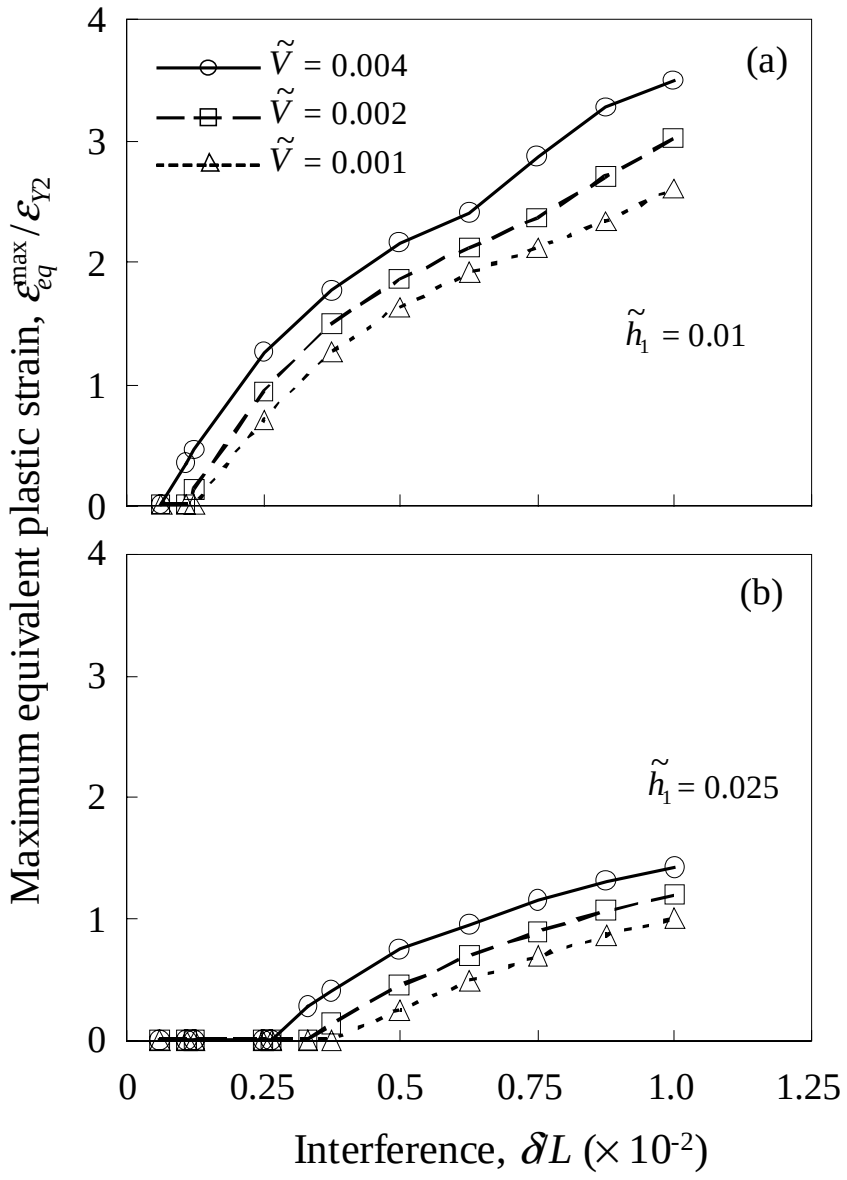

Fig. 4.11 Maximum equivalent plastic strain in the second layer of an elastic-plastic multi-layered medium indented by a rigid rough surface versus interference for indentation speed $\tilde{V}$ = 0.001, 0.002, and 0.004 and surface-layer thickness (a) $\tilde{h}_1$ = 0.01 and (b) $\tilde{h}_1$ = 0.025.

$\varepsilon_{eq}^{\max}$, in the second layer on the indentation speed and surface-layer thickness. The increase of the indentation speed promotes the initiation of yielding in the second layer and the development of larger plastic strains at a given interference. A comparison of Figs. 4.11(a) and 4.11(b) shows that the plastic flow resistance decreases with the surface-layer thickness. These tendencies are in agreement with those shown in Fig. 4.7.

Figure 4.12 shows contours of residual equivalent plastic strain, $\varepsilon_{eq,res}$, for different values of indentation speed and surface-layer thickness obtained after the first indentation cycle. Figures 4.12(a) and 4.12(b) show that, for a fixed surface-layer thickness, an increase of the indentation load/unload rate leads to the formation of more plastic zones with larger plastic strains. While the values of $\varepsilon_{eq,res}^{\max}$ at the interface below asperity contacts A and B are comparable in the low-speed indentation case (Fig. 4.12(a)), a higher $\varepsilon_{eq,res}^{\max}$ was produced below the sharper asperity B in the high-speed indentation case (Fig. 4.12(b)). This demonstrates a higher probability for excessive plastic deformation at the interface below less conforming (sharp) asperity contacts at high indentation speeds. However, Fig. 4.12(c) shows that fewer and smaller plastic zones occurred with the thicker surface layer. It is also noted that $\varepsilon_{eq,res}^{\max}$ does not occur in the plastic zone below the sharper asperity B but in the plastic zone of the relatively blunt asperity A. This is another illustration of the important role of the surface-layer thickness, indentation speed, and surface topography (roughness) on the development of subsurface plasticity in multi-layered media subjected to dynamic contact loads.

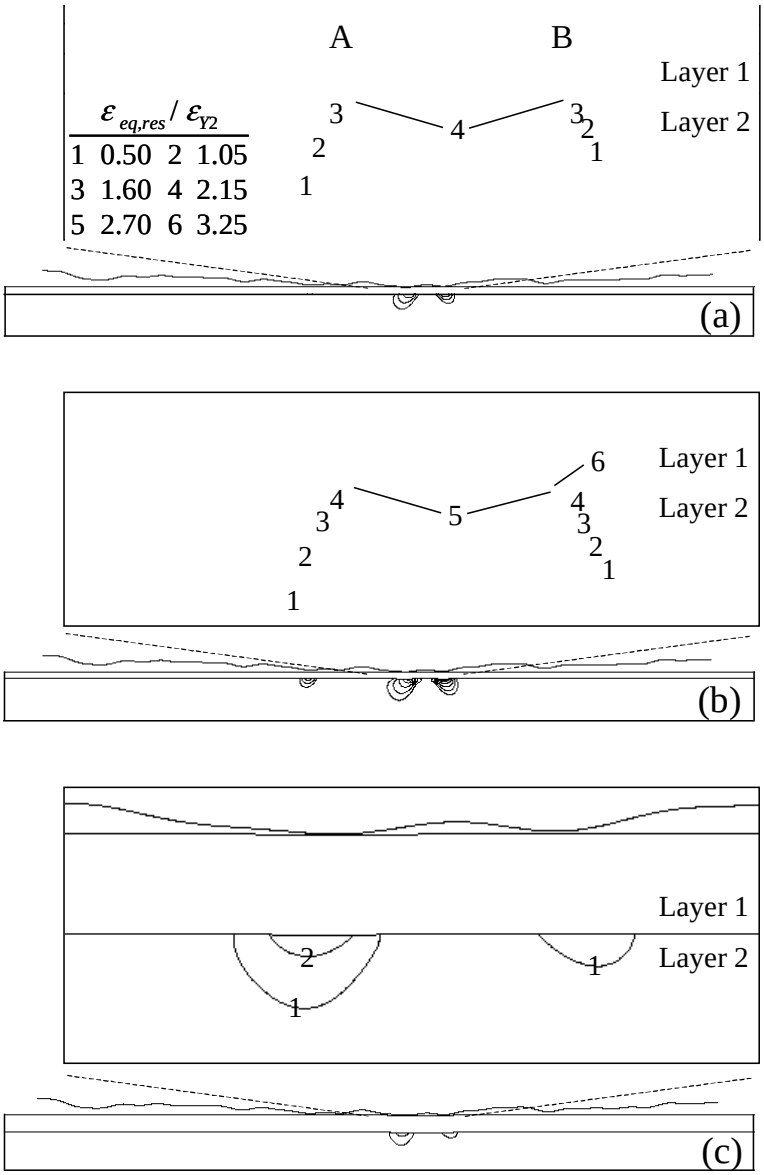

Fig. 4.12 Contours of residual equivalent plastic strain in an elastic-plastic multi-layered medium indented by a rigid, rough surface for different indentation speed and surface-layer thickness: (a) $\tilde{V}$ = 0.001, $\tilde{h}_1$ = 0.01, (b) $\tilde{V}$ = 0.004, $\tilde{h}_1$ = 0.01, and (c) $\tilde{V}$ = 0.004, $\tilde{h}_1$ = 0.025.

4.3.2 Cyclic Indentation

Although damping effects were not considered in the indentation loading and unloading simulation steps, as mentioned in section 4.2.3, after each indentation cycle, dashpot elements were added to the finite element mesh in order to obtain results for the residual stresses and strains. Due to the excessive computation time, only four indentation cycles were simulated, and the development of plasticity was examined in terms of the residual equivalent plastic strain. Representative results of $\varepsilon_{eq}^{\max}$ and $\varepsilon_{eq,res}$ in the second layer are presented below for different values of indentation speed and surface-layer thickness.

The maximum equivalent plastic strain, $\varepsilon_{eq}^{\max}$ (maximum $\tilde{\delta}$ = 0.01), and the maximum residual equivalent plastic strain, $\varepsilon_{eq,res}^{\max}$ (after full unloading from $\tilde{\delta}$ = 0.01) versus indentation cycle are shown in Figs. 4.13(a) and 4.13(b), respectively. A significant effect of both the surface-layer thickness and the indentation speed on the accumulation of plastic deformation in the second layer can be observed. In the presence of a thin surface layer ($\tilde{h}_1$ = 0.01), plastic deformation in the second layer increases linearly with the indentation cycles. However, the relatively thick surface layer ($\tilde{h}_1$ = 0.025) inhibits the cyclic accumulation of plasticity after the first indentation cycle, even in the high-speed indentation case. This implies that subsequent cyclic indentation up to the same maximum interference (i.e., $\tilde{\delta}$ = 0.01) yields a purely elastic response, indicating the occurrence of elastic shakedown. H, the results for $\tilde{h}_1$ = 0.025, $\tilde{V}$ = 0.004, and $\tilde{\delta}$ = 0.01 shown in Fig. 4.13 suggest that the single-indentation results for $\tilde{h}_1$ =

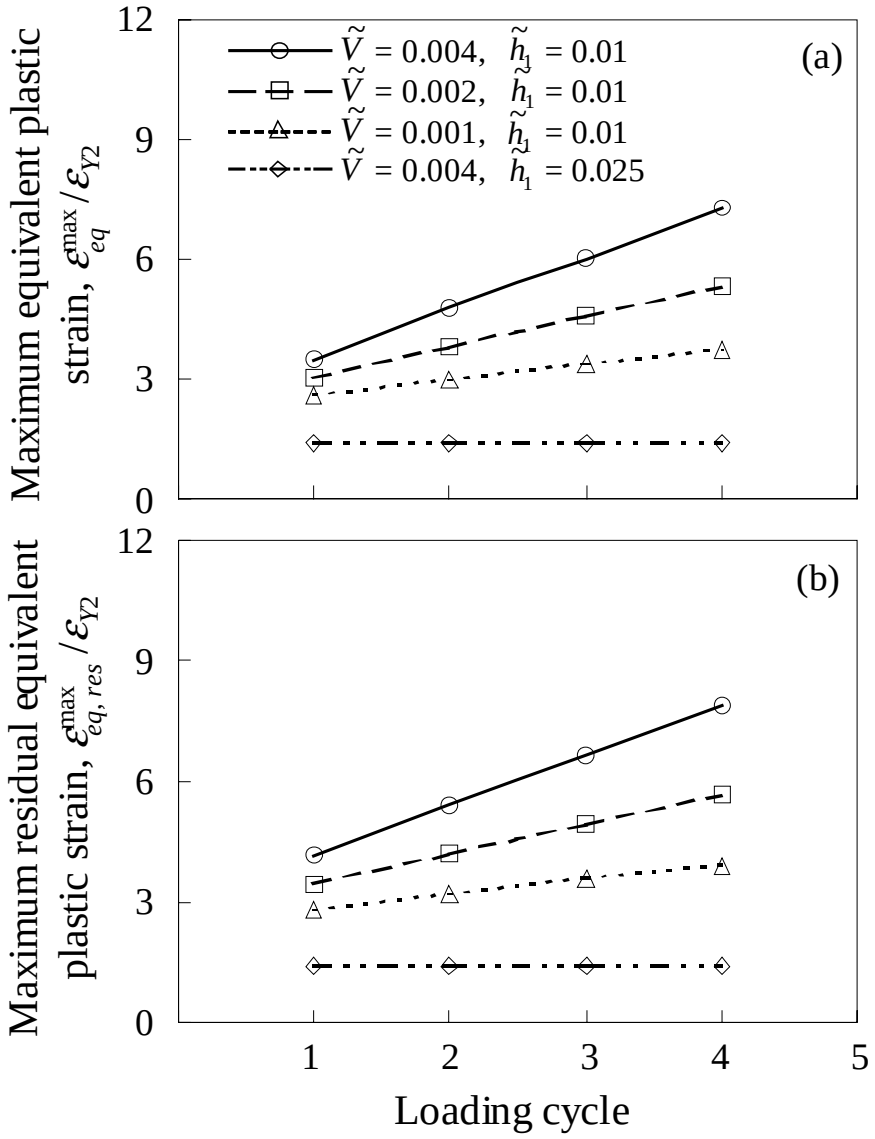

Fig. 4.13 (a) The maximum equivalent plastic strain at the maximum interference $\tilde{\delta}$ = 0.01 and (b) maximum residual equivalent plastic strain after full unloading produced in the second layer of an elastic-plastic multi-layered medium indented by a rigid, rough surface versus loading cycle for indentation speed $\tilde{V}$ = 0.001, 0.002, and 0.004 and surface-layer thickness $\tilde{h}_1$ = 0.01 and 0.025.

0.025, shown in Figs. 4.3(b), 4.4(d), 4.5(d), 4.7(b), 4.9(b), 4.11(b), and 4.12(c), are also representative of the cyclic-indentation response of this multi-layered medium for $\tilde{\delta} \leq$ 0.01. Therefore, a significant enhancement of the contact fatigue life of the multi-layered medium can be achieved in the presence of a strong and sufficiently thick surface layer that suppresses the development of high stresses at the interface due to the material property mismatch of the first and second layers. The contours of $\varepsilon_{eq,res}$ shown in Fig. 4.14 provide additional information for the spatial development of plasticity in the multi-layered medium with the thin surface layer due to cyclic indentation. It is noted that the accumulation of plastic strain is confined within a small region in the second layer close to the interface, where the maximum equivalent plastic strain always occurs. It is interesting to note the accumulation of plastic strain only below the sharper asperity B. Thus, while the region in the second layer below the blunt asperity A attains elastic shakedown after one indentation cycle, the region in the second layer below the sharper asperity B continues to accrue plastic strain. This implies that cyclic indentation may promote microcrack initiation in the compliant and soft second layer adjacent to the interface, especially below sharper asperities, eventually leading to delamination of the stiffer and stronger surface layer.

4.4 Conclusions

Dynamic indentation of an elastic-plastic multi-layered medium by a rigid, rough (fractal) surface was investigated using the finite element method. Based on the presented results for the contact force, contact pressure distribution, and subsurface stresses and strains obtained in terms of the surface-layer thickness, indentation speed, and indentation cycle, the following main conclusions can be drawn.

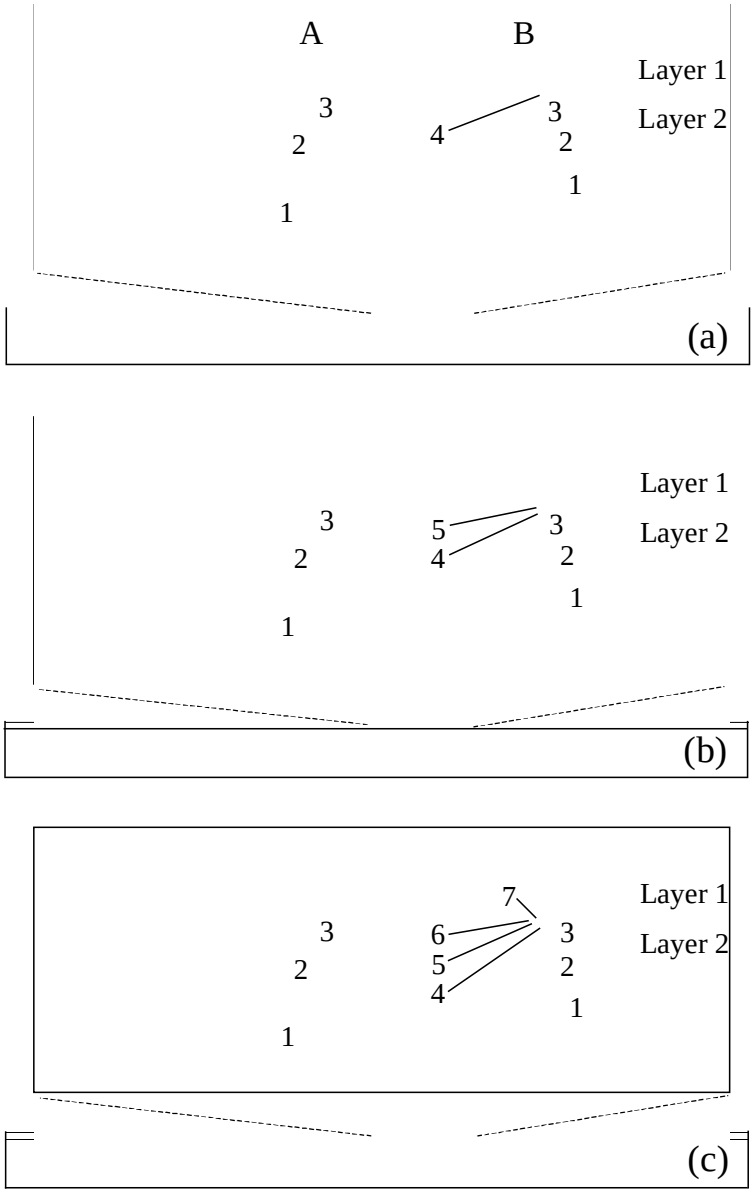

Fig. 4.14 Contours of residual equivalent plastic strain in an elastic-plastic multi-layered medium with surface-layer thickness $\tilde{h}_1$ = 0.01 indented by a rigid, rough surface for indentation speed $\tilde{V}$ = 0.004 and maximum interference $\tilde{\delta}$ = 0.01 obtained after the (a) first, (b) second, and (c) fourth loading cycle.

(1) The number of asperity contacts and the contact load, contact pressure, and subsurface stresses and plastic strains intensify with the increase of the interference and/or the indentation speed. For the material properties, surface topography (fractal parameters), and ranges of interference and indentation speed examined in this analysis, the increase of the indentation speed leads to premature yielding, more plastic zones in the soft, second layer, relatively faster increase of the maximum equivalent plastic strain below the sharper asperities, and higher tensile stresses in the elastically deformed surface layer.

(2) The critical interference at the inception of yielding in the soft, second layer increases and the intensities of the subsurface stresses and strains decrease with the increase of the thickness of the stiffer and stronger surface layer.

(3) Results for the maximum von Mises equivalent stress, first principal stress, and maximum equivalent plastic strain show that, under the simulated conditions, crack initiation and excessive plastic deformation are more likely to occur at the layer interface below the sharper and/or deeper indenting asperities.

(4) A high indentation speed and a relatively thin surface layer promote cyclic plasticity in the soft, second layer adjacent to the interface with the hard surface layer, especially below the sharper asperities. This increases the likelihood for crack initiation at the interface, where excessive plastic deformation and high tensile stress are encountered in view of the significant mismatch of the elastic and plastic properties of the two layers.

CHAPTER 5

A Mechanics Approach to Static Friction of Elastic-Plastic Fractal Surfaces

5.1 Introduction

Friction plays an important role in many fields of science and technology. The effect of friction can be either detrimental or beneficial to the performance of various engineering components and scientific instruments. However, despite numerous analytical and experimental studies, fundamental understanding of friction remains largely elusive, principally due to the lack of adequate mechanics models and unbiased description of the surface topography over a wide range of length scales. Friction depends on adhesion and deformation mechanisms encountered at asperity contacts where actual surface interaction occurs. These mechanisms are usually interdependent and their dominance is controlled by the external load, elastic-plastic material properties, surface topography, and interfacial shear strength. The large discrepancies among friction analyses in the literature are mainly due to superficial treatment of associated contact mechanics and use of scale-dependent parameters to describe the topographies of the contacting surfaces.

In early analyses, the contacting solid surfaces were assumed to be perfectly smooth. However, later studies revealed that this assumption can lead to an overestimation of the real contact area by several orders of magnitude (Webster and Sayles, 1986; Yan and Komvopoulos, 1998a) because of multi-scale roughness effects. Greenwood and Williamson (1966) developed an asperity-based model (GW model) to

study contact between nominally flat surfaces. In this model, a rough surface is represented by a large number of spherical asperities with constant radius of curvature and normal height distribution. Due to the assumption of constant asperity radius, analyses based on the original GW model predict elastic (plastic) deformation for smaller (larger) asperity contacts. In later studies, the GW model was extended to study curved surfaces (Greenwood and Tripp, 1967) and modified to include the asperity radius as a variable (Hisakado, 1974). The GW model has also been used in studies dealing with elastic-plastic contact of rough surfaces (Chang, Etsion and Bogy, 1987) and solid surface adhesion (Roy Chowdhury and Ghosh, 1994).

In view of the self-affinity property of engineering surfaces, fractal geometry (Mandelbrot, 1967) was used in contemporary contact mechanics analyses to describe the surface topography. Since the first studies dealing with surface fractal behavior (Majumdar and Tien, 1990; Majumdar and Bhushan, 1990), several contact mechanics and friction analyses have been proposed for fractal surfaces. Conversely to traditional characterization of rough surfaces by scale-dependent parameters, fractal characterization yields scale-independent parameters over a wide range of length scales where fractal behavior is observed. It has been proposed that contact of two fractal surfaces can be represented by an equivalent fractal surface in normal contact with a flat plane (Majumdar and Tien, 1991). This suggestion has been adopted in most recent contact analyses of rough surfaces. Based on a contact model of elastic-plastic fractal surfaces, Majumdar and Bhushan (1991) estimated that plastic deformation occurs at all the asperity contacts with areas less than a critical value, which is contradictory to the prediction of the original GW model. A similar model was proposed by the same authors

for elastic-plastic bi-fractal surfaces (Bhushan and Majumdar, 1992). Sahoo and Roy Chowdhury used a model of a rigid plane in contact with a deformable fractal surface to investigate normal (1996) and sliding (2000) contact of adhesive rough surfaces. Yan and Komvopoulos (1998a) performed a three-dimensional contact analysis of elastic-plastic rough surfaces characterized by a modified two-variable Weierstrass-Mandelbrot (W-M) function. Using a similar elastic-plastic fractal approach, Komvopoulos and Yan (1998) investigated adhesion in microelectromechanical systems due to van der Waals, electrostatic, and capillary forces. More recently, Komvopoulos and Ye (2001) analyzed elastic-plastic contact of layered media with fractal topographies and derived constitutive contact relationships from finite element results obtained for homogeneous and layered media.

In all the previous contact mechanics and adhesion studies, contact of two rough surfaces was modeled by an equivalent rough surface in contact with a rigid plane. Although this model greatly simplifies the interfacial geometry, its legitimacy is challenged in friction studies where the contact slope plays an important role in asperity contact deformation. The objective here is to perform a comprehensive fractal analysis of static friction based on an elastic-plastic contact mechanics model that includes both rough surfaces. Numerical results illustrate the dependence of the static coefficient of friction on normal load, interfacial shear strength, and fractal parameters.

5.2 Characterization of Rough Surfaces by Fractal Geometry

Fractal geometry was introduced by Mandelbrot (1967) to describe the self-similarity behavior of the earth's coastlines. Self-similarity and self-affinity characteristics have been observed in various fields of science and engineering, including

topographies of engineering surfaces and mechanical components (Majumdar and Tien, 1990). For three-dimensional isotropic rough surfaces, a two-dimensional profile obtained in any direction is a statistically valid representation of the surface (Majumdar and Bhushan, 1990). A two-dimensional fractal surface profile, $z(x)$, can be represented by a W-M function that satisfies the properties of continuity, non-differentiability, and self-affinity (Berry and Lewis, 1980), given by

$$z(x) = A^{(D-1)} \sum_{n=n_{\min}}^{\infty} \frac{\cos 2\pi\gamma^n x}{\gamma^{(2-D)n}}, \tag{5.1}$$

where A and D are the fractal roughness parameter and fractal dimension of the surface profile ($1 < D < 2$), respectively, γ is a parameter that determines the relative phase differences between fractal modes, and $n_{\min}$ is related to γ and the sample length, L, by $\gamma^{n_{\min}} \approx 1/L$.

For dimensional consistency, Komvopoulos and Yan (1997a) modified Eq. (5.1) to the following truncated W-M function:

$$z(x) = L\left(\frac{G}{L}\right)^{(D-1)} \sum_{n=0}^{n_{\max}} \frac{\cos(2\pi\gamma^n x/L)}{\gamma^{(2-D)n}}, \tag{5.2}$$

where G is the same as A in Eq. (5.1). Conversely to Eq. (5.1), γ is a dimensionless parameter in Eq. (5.2). Based on surface flatness (in the vicinity of $x = 0$) and frequency distribution density arguments, an appropriate value of γ equal to 1.5 was proposed in Ref. 19. Equation (5.2) shows that the surface profile is approximated by a finite number ($n_{\max} + 1$) of frequency components, where $n_{\max}$ is related to the smallest characteristic length, L_0, typically, on the order of the equilibrium atomic distance (Komvopoulos and

Yan, 1997a), by $n_{\max} \approx \ln(L/L_0)/\ln\gamma$. Accordingly, the lowest and the highest spatial frequencies of the surface profile are $\omega_l = 1/L$ and $\omega_h = \gamma^{n_{\max}}/L \approx 1/L_0$, respectively.

The power spectrum function, $\hat{P}(\omega)$, is the Fourier transformation of the autocorrelation function of $z(x)$, which is given by (Majumdar and Tien, 1990)

$$\hat{P}(\omega) = \frac{L^2}{2}\left(\frac{G}{L}\right)^{2(D-1)} \sum_{n=0}^{n_{\max}} \frac{\delta(\omega - \gamma^n/L)}{\gamma^{2(2-D)n}}, \tag{5.3}$$

or equivalently,

$$\hat{P}_c(\omega_c) = \frac{L^2}{2}\left(\frac{G}{L}\right)^{2(D-1)} \sum_{n=0}^{n_{\max}} \frac{\delta(\omega_c - 2\pi\gamma^n/L)}{\gamma^{2(2-D)n}}, \tag{5.4}$$

where ω and ω_c are spatial and circular frequencies, respectively (i.e., $\omega_c = 2\pi\omega$).

The height and the slope variances of the surface profile are obtained from the power spectrum function as following:

$$\left\langle (z)^2 \right\rangle = \int_{\omega_{cl}}^{\omega_{ch}} \hat{P}_c(\omega_c)\, d\omega_c = \frac{L^2}{2}\left(\frac{G}{L}\right)^{2(D-1)} \sum_{n=0}^{n_{\max}} \frac{1}{\gamma^{2(2-D)n}} \tag{5.5}$$

and

$$\left\langle \left(\frac{dz}{dx}\right)^2 \right\rangle = \int_{\omega_{cl}}^{\omega_{ch}} \omega_c^{\,2} \hat{P}_c(\omega_c)\, d\omega_c = 2\pi^2 \left(\frac{G}{L}\right)^{2(D-1)} \sum_{n=0}^{n_{\max}} \frac{1}{\gamma^{2(1-D)n}} \tag{5.6}$$

where ω_{cl} and ω_{ch} are the lowest and the highest circular frequencies, respectively.

The discrete power spectrum functions given by Eqs. (5.3) and (5.4) can be approximated by the continuous spectrum functions (Berry and Lewis, 1980):

$$\overline{P}(\omega) = \frac{G^{2(D-1)}}{2\ln\gamma} \frac{1}{\omega^{(5-2D)}}, \tag{5.7}$$

or

$$\overline{P}_c(\omega_c) = (2\pi)^{2(2-D)} \frac{G^{2(D-1)}}{2\ln\gamma} \frac{1}{\omega_c^{(5-2D)}} \quad . \tag{5.8}$$

Equations (5.7) and (5.8) are derived by averaging $\hat{P}(\omega)$ and $\hat{P}_c(\omega_c)$ over a frequency range $\Delta\omega$ and $\Delta\omega_c$, respectively (Berry and Lewis, 1980). Therefore, the height and the slope variances are expressed as:

$$\left\langle (z)^2 \right\rangle \approx \int_{\omega_{cl}}^{\omega_{ch}} \overline{P}_c(\omega_c) d\omega_c = \frac{1}{4\ln\gamma} \frac{G^{2(D-1)}}{(2-D)} \left[\frac{1}{\omega_l^{2(2-D)}} - \frac{1}{\omega_h^{2(2-D)}} \right] \tag{5.9}$$

and

$$\left\langle \left(\frac{dz}{dx} \right)^2 \right\rangle \approx \int_{\omega_{cl}}^{\omega_{ch}} \omega_c^{\,2} \overline{P}_c(\omega_c) d\omega_c = (2\pi)^2 \frac{1}{4\ln\gamma} \frac{G^{2(D-1)}}{(D-1)} \left[\omega_h^{\,2(D-1)} - \omega_l^{\,2(D-1)} \right] . \tag{5.10}$$

It is noted that Eq. (5.10) differs from that given by Majumdar and Tien (1990) and Majumdar and Bhushan (1990) by a factor of $(2\pi)^2$ because of an error in their integration involving the use of the spatial frequency instead of the circular frequency. The correct derivation of Eq. (5.10) is given in Appendix A (Eq. (A8)).

5.3 Contact Mechanics and Friction Analysis

In all previous contact mechanics studies of fractal surfaces, one of the contacting surfaces is assumed to be flat and, thus, all the asperity contacts are perpendicular to the global normal direction (i.e., zero-slope contacts). However, contact of real surfaces produces asperity contacts that, in general, are not perpendicular to the global normal direction. Because the contact slope plays an important role in friction and affects the real contact area, it is necessary to include the contact slope distribution in the friction analysis of rough surfaces. A theoretical analysis of static friction, in which both rough surfaces are characterized by fractal geometry, is developed in this section. In general, the

two surfaces possess different fractal parameters D and G. Without loss of generality, it is assumed that $D_1 < D_2$, where subscripts 1 and 2 are used to distinguish the surfaces, and the system consisting of two surfaces with the same D parameter ($D_1 = D_2$) is treated as a special case.

5.3.1 Contact size distribution.

The contact (normal) load and friction force acting between asperities depend strongly on the contact size. Predicting the size distribution is fundamental in contact mechanics. Mandelbrot (1975, 1983) proposed that the cumulative size distribution of the earth's islands follows a power-law relationship. This relationship has been used in several contact analyses of fractal surfaces (Yan and Komvopoulos, 1998a; Majumdar and Bhushan, 1990 and 1991; Majumdar and Tien, 1991; Sahoo and Roy Chowdhury, 1996 and 2000; Komvopoulos and Yan, 1997a and 1998; Komvopoulos and Ye, 2001) in the form:

$$N(a') = \left(\frac{a'_L}{a'}\right)^{D/2}, \tag{5.11}$$

where $N(a')$ is the number of truncated contacts with areas larger than a', and a'_L is the largest truncated contact area. The size distribution of the truncated contacts is given by

$$n(a') = -\frac{dN(a')}{da'} = \frac{D}{2a'_L}\left(\frac{a'_L}{a'}\right)^{(D+2)/2}. \tag{5.12}$$

Bhushan and Majumdar (1992) extended this power-law relationship to bi-fractal surfaces. A similar approach is used in the present analysis to derive the size distribution of the projected areas (on the zero z plane of each surface) of the truncated asperity contacts.

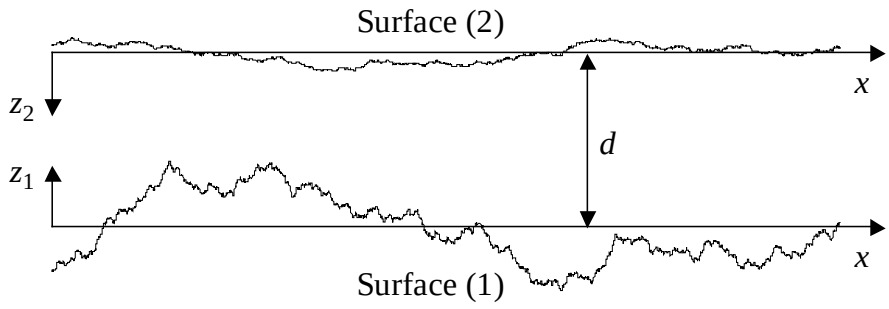

Fig. 5.1 Schematic showing the separation distance, *d*, between two rough surfaces, 1 and 2.

For nominal surface separation equal to *d* (Fig. 5.1), the real separation between two surface profiles $z_1(x)$ and $z_2(x)$ is

$$z(x) = d - z_1(x) - z_2(x). \tag{5.13}$$

Since the two surfaces are statistically uncorrelated, the structure function of the surface separation is given by (Majumdar and Tien, 1991)

$$S(\lambda) = \left\langle (z(x+\lambda) - z(x))^2 \right\rangle = \left\langle (z_1(x+\lambda) - z_1(x))^2 \right\rangle + \left\langle (z_2(x+\lambda) - z_2(x))^2 \right\rangle = S_1(\lambda) + S_2(\lambda), \tag{5.14}$$

where λ is the correlation length, and its approximate continuous power spectrum satisfies the relationship:

$$\overline{P}(\omega) = \overline{P}_1(\omega) + \overline{P}_2(\omega). \tag{5.15}$$

Figure 5.2 shows schematically the approximate continuous power spectra of two surface profiles intersecting at a critical frequency ω^*. For $\omega < \omega^*$, $\overline{P}(\omega) \approx \overline{P}_1(\omega)$ because $\overline{P}_1(\omega) > \overline{P}_2(\omega)$, while for $\omega > \omega^*$, $\overline{P}(\omega) \approx \overline{P}_2(\omega)$ because $\overline{P}_1(\omega) < \overline{P}_2(\omega)$. Therefore, the equivalent topography of the two-surface system can be characterized by a

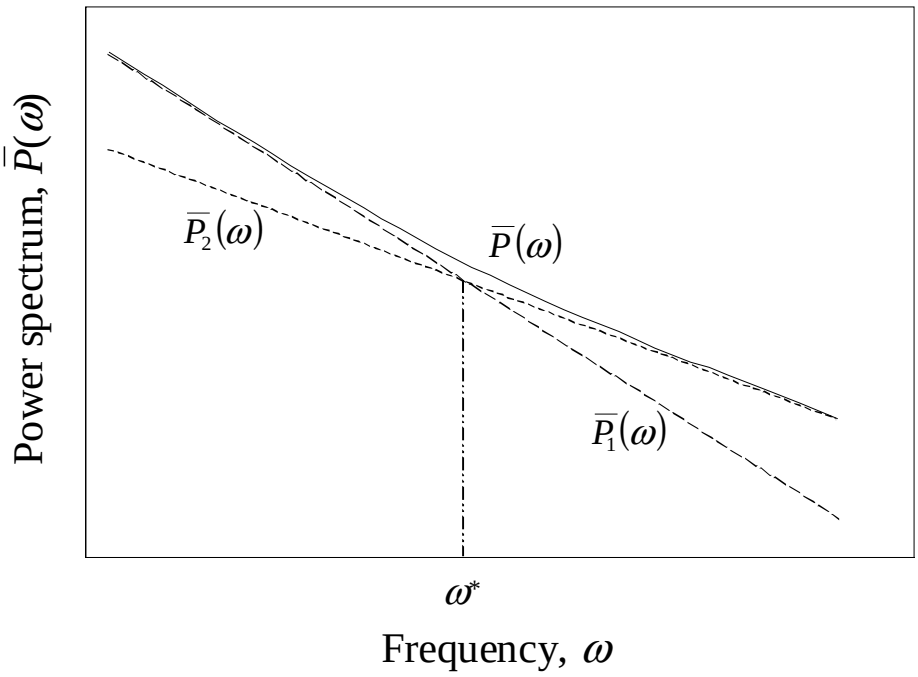

Fig. 5.2 Schematic log-log plot of approximate continuous power spectra of two fractal surfaces $\overline{P}_1(\omega)$ and $\overline{P}_2(\omega)$ with different fractal dimension ($D_1 < D_2$) intersecting at a critical frequency ω^*, and power spectrum of the equivalent surface $\overline{P}(\omega)$.

single set of fractal parameters in each regime, i.e., D_1 and G_1 ($\omega < \omega^*$) and D_2 and G_2 ($\omega > \omega^*$). Since the spatial frequency and the base wavelength of a truncated contact, $2r_p'$, where r_p' is the effective radius of the projected area of the truncated contact, are related by $\omega = 1/(2r_p')$, the spatial frequency is a function of the projected area of the truncated contact ($a_p' = \pi r_p'^2$) (Fig. 5.3), i.e.,

$$\omega(a_p') = \left(\frac{\pi}{4a_p'} \right)^{1/2} . \tag{5.16}$$

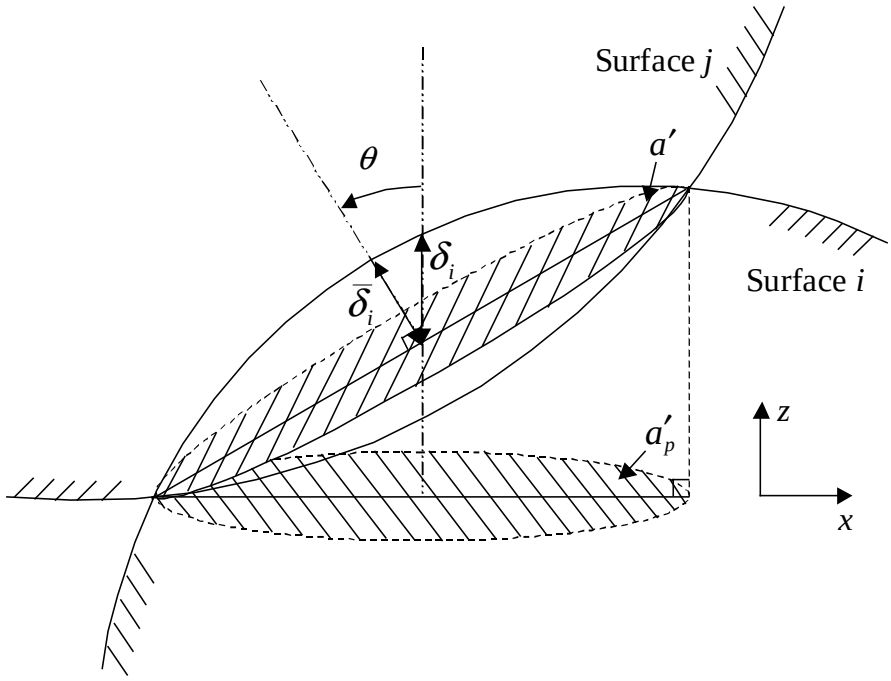

Fig. 5.3 Schematic illustration of the truncation of two asperities on surfaces *i* and *j* with contact angle θ.

In view of Eqs. (5.12) and (5.16) and Fig. 5.2, the size distribution of the projected areas of the truncated contacts can be approximated by

$$n(a'_p) \propto \left(a'_p\right)^{-(D_1+2)/2},\ \omega(a'_p) < \omega^* \tag{5.17a}$$

and

$$n(a'_p) \propto \left(a'_p\right)^{-(D_2+2)/2},\ \omega(a'_p) > \omega^*. \tag{5.17b}$$

If the largest projected area of the truncated contacts, a'_{pL}, is known, then if $\omega(a'_{pL}) > \omega^*$,

$$n(a'_p) = \frac{D_2}{2a'_{pL}}\left(\frac{a'_{pL}}{a'_p}\right)^{(D_2+2)/2}, \tag{5.18}$$

while if $\omega(a'_{pL}) < \omega^*$,

$$n(a'_p) = \frac{D_1}{2a'_{pL}}\left(\frac{a'_{pL}}{a'_p}\right)^{(D_1+2)/2}, \qquad \omega(a'_p) < \omega^* \tag{5.19a}$$

and

$$n(a'_p) = \frac{D_1}{2a'_{pL}}\left(\frac{a'_{pL}}{a'_{p*}}\right)^{(D_1+2)/2}\left(\frac{a'_{p*}}{a'_p}\right)^{(D_2+2)/2}, \qquad \omega(a'_p) > \omega^*, \tag{5.19b}$$

where a'_{p*} is the critical projected area of truncated contact corresponding to the critical frequency $\omega^* = \left[\pi/\left(4a'_{p*}\right)\right]^{1/2}$.

The total projected area of truncated contacts, A'_P, is a function of the largest and the smallest projected areas of truncated contacts, a'_{pL} and a'_{pS} ($a'_{pS} = \pi L_0^{\,2}/4$), and can be obtained from the piece-wise power-law size distribution (Eqs. (5.18) and (5.19)) by integration (Komvopoulos and Ye, 2001):

$$A'_P = \int_{a'_{pS}}^{a'_{pL}} n(a'_p)\, a'_p\, da'_p .$$

Using the previous integral relationship and the bisection method, a'_{pL} was determined in terms of A'_P, D_i (i=1, 2), a'_{pS}, and a'_{p*}.

For the special case of $D_1 = D_2$, the system of the two contacting surfaces can be characterized by only one fractal dimension, and the island rule proposed by Mandelbrot (1975, 1983) can be used directly. For this case, Eqs. (5.19a) and (5.19b) are identical.

5.3.2 Contact slope distribution.

The contact angle, θ ($0 \le \theta < \pi/2$), of a truncated plane is the angle between the

global z direction and the normal to the contact plane (Fig. 5.3). For static friction analysis, if the contact opposes the onset of relative movement, the contact slope is defined as $s = \tan\theta$ (positive slope), while if the contacting asperities tend to separate, $s = -\tan\theta$ (negative slope). For three-dimensional isotropic surfaces, the contact slope distribution can be obtained from the secant slope distribution of the truncation line-segments (Fig. 5.4(a)) of a two-dimensional surface profile with associated fractal parameters. The probability density function, $p(s)$, of the secant slope of line-segments with the same projected length, l ($l << L$), can be determined from numerical simulation. Figure 5.4(b) shows a comparison between the probability density function obtained from a simulation and three normal distributions with standard deviations equal to the root-mean-square (rms) of the secant slope of the simulation data, σ_{sim}, and the square root of the values estimated from Eqs. (5.6) and (5.10). In the calculation of the slope variance using Eqs. (5.6) and (5.10), the highest frequency, ω_h, was replaced by $1/(2l)$. The close agreement between the distributions shown in Fig. 5.4(b) indicates that the secant slope of line-segments with the same projected length follows a normal distribution and that the slope variance can be estimated from Eqs. (5.6) or (5.10) by replacing ω_h with $1/(2l)$. This is due to the fact that the tangent slope is a good approximation of the secant slope for low frequency components ($\omega \le 1/(2l)$) and the contribution of high frequency components ($\omega > 1/(2l)$) to the secant slope is negligible. Obviously, the expectation of the secant slope is close to zero because the rough surface is a flat plane at the macroscale. Thus, the distribution of the secant slope for a given projected length can be expressed as:

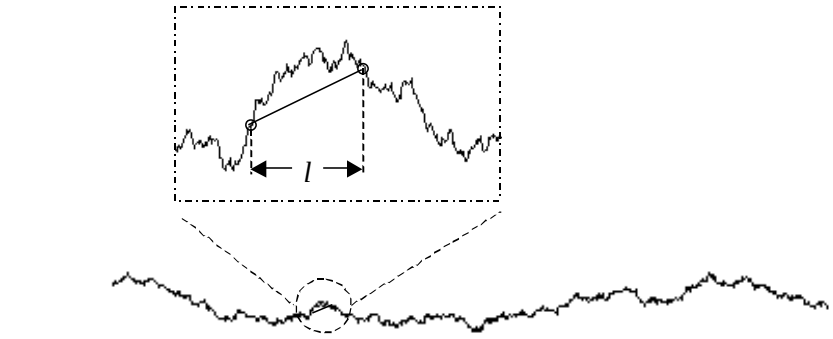

(a)

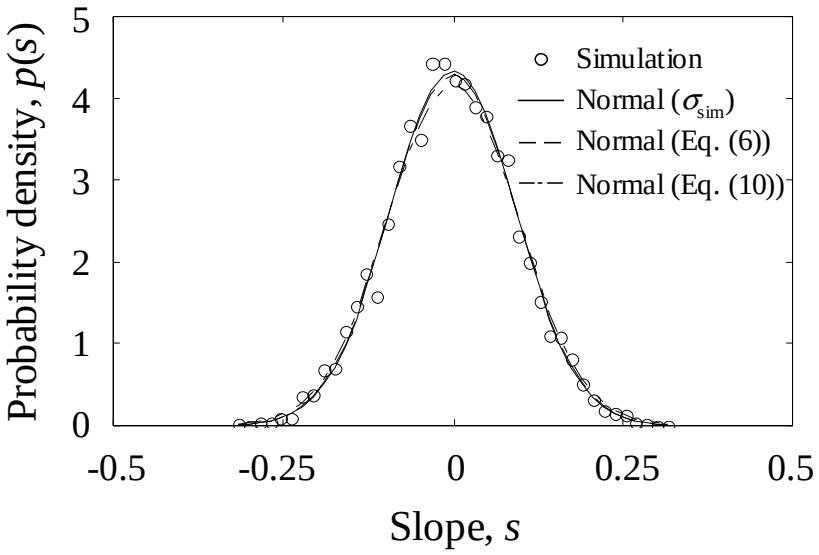

(b)

Fig. 5.4 (a) Schematic showing a line-segment of projected length l, and (b) probability density function of the secant slope of line-segments with l = 10 nm (obtained from a two-dimensional fractal surface profile with L = 4379 nm, L_0 = 2 nm, D = 1.44, and G = 9.46×10^{-4} nm) and normal distributions with standard deviations equal to the rms of the secant slope of the simulation data, σ_{sim}, and the square root of the values estimated from Eqs. (5.6) and (5.10).

$$p_i(s) = \frac{1}{\sqrt{2\pi}\sigma_i} e^{-(s^2/2\sigma_i^2)} \qquad (i = 1, 2), \tag{5.20}$$

where σ_i is obtained from Eq. (5.10), and for $l = 2r_p'$, it is given by

$$\sigma_i^2 \approx \frac{\pi^2}{\ln\gamma}\frac{G_i^{2(D_i-1)}}{(D_i-1)}\left[\left(\frac{1}{2l}\right)^{2(D_i-1)} - \left(\frac{1}{L}\right)^{2(D_i-1)}\right] = \frac{\pi^2}{\ln\gamma}\frac{G_i^{2(D_i-1)}}{(D_i-1)}\left[\left(\frac{\pi}{16a_p'}\right)^{(D_i-1)} - \left(\frac{1}{L}\right)^{2(D_i-1)}\right]$$

(i=1, 2). (5.21)

Assuming that the slope distribution, $p_{12}(s)$, of the truncated contacts with base wavelength equal to $2r_p'$ is proportional to the secant slope distribution of each surface profile, $p_i(s)$ (i =1, 2), obtained for $l = 2r_p'$,

$$p_{12}(s) \propto p_1(s)p_2(s), \tag{5.22}$$

it can be shown that

$$p_{12}(s) = \frac{1}{\sqrt{2\pi}\sigma_{12}} e^{-(s^2/2\sigma_{12}^2)}, \tag{5.23}$$

where

$$\frac{1}{\sigma_{12}^2} = \frac{1}{\sigma_1^2} + \frac{1}{\sigma_2^2}. \tag{5.24}$$

5.3.3 Mechanics and friction models of a single asperity contact.

Consider a truncated contact with projected area a_p' (Fig. 5.3). The truncated contact area, a', is related to a_p' by $a' = a_p'/\cos\theta$. The roughness amplitude, δ_i (i = 1, 2), is a function of the base wavelength $2r_p'$ and, hence, a_p' (Majumdar and Bhushan, 1991):

$$\delta_i = G_i^{(D_i-1)}(2r_p')^{(2-D_i)} = G_i^{(D_i-1)}\left(\frac{4a'_p}{\pi}\right)^{(2-D_i)/2}. \quad (5.25)$$

In view of Fig. 5.3, the local interference is given by $\bar{\delta}_i \approx \delta_i \cos\theta$. For spherical asperities, the effective radius of the truncated contact is $r' = (a'_p/\pi\cos\theta)^{1/2}$, and the radius of curvature of the contacting asperity on surface *i*, R_i, can be written as:

$$R_i^{\ 2} = \left(R_i - \bar{\delta}_i\right)^2 + r'^2 \approx \left(R_i - \delta_i\cos\theta\right)^2 + \frac{a'_p}{\pi\cos\theta}. \quad (5.26)$$

If $\delta_i << R_i$, Eqs. (5.25) and (5.26) yield

$$R_i = \frac{\left(a'_p\right)^{D_i/2}}{2^{(3-D_i)}\pi^{D_i/2}G_i^{(D_i-1)}\cos^2\theta}. \quad (5.27)$$

According to the Hertz theory, the local normal force, F_n^l, of an elastic spherical contact is given by

$$F_n^l = \frac{4E'}{3R}\left(\frac{a}{\pi}\right)^{3/2} = \frac{4E'}{3R}\left(\frac{a'_p}{2\pi\cos\theta}\right)^{3/2}, \quad \frac{1}{E'} = \frac{1-\nu_1^2}{E_1} + \frac{1-\nu_2^2}{E_2}, \quad \frac{1}{R} = \frac{1}{R_1} + \frac{1}{R_2}, \quad (5.28)$$

where a is the real contact area $(a = a'/2)$, and E' and R are the equivalent elastic modulus and radius of curvature, which are functions of the elastic modulus, E_i, Poisson ratio, ν_i, and radius of curvature, R_i, of the asperities (i = 1, 2).

The asperity contacts are assumed to deform either elastically or fully plastically. To maintain a continuous mean contact pressure, p_m, the criterion for the inception of fully plastic deformation is expressed as

$$p_m = \frac{F_n^l}{a} = \frac{(2\cos\theta)^{3/2}}{3}\left[\frac{2^{(3-D_1)}\pi^{(D_1-3)/2}G_1^{(D_1-1)}}{\left(a'_p\right)^{(D_1-1)/2}} + \frac{2^{(3-D_2)}\pi^{(D_2-3)/2}G_2^{(D_2-1)}}{\left(a'_p\right)^{(D_2-1)/2}}\right]E' = H_s, \quad (5.29)$$

where $H_s = \min(H_1, H_2)$ denotes the hardness of the softer surface. Equation (5.29) is applicable when $\min(H_1, H_2) << \max(H_1, H_2)$, i.e., the softer surface deforms plastically, and in the special case of similar surfaces, i.e., $H_1 \approx H_2$. This criterion leads to the following distinction of elastic and fully plastic contacts:

$$p_m = \frac{F_n^l}{a} < H_s \qquad \text{(elastic contact)} \tag{5.30a}$$

and

$$p_m = H_s \qquad \text{(fully plastic contact).} \tag{5.30b}$$

For fixed θ, Eq. (5.29) indicates that a smaller a_p' (or a') yields a higher mean contact pressure. This implies that asperity contacts with a smaller a_p' (or a') are more likely to deform plastically. The local normal force for a fully plastic contact is given by

$$F_n^l = H_s a, \tag{5.31}$$

and the corresponding real contact area can be approximated by the truncated contact area because for fully plastic contact, $a \approx a'$ (Yan and Komvopoulos, 1998a).

It is noted that in the present model the direction of the local normal (contact) load may not be coincident with the global normal direction due to a non-zero contact slope. However, for perfectly normal contact, the total lateral force is close to zero because the slope effect is insignificant due to the randomness of the slope distribution.

By definition, the static friction force is equal to the lateral force at the inception of sliding. Since the normal load and displacement at each asperity contact are affected by the lateral force, some assumptions are necessary in order to obtain closed-form solutions for the normal and friction forces between two contacting asperities at the

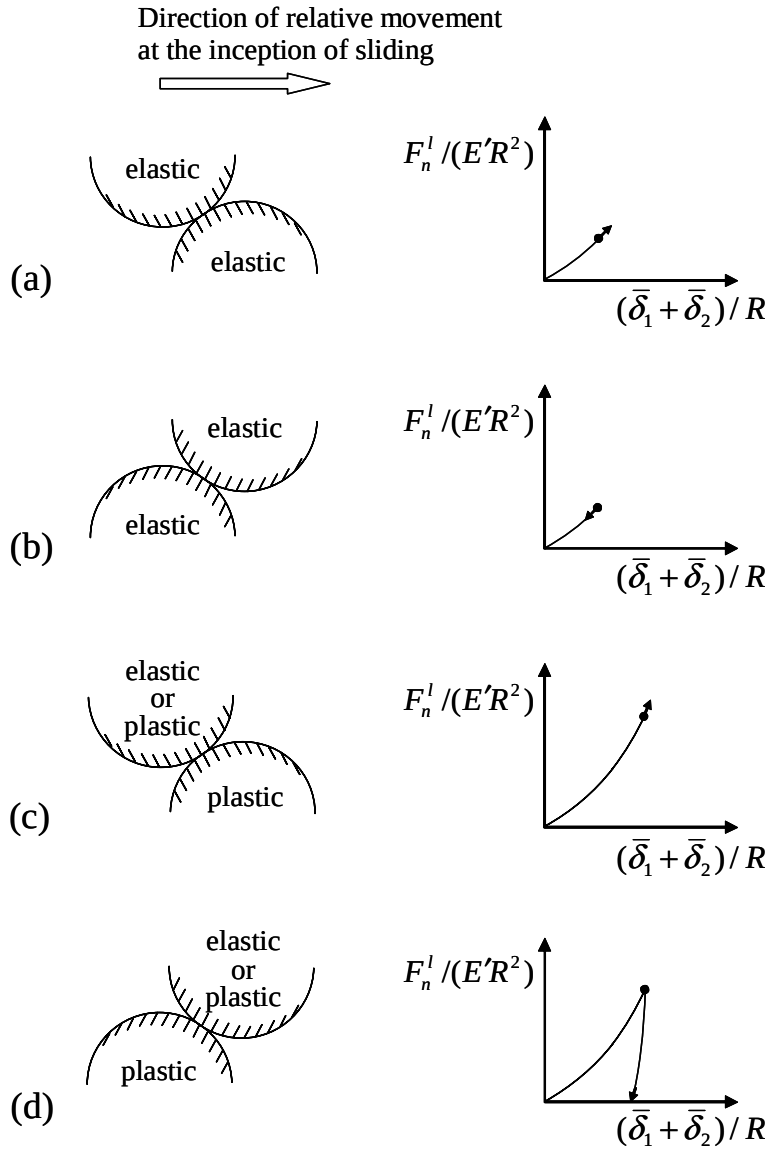

Fig. 5.5 Schematics of asperity contacts and associated normal load versus interference response: (a) both asperities deform elastically and the contact opposes the onset of relative movement, (b) both asperities deform elastically and tend to separate at the inception of sliding, (c) at least one asperity deforms plastically and the contact opposes the onset of relative movement, and (d) at least one asperity deforms plastically and the asperities tend to separate at the inception of sliding.

inception of sliding. In the present analysis, the asperity contacts are divided into four categories, as shown schematically in Fig. 5.5: (a) both asperities deform elastically and the contact opposes the onset of relative movement, (b) both asperities deform elastically and tend to separate at the inception of sliding, (c) at least one asperity deforms plastically and the contact opposes the onset of relative movement, and (d) at least one asperity deforms plastically and the asperities tend to separate at the inception of sliding. Depending on the type of contact, the normal force F_n^l may increase (cases (a) and (c)) or decrease (cases (b) and (d)) due to lateral deformation. If the normal load and the friction force vary independently, the normal force versus interference response for pure normal contact loading and unloading can be used to characterize the change in the normal force. For cases (a)–(c), a small change in the interference produces a small change in the normal force, while for case (d) even a small change in the interference produces a significant decrease in the normal force, as shown in the corresponding force-displacement schematics in Fig. 5.5. It is possible for the normal force to decrease to zero, in which case the asperities separate. Therefore, a reasonable simplification for the estimation of the normal force is to assume that in cases (a)-(c) the normal force can be approximated by that obtained for pure normal contact at the same interference, whereas in case (d) the normal force is assumed to be zero due to the separation of the asperities.

The friction force at a contact depends on the interfacial shear strength, τ, and real contact area, a. Experiments have shown that the static friction force in dry contacts is proportional to the real contact area and independent of the normal load (Johnson, 1997). This suggests that the interfacial shear strength is constant and indicative of the affinity of the contacting surfaces for each other. Constant shear strength is also a

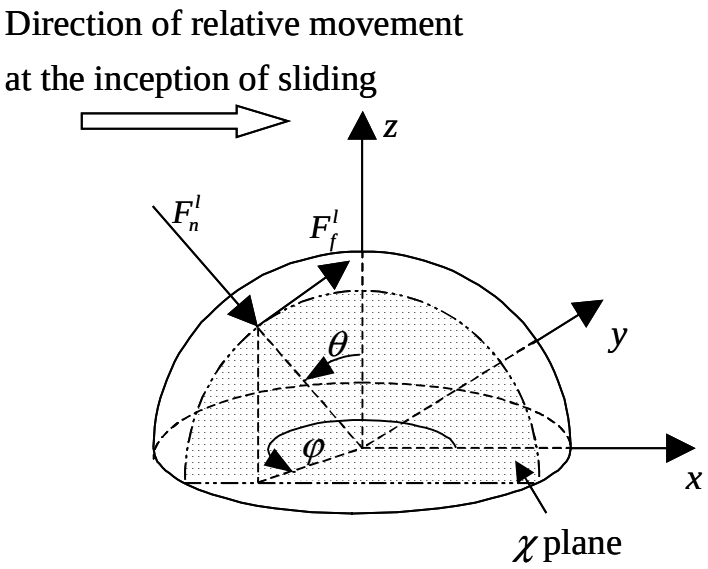

Fig. 5.6 Schematic showing the local forces acting on a single spherical asperity. The local normal force F_n^l passes through the sphere center, while the local friction force F_f^l is tangent to the circle on χ plane, which is parallel to the direction of the relative movement at the inception of sliding.

reasonable assumption for boundary-lubricated surfaces (Komvopoulos, 1991), in the absence of significant contact pressure and/or flash temperature changes. Thus, the local friction force at a contact, F_f^l, can be expressed as:

$$F_f^l = a\tau. \tag{5.32}$$

Figure 5.6 shows the normal and friction forces acting between two contacting spherical asperities with a random spatial engagement. (Only one asperity is shown for clarity.) The normal force passes through the centers of the spherical asperities, while the friction force is tangent to the circle on χ plane, which is parallel to the direction of relative movement at the inception of sliding. Both forces depend on angles θ (colatitude angle) and φ (azimuthal angle), where φ varies in the range of $(-\pi/2, 3\pi/2]$. For cases (a)

and (c), $\pi/2 \le \varphi \le 3\pi/2$ (positive contact slope), while for cases (b) and (d), $-\pi/2 < \varphi < \pi/2$ (negative contact slope). Transformation of the local normal and friction forces to the global coordinate system yields the following relationships for the global normal and friction forces, F_n^g and F_f^g, respectively, at a single asperity contact:

$$F_n^g = F_n^l \cos\theta + F_f^l \left[1 - \frac{\cos^2\theta}{1-\sin^2\theta\sin^2\varphi}\right]^{1/2} \operatorname{sgn}(\cos\varphi) \tag{5.33a}$$

and

$$F_f^g = -F_n^l \sin\theta\cos\varphi + F_f^l \frac{\cos\theta}{\left[1-\sin^2\theta\sin^2\varphi\right]^{1/2}}. \tag{5.33b}$$

Equations (5.33a) and (5.33b) are applicable to asperity contact cases (a)-(c), while for asperity contact case (d) both forces are equal to zero because the asperities are assumed to separate at the inception of sliding.

5.3.4 Total normal and friction forces.

For lightly loaded interfaces, such as those of hard disk drives and microelectromechanical systems, the real contact area is a small fraction of the apparent contact area (e.g., less than 1-2 percent), and interaction between neighboring contacts can be neglected as insignificantly small. Therefore, based on the size and slope distributions of the asperity contacts and the contact mechanics relationships and friction model presented in the previous sections, the total normal and friction forces in the global coordinate system, F_n^{tot} and F_f^{tot}, respectively, can be determined from the following integral relationships:

$$F_n^{tot} = \int_{a'_{pS}}^{a'_{pL}} \left[\int_0^{+\infty} \left(\frac{1}{2\pi} \int_{-\pi/2}^{3\pi/2} F_n^g \, d\varphi \right) 2 p_{12}(s) \, ds \right] n(a'_p) \, da'_p \tag{5.34a}$$

and

$$F_f^{tot} = \int_{a'_{pS}}^{a'_{pL}} \left[\int_0^{+\infty} \left(\frac{1}{2\pi} \int_{-\pi/2}^{3\pi/2} F_f^g \, d\varphi \right) 2 p_{12}(s) ds \right] n(a'_p) da'_p. \tag{5.34b}$$

Both forces are averaged in all possible azimuthal directions (angle φ), assuming a uniform distribution of φ. This implies that the total forces are obtained by averaging the local forces in all possible sliding directions.

Numerical integration of Eqs. (5.34a) and (5.34b) yields the total normal and friction forces, which are used to obtain the static coefficient of friction, *f*, defined as

$$f = \frac{F_f^{tot}}{F_n^{tot}}. \tag{5.35}$$

5.4 Results and Discussion

A mechanics approach for analyzing static friction of fractal surfaces was presented in the previous sections. Because it is not possible to derive closed-form solutions for the total normal and friction forces (Eqs. (5.34a) and (5.34(b)), results for the static coefficient of friction in terms of normal load, interfacial shear strength, and fractal parameters were obtained by numerical integration. The results presented below are for three-dimensional isotropic copper surfaces with E = 129.8 GPa, ν = 0.343 (Kaye, 1986), and H = 900 MPa (= $3S_y$, where S_y is the yield strength). For isotropic surfaces, the fractal dimension of the three-dimensional topography, D_s, is related to that of any two-dimensional surface profile, D, through $D_s = D + 1$ (Majumdar and Bhushan, 1990). Hence, for consistency, in the numerical results presented below the fractal parameter values were converted to their corresponding D_s values. Unless otherwise stated, the results were obtained for τ/k = 0.8, where k is the yield strength in shear ($k = S_y/\sqrt{3}$).

5.4.1 Dependence of Static Coefficient of Friction on Normal Load.

Before proceeding with the presentation of the results showing the effect of the normal load on the static coefficient of friction, it is instructive to consider the effects of surface roughness and normal load on the deformation of the asperity contacts. A characteristic of fractal surfaces is that small and large asperity contacts undergo plastic and elastic deformation, respectively (asperity radius effect). In the case of lightly loaded interfaces, contact occurs at the tips of the asperities, where the local curvature is controlled by the smaller wavelengths of the surface profile. Consequently, the majority of the asperity contacts deform plastically. When plastic deformation dominates, $F_f^l / F_n^l = \tau / H_s$ (Eqs. (5.31) and (5.32)), which is constant for given material properties and interfacial condition. However, because the variance of the contact slope decreases with the increase of the projected area of truncated contact, a_p' (Eq. (5.21)) and both the largest and the average projected areas of truncated contacts increase with normal load, the surface roughness effect becomes less significant with the increase of the normal load. Thus, the static coefficient of friction decreases as the normal load increases in the low-load range, where plastic deformation is the dominant mode. At high normal loads, deformation is controlled by the larger wavelengths of the surface profile, and the dominant larger asperity contacts undergo elastic deformation. In this case, the static coefficient of friction increases with the normal load. This can be attributed to the rapid increase of $F_f^l / F_n^l = \tau / p_m$ (Eqs. (5.29) and (5.32)) due to the inverse dependence of p_m on a_p' (Eq. (5.29)), while the surface roughness effect becomes less significant, as

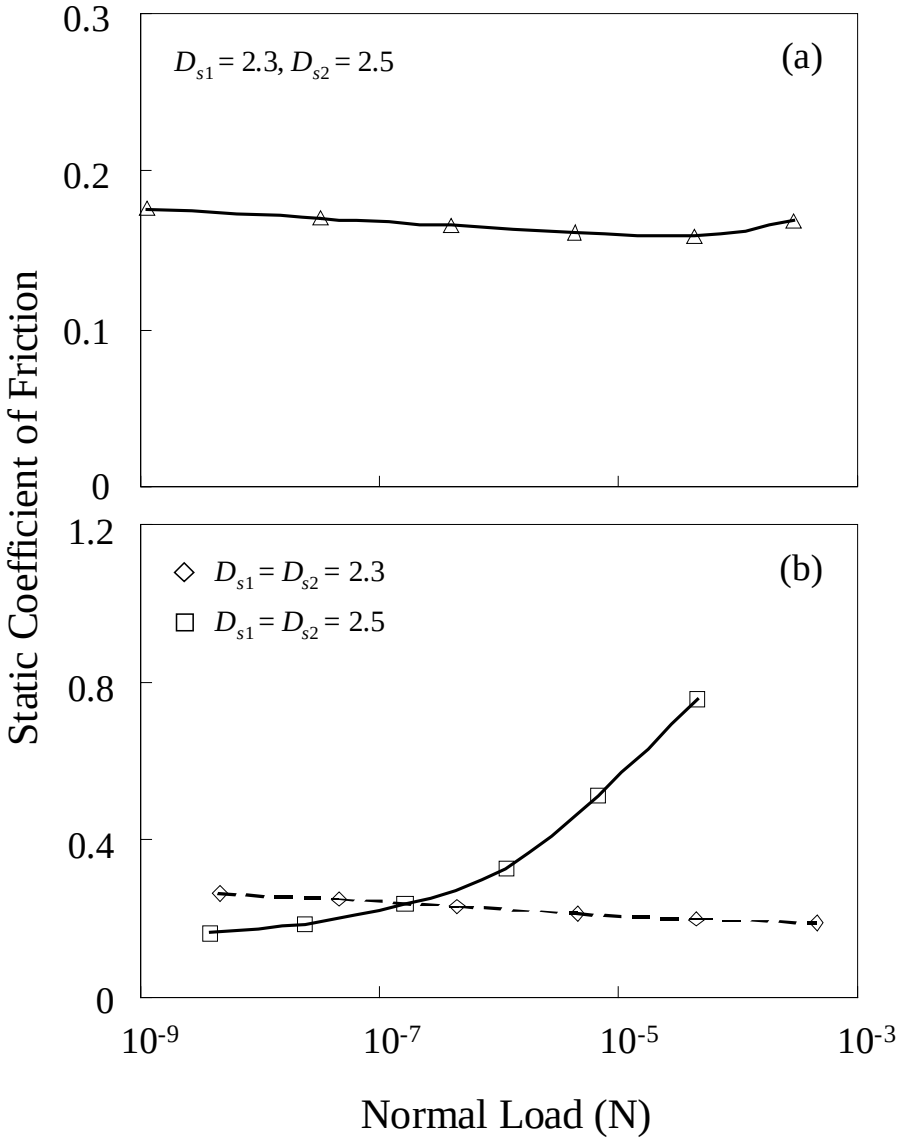

Fig. 5.7 Static coefficient of friction versus normal load for (a) D_{s1} = 2.3 and D_{s2} = 2.5, and (b) D_{s1} = D_{s2} = 2.3 and 2.5 (L = 10 μm, L_0 = 2 nm, $G_1 = 2.109 \times 10^{-5}$ nm, $G_2 = 1.055 \times 10^{-4}$ nm, E = 129.8 GPa, S_y = 300 MPa, ν = 0.343, H = 900 MPa, and τ/k = 0.8.)

explained earlier for the low-load range.

Figure 5.7 shows the dependence of the static coefficient of friction on the normal load for different values of fractal dimension D_s. Figure 5.7(a) shows that the increase of

the normal load produces a gradual decrease of the static coefficient of friction up to a critical load, followed by a gradual increase at higher loads. This trend can be explained by considering the previous discussion about the normal load dependence of the dominant deformation mode at the asperity contacts. Hereafter, the critical load corresponding to the minimum static coefficient of friction will be referred to as the transition load. In view of the dependence of the coefficient of friction on the dominant deformation mode, the friction curves shown in Fig. 5.7(b) indicate that, for the simulated normal load range, plastic and elastic deformation prevailed at the asperity contacts for $D_{s1} = D_{s2} = 2.3$ and 2.5, respectively. These results illustrate that, depending on the topographies of the contacting surfaces, a transition load may not exist within the normal load range examined.

5.4.2 Dependence of Static Coefficient of Friction on Interfacial Shear Strength.

Figure 5.8 shows the effect of the interfacial shear strength on the static coefficient of friction. The cases of $\tau/k = 0.2$ and 0.8 are representative of boundary-lubricated and unlubricated interfaces. As expected, higher interfacial shear strength resulted in higher static coefficient of friction. For the simulated parameters, when plastic deformation at the asperity contacts dominates (low-load range), the static coefficient of friction decreases gradually with the increase of the normal load at a rate independent of the τ/k value. However, when elastic deformation dominates (high-load range), the rate at which the static coefficient of friction increases with the normal load is affected by the interfacial shear strength.

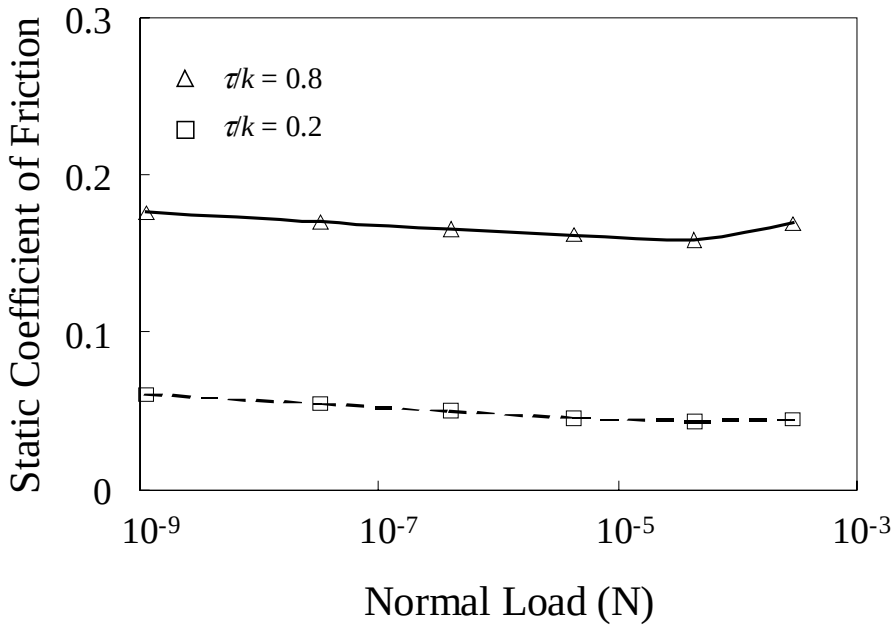

Fig. 5.8 Static coefficient of friction versus normal load for τ/k = 0.2 and 0.8 (L = 10 μm, L_0 = 2 nm, D_{s1} = 2.3, D_{s2} = 2.5, $G_1 = 2.109 \times 10^{-5}$ nm, $G_2 = 1.055 \times 10^{-4}$ nm, E = 129.8 GPa, S_y = 300 MPa, ν = 0.343, and H = 900 MPa.)

5.4.3 Dependence of Static Coefficient of Friction on Fractal Dimension.

As discussed earlier, the surface topography plays an important role in friction because it controls the dominant deformation mode. In this section, the effect of the fractal dimension on the static coefficient of friction is examined in light of results obtained for D_s = 2.3, 2.4, and 2.5 and either fixed fractal roughness G (Fig. 5.9) or fixed height standard deviation (i.e., rms surface roughness) (Fig. 5.10). The results shown in Fig. 5.9 indicate a decrease of the transition load with the increase of D_s, accompanied by a significant decrease of the load range where low coefficient of friction is obtained. This can be explained by considering the effect of D_s on the surface roughness. For fixed G,

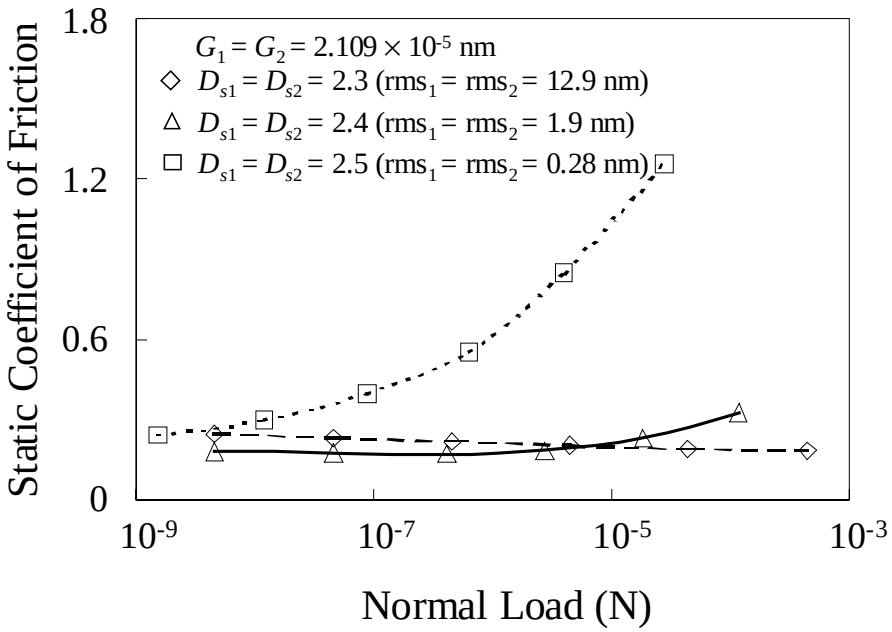

Fig. 5.9 Static coefficient of friction versus normal load for surfaces with fractal dimension D_{s1} and D_{s2}, height standard deviation rms_1 and rms_2, and fractal roughness $G_1 = G_2 = 2.109 \times 10^{-5}$ nm (L = 10 μm, L_0 = 2 nm, E = 129.8 GPa, S_y = 300 MPa, ν = 0.343, H = 900 MPa, and τ/k = 0.8.)

because, in general, $2r_p' \geq L_0 > G$, Eq. (5.25) shows that the roughness amplitude decreases with the increase of D_s, implying an increase in the effective radius of curvature of the asperities with a given truncated contact area (Eq. (5.26)). Since these asperity contacts are more likely to deform elastically and, thus, produce a lower mean contact pressure than plastic contacts, higher static coefficient of friction is produced for fixed interfacial shear strength, despite the relatively lower height standard deviation ($rms_1 = rms_2 = 0.28$ nm) of the surfaces with higher D_s.

Figure 5.10 shows the effect of the fractal dimension on the variation of the static

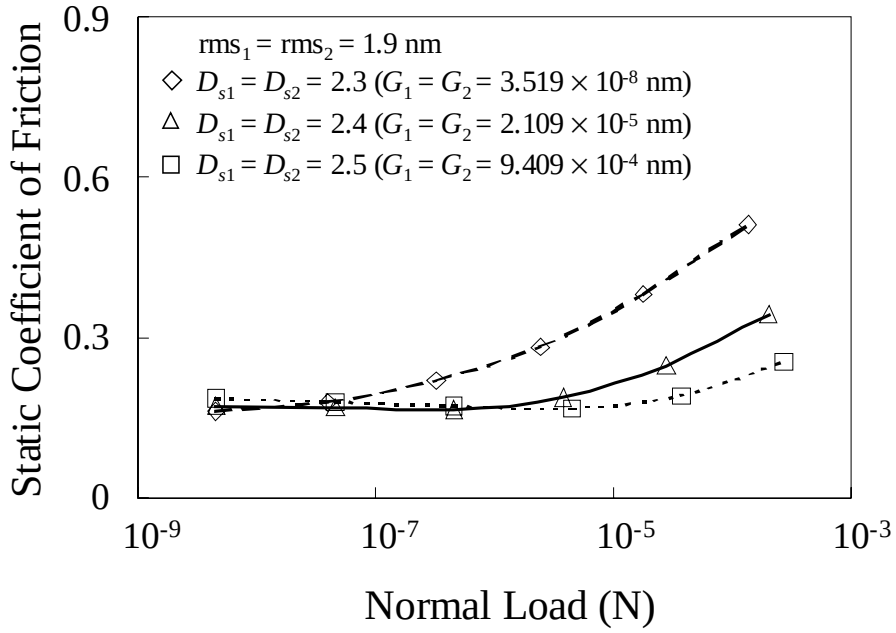

Fig. 5.10 Static coefficient of friction versus normal load for surfaces with fractal dimension D_{s1} and D_{s2}, fractal roughness G_1 and G_2, and height standard deviation $rms_1 = rms_2 = 1.9$ nm ($L = 10$ μm, $L_0 = 2$ nm, $E = 129.8$ GPa, $S_y = 300$ MPa, $\nu = 0.343$, $H = 900$ MPa, and $\tau/k = 0.8$.)

coefficient of friction with normal load for fixed height standard deviation. The fractal roughness was adjusted according to the value of the fractal dimension in order to obtain the same height standard deviation in all simulation cases. It can be seen that the transition load increases and the static coefficient of friction in the high-load range decreases with the increase of D_s. Hence, low coefficient of friction is obtained over a larger load range. This effect of the fractal dimension on the static coefficient of friction is opposite to that shown in Fig. 5.9, and can be attributed to the dominance of the high-frequency components (small wavelengths) of the fractal surfaces characterized by a high D_s value, which increases the number density of small (plastic) asperity contacts under a

given normal load (Eq. (5.12)). Hence, the decrease of the static coefficient of friction in the high-load range when D_s increases is due to the increased contribution of the plastically deformed smaller asperity contacts.

The numerical results presented in this section illustrate the important role of the normal load, interfacial condition, and surface topography on the static coefficient of friction and the dominant deformation mode of the asperity contacts. The analysis is based on a contact mechanics theory of isotropic rough surfaces developed for (a) piece-wise power-law contact size distribution, (b) normal contact slope distribution, (c) negligible asperity interaction, (d) constant interfacial shear strength, and (e) asperity normal load and contact area (at the inception of sliding) approximately equal to those obtained from pure normal contact at the same interference (when both asperities deform elastically or the contact opposes the onset of relative movement) or negligible (when at least one of the asperities deforms plastically and separation tends to occur at the inception of sliding). The present numerical model is suitable for lightly loaded contact interfaces, such as those of magnetic storage disk drives and miniaturized electromechanical devices. The analysis can be extended to include pressure-dependent interfacial shear strength and modified to yield estimates of the lateral displacement at the inception of microscopic sliding by including in the contact mechanics model the effect of asperity bulk deformation on the local slip distance. The new approach for estimating the slope distribution and the modified contact size distribution rule developed in this chapter can be used in contact analyses dealing with various interfacial phenomena, such as adhesion and electrical contact resistance between rough surfaces, where accurate

description of the real contact area in terms of scale-independent topography parameters and mechanical properties is imperative.

5.5 Conclusions

A contact mechanics theory of static friction based on a fractal description of the surface topography and a new approach for estimating the contact slope distribution was presented for isotropic rough surfaces. A modified contact size distribution, an elastic-fully plastic asperity contact model, and a simple static friction mechanism were implemented in the analysis. Numerical results illustrated the dependence of the static coefficient of friction on normal load, interfacial shear strength, and fractal parameters. In view of these results, the following conclusions can be drawn.

(1) The static coefficient of friction decreases gradually to a minimum and then increases with the increase of the normal load. The load corresponding to the minimum static coefficient of friction (transition load) signifies the transition from plastic to elastic dominant deformation at the asperity contacts. The magnitude of the transition load depends strongly on the surface topography through the fractal parameters.

(2) The interfacial shear strength exhibits a strong effect on the static coefficient of friction. Significantly lower friction is obtained with contact interfaces exhibiting low shear strength. In the low-load range (i.e., below the transition load), the variation of the static coefficient of friction with the normal load is independent of interfacial shear strength.

(3) For fixed fractal roughness, higher fractal dimension produces higher static coefficient of friction at relatively high normal loads. However, an opposite trend

occurs for fixed height standard deviation. These effects of the surface topography on the static friction behavior are related to the dominance of elastic and plastic deformation at the asperity contacts.

(4) The effects of the normal load and fractal parameters on the friction behavior indicate that the coefficient of friction is not an intrinsic material parameter. Instead, it represents a global indicator of the relative contributions of elastic and plastic deformation at the asperity contacts.

CHAPTER 6

A Molecular Dynamics Analysis of Surface Interference and Tip Shape and Size Effects on Atomic-Scale Friction

6.1 Introduction

Recent advances in nanotechnology have increased the demand for fundamental understanding of material behaviors at the nanoscale. Despite numerous theoretical and analytical studies on the mechanical response of solid surfaces subjected to various contact loads (Johnson, K. L., 1985), the majority of the earlier studies have been based on continuum mechanics approaches that cannot be applied at the atomic scale. Molecular dynamics (MD) is a powerful computational method for studying nanoscale surface phenomena and instantaneous material properties. Landman et al. (1990) performed MD simulations and atomic force microscopy (AFM) experiments with a nickel tip indenting a gold substrate and reported a "jump-to-contact" phenomenon as the tip approached the substrate surface and elongation of a connective neck during the withdrawal of the tip. MD indentation simulations by Kallman et al. (1993) revealed a transformation from diamond to amorphous structure in the near-surface region of crystalline silicon. MD simulations of a copper substrate indented by a rigid tip performed by Leng et al. (2000) showed that the elastic stress field exhibited similarities with that predicted by the Hertz theory. Komvopoulos and Yan (1997b) investigated the dynamic response of metal-like substrates due to single and repeated indentation by metal-like and diamond-like tips and observed that the deformation behavior of the metal-like substrate indented by the diamond-like tip resembled cyclic softening. Such

material behaviors are not observed in macroscopic studies and cannot be analyzed by continuum mechanics theories.

In addition to the mechanical response of materials at the atomic level, significant efforts have been devoted to study friction and wear behaviors at the atomic and molecular levels. Belak and Stowers (1992) developed MD models for indentation and scratching of a single-crystal copper substrate by a conical diamond tip and estimated the coefficient of friction to be approximately equal to one. MD simulations by Harrison et al. (1992) demonstrated directional anisotropy in the friction behavior of sliding diamond surfaces. In another MD study by Harrison et al. (1993), a weaker friction dependence on the sliding direction was observed when methyl groups were used to replace some of the surface hydrogen atoms (Harrison et al., 1993). Zhang and Tanaka (1997) performed two-dimensional MD simulations of a cylindrical tip with diamond-like material properties and crystal structure different from that of diamond interacting with a copper substrate and reported the occurrence of no-wear, adhesion, plowing, and cutting deformation regimes. Using a relatively large substrate in order to avoid boundary effects, the same authors studied two-body and three-body sliding contact between a rigid diamond tip and silicon monocrystals and proposed a new friction law (1998).

MD simulations by Shimizu et al. (1998) revealed atomic-scale stick-slip phenomena similar to those encountered in AFM measurements. Matthey and Hansen (1998) reported a Coulomb-like friction behavior for granular materials. Tamura et al. (1999) investigated the behavior of hydrocarbon thin films confined between two solid surfaces and discovered that slip occurred mainly in the bulk of the films due to the high affinity of the films for the solid surfaces. Komanduri et al. (2000) studied indentation of

an Al(001) substrate by an aluminum-like rigid tip and subsequent scratching in the [100] direction and reported a nearly constant friction coefficient for 5% variation in the *D* parameter of the Morse potential. MD simulations by Zhang et al. (2001) demonstrated that sliding commenced as a result of the simultaneous slip of all contacting atoms when the (friction) shear stress reached the shear strength of the solid.

The previous studies provide important information about atomic-scale deformation behavior of different materials due to indentation and/or sliding contact loadings. However, because of the limited number of atoms (i.e., less than a few thousand) (Landman et al., 1990; Leng et al., 2000; Komvopoulos and Yan, 1997b; Harrison et al., 1992; Harrison et al., 1993; Zhang and Tanaka 1997; Shimizu et al., 1998; Matthey and Hansen, 1998; Tamura et al., 1999; Komanduri et al., 2000; Zhang et al., 2001) and/or high indentation and sliding speeds (e.g., $\geq$ 50 m/s) (Kallman et al., 1993; Belak and Stowers, 1992; Harrison et al., 1992; Harrison et al., 1993; Zhang and Tanaka 1997; Zhang and Tanaka, 1998; Komanduri et al., 2000) used in earlier MD studies to avoid prohibitively long computational times, the reported results may have been biased by boundary and speed effects. Therefore, one of the objectives of this chapter is to evaluate these effects in the context of MD simulation results obtained for different substrate dimensions and indentation/sliding speed. Moreover, the review of the literature revealed significant variations in atomic-scale friction behavior. In some previous studies, friction anisotropies were associated with the dependence of the normal and friction forces on the sliding direction and lattice structure. However, comprehensive MD studies elucidating several important effects, such as those related to the tip shape and size and penetration depth, on the friction behavior have not been reported yet. Consequently, another

objective is to develop a three-dimensional MD model of a diamond-like rigid tip (prismatic or pyramidal) indenting and sliding over a crystalline copper-like substrate. Simulation results are presented in order to illustrate the dependence of the normal and friction forces on the tip-substrate interference and the variation of the friction coefficient with the size, shape, and orientation of the sliding diamond tip.

6.2 Molecular Dynamics Model

Although useful insight into atomic-scale friction of diamond/copper systems has been obtained from previous two-dimensional MD studies (e.g., Zhang and Tanaka, 1997), three-dimensional MD models yield more realistic deformation behaviors. In this study, the three-dimensional MD code developed by Komvopoulos and Yan (1997b) was modified according to the objectives of the present analysis. Figure 6.1 shows the initial atomic configuration used in some simulations. The figure shows a face-centered-cubic (FCC) copper-like substrate with (001) free surface and a prismatic diamond tip. The substrate has a size of $24a_s \times 18a_s \times 10a_s$, where a_s is the substrate lattice dimension, and consists of 19,037 atoms. To enhance the distinction of each atomic layer, substrate atoms are shown sequentially in gray and black color. The movement of the atoms on the vertical and bottom boundaries of the substrate was fully constraint, as shown in Fig 6.2(a), while the movement of all other atoms obeyed Newton's law. The initial positions of the substrate atoms were set according to the assumed FCC structure, and the initial velocities of the dynamic atoms were assigned randomly from a finite interval (Komvopoulos and Yan, 1997b). Numerical integration of the equations of motion was

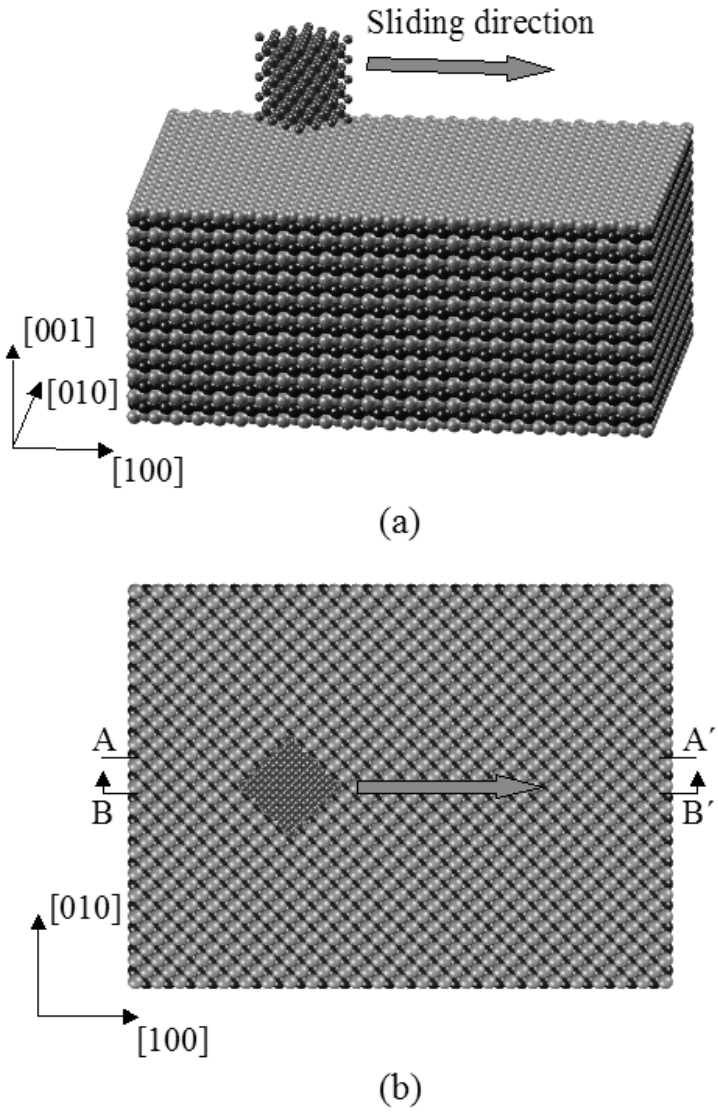

Fig. 6.1 (a) Three-dimensional representation and (b) top view of initial atomic configuration of a $24a_s \times 18a_s \times 10a_s$ FCC copper-like substrate and a $3a_t \times 3a_t$ square-base prismatic diamond tip used in some simulations. Sliding was simulated along the [100] direction with the tip edge in the front.

performed with a fifth-order predictor-corrector algorithm using a constant time step of 2 fs. The forces between the substrate atoms were derived from the Morse potential,

$$V(r) = De^{-2\alpha(r-r_0)} - 2De^{-\alpha(r-r_0)}, \tag{6.1}$$

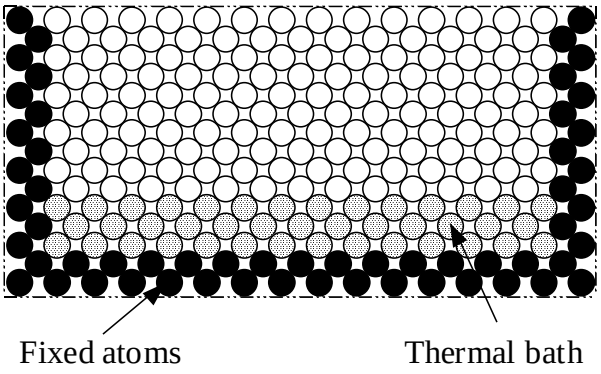

(a)

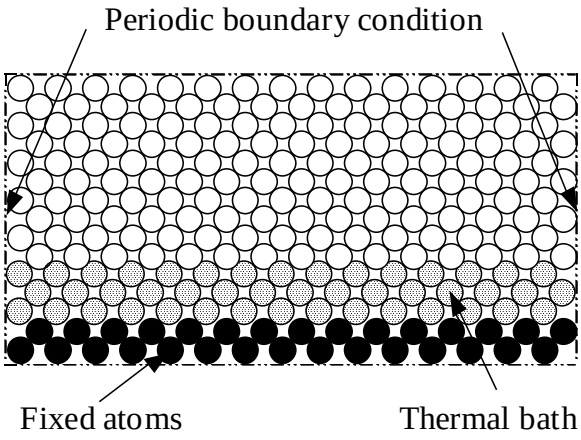

(b)

Fig. 6.2 Schematics showing (a) the boundary conditions (A) used in most simulations and (b) the periodic boundary conditions (B) used to analyze the effects of boundary conditions on the simulation results.

where r is the distance between two atoms and D, r_0, and α are material parameters obtained from Torrens (1972). The forces between the tip and the substrate atoms were determined from the Lennard-Jones potential,

$$V(r) = 4\varepsilon\left[\left(\frac{\sigma}{r}\right)^{12} - \left(\frac{\sigma}{r}\right)^{6}\right]. \tag{6.2}$$

Lorentz-Berthelot mixing rules were used to estimate the values of ε and σ, i.e.,

$$\varepsilon = (\varepsilon_t \varepsilon_s)^{1/2} \text{ and } \sigma = (\sigma_t + \sigma_s)/2, \tag{6.3}$$

where ε_t and σ_t are the Lennard-Jones parameters for the diamond tip obtained from Cheng and Klein (1991), and ε_s and σ_s are similar parameters for the copper substrate obtained by fitting the Lennard-Jones function to a Morse potential, assuming identical potential minima and equal zero-potential distances (Komvopoulos and Yan, 1997b). In view of the significantly higher hardness of diamond than copper, the tip atoms were fully constraint for simplicity. Thus, rigid tips of different shapes and sizes with diamond atomic configurations were used in the MD simulations.

The nominal tip-substrate interference is defined as the penetration depth of the tip measured from the original substrate surface. In the absence of a surface definition at the atomic scale, the tip and substrate surfaces were represented by lines tangent to circles centered at surface atoms with radii equal to the theoretical atomic radii, as proposed by Zhang and Tanaka (1997). Figure 6.3 shows the surface separation and tip-substrate interference, δ, as measured in the present simulations. The side of the square base of the tip is denoted by *w*. The convention is that negative separation denotes positive interference and vice versa.

The MD simulations were performed in three sequential stages. First, the substrate atoms were allowed to reach equilibrium. This was accomplished in 20,000 steps by preventing the substrate atoms from interacting with any external atoms and controlling the substrate temperature, T_0 (= 300 K in all simulations) by direct scaling of the atom velocities (Yan and Komvopoulos, 1998b) and by maintaining the total kinetic

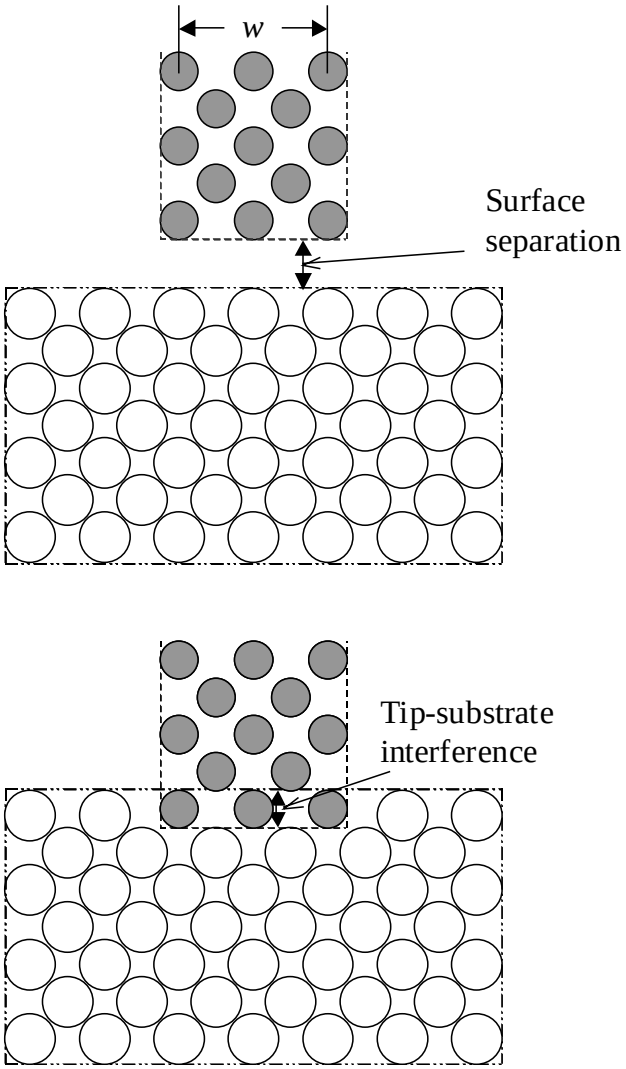

Fig. 6.3 Schematics illustrating the measurement of surface separation and tip-substrate interference for a prismatic diamond tip with square-base width *w*.

energy of the substrate, E_K, equal to $\frac{3}{2}NkT_0$, where N is the number of dynamic substrate atoms, and k is the Boltzmann's constant. After these equilibrium steps, the rigid diamond tip was displaced toward the substrate at a constant speed up to certain

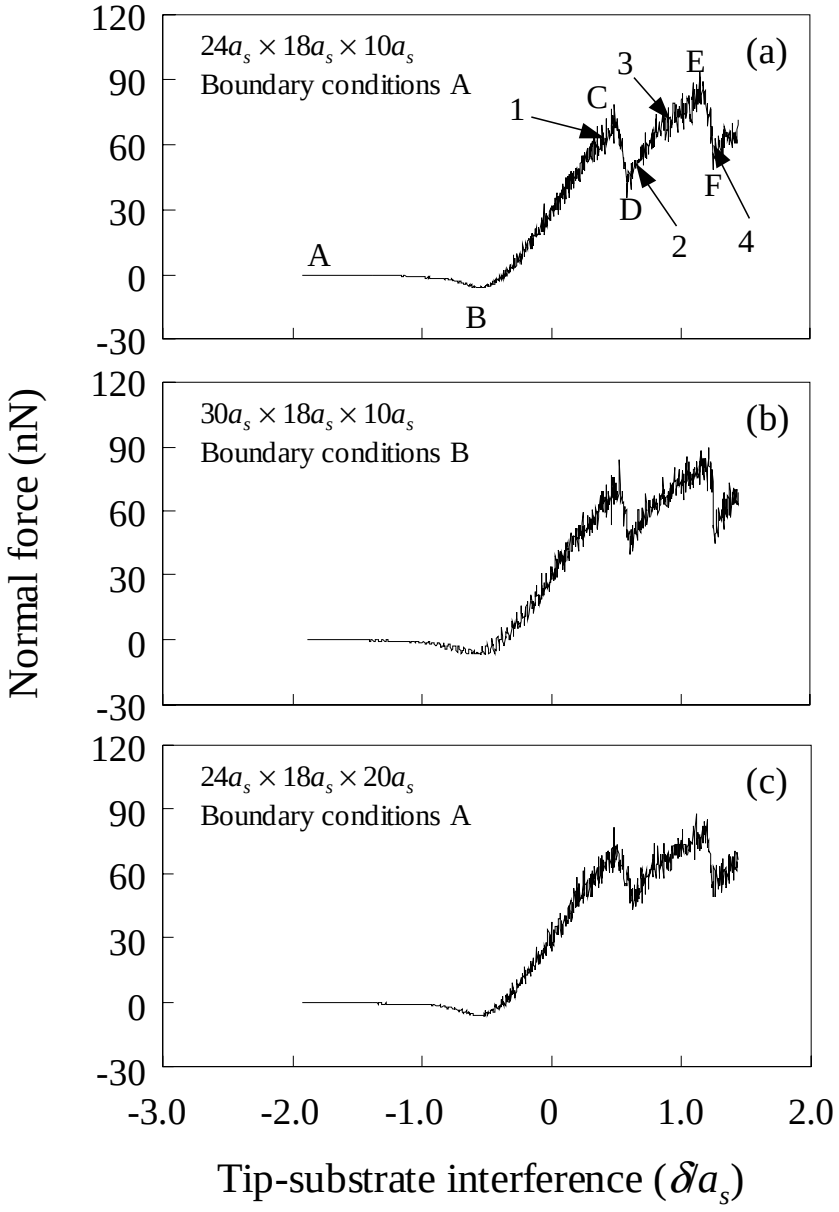

Fig. 6.4 Normal force versus dimensionless tip-substrate interference for a FCC copper-like substrate indented by a $3a_t \times 3a_t$ square-base prismatic diamond tip: (a) $24a_s \times 18a_s \times 10a_s$ substrate with boundary conditions A, (b) $30a_s \times 18a_s \times 10a_s$ substrate with boundary conditions B, and (c) $24a_s \times 18a_s \times 20a_s$ substrate with boundary conditions A. The initial atomic configuration for simulation case (a) is shown in Fig. 6.1.

interference in order to simulate indentation. Finally, sliding was simulated by displacing the tip along the [100] direction of the substrate at constant speed and fixed tip-substrate interference. A thermal bath consisting of three atomic layers near the fixed bottom surface (Fig. 6.2) was used to dissipate the thermal energy generated during indentation and sliding (Yan and Komvopoulos, 1998b). An approach similar to that used in the equilibrium steps was used to control the temperature in the thermal bath.

To examine the effects of the boundary conditions on the MD results, a $30a_s \times 18a_s \times 10a_s$ substrate with periodic boundary conditions (B) (Fig. 6.2(b)) and a thicker substrate ($24a_s \times 18a_s \times 20a_s$) with boundary conditions (A) (Fig. 6.2(a)) were used to simulate both indentation and sliding with the prismatic tip shown in Fig. 6.1. The results were compared to those obtained with the $24a_s \times 18a_s \times 10a_s$ substrate (Fig. 6.1) for boundary conditions A and indentation/sliding speed equal to 5 m/s. Figure 6.4 shows a close similarity between the normal (indentation) force responses predicted by different MD models. Table 6.1 illustrates that the average normal and friction forces obtained

Table 6.1. Average normal and friction forces versus substrate size and boundary conditions for a $3a_t \times 3a_t$ square-base prismatic diamond tip and dimensionless tip-substrate interference $\delta/a_s = 1.44$.

Average force (nN)	Substrate dimensions $24a_s \times 18a_s \times 10a_s$ Boundary Conditions A (Fig. 6.2(a))	$30a_s \times 18a_s \times 10a_s$ Boundary Conditions B (Fig. 6.2(b))	$24a_s \times 18a_s \times 20a_s$ Boundary Conditions A (Fig. 6.2(a))
Normal	34.2	34.0	33.2
Friction	18.4	17.9	18.2

with different substrates and boundary conditions are in good agreement. (The calculation of the average normal and friction forces will be explained later.) In view of the good agreement between the results of the previous MD models and in order to enhance the computational efficiency, all simulation results presented in the following section were obtained with the $24a_s \times 18a_s \times 10a_s$ substrate (Fig. 6.1) subjected to boundary conditions A (Fig. 6.2(a)).

The effect of the sliding speed, V, on the simulation results was also evaluated before proceeding with the main computational study. Figure 6.5 shows the dependence of the average normal and friction forces on the sliding speed. The normal force does not

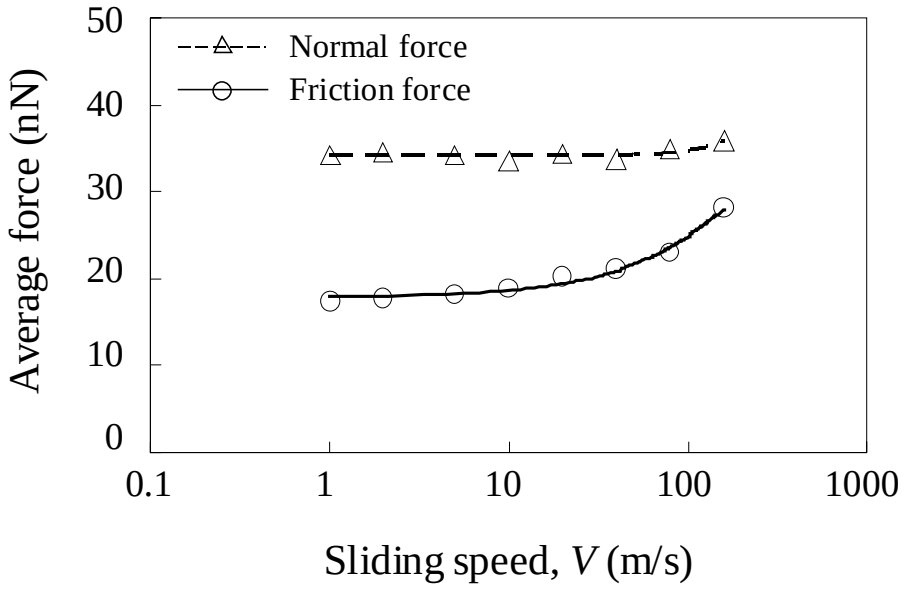

Fig. 6.5 Average normal and friction forces versus sliding speed for a square-base prismatic diamond tip sliding on a FCC copper-like substrate and fixed tip-substrate interference (δ/a_s = 1.44). The initial atomic configuration and sliding direction are shown in Fig. 6.1.

exhibit a speed dependence (for the simulated speed range), while the friction force begins to increase when $V > 10$ m/s. Since a low sliding speed requires significantly more time steps (for convergence, the time step in the present analysis was set equal to 2 fs) to simulate a certain sliding distance and, hence, longer computation time, the simulations discussed in the following section were performed for $V = 5$ m/s. The MD simulations were run on Linux servers with Pentium IV 3.06 GHz processors and 512 MB memory. Depending on the dimensions of the tip and the substrate and the indentation/sliding speed (e.g., see Fig. 6.5), the computational time varied in the range of 2-100 hours of CPU time. For example, in the simulations performed with the model shown in Fig. 6.1 and boundary conditions A (Fig. 6.2(a)), the CPU time for indentation/sliding speed equal to 200 and 1 m/s was approximately equal to 2 and 100 hours, respectively.

6.3 Results and Discussion

6.3.1 Square-base prismatic diamond tip

Indentation and sliding results are presented in this section for a FCC copper-like substrate and a square-base prismatic diamond tip, both possessing {100} contact surfaces. Sliding was simulated along the [100] direction of the substrate with the tip edge in the front, as shown in Fig. 6.1(b). In the following figures, either the tip or the substrate lattice dimension, a_t and a_s, respectively, were used to normalize the length parameters. Figure 6.4(a) shows the variation of the normal force with the dimensionless tip-substrate interference, δ/a_s, due to indentation by a prismatic diamond tip with a bottom surface area equal to $3a_t \times 3a_t$. The initial atomic configuration for this simulation is shown in Fig. 6.1. The high-frequency fluctuations in the force response are due to the thermal vibration of the substrate atoms. As the tip approaches the substrate surface, a

negative (attractive) force is produced, which reaches a maximum at $\delta/a_s = -0.55$. This peak attractive force illustrates a dominant long-range effect of the carbon-copper atomic forces. When the tip moves closer to the substrate surface, the normal force becomes positive (repulsive), illustrating a dominant short-range effect of the interatomic forces. Further advancement of the tip leads to a continuous increase of the repulsive normal force up to a critical interference (point C) at which, the normal force decreases rapidly (point D), indicating the occurrence of irreversible deformation characterized by localized atomic rearrangement and loss of crystallinity. Thereafter, the microstructure modified in the vicinity of the tip deforms only elastically, and the normal force increases again up to a new peak value (point E). At this juncture, additional irreversible deformation occurs, as evidenced from the abrupt decrease of the normal force (point F). This behavior is similar to that reported by Komvopoulos and Yan (1997b) for a metal-like substrate indented by a rigid tip.

Figure 6.6 shows deformed atomic configurations for $\delta/a_s = 0.4$, 0.65, 0.9, and 1.15 (denoted by 1, 2, 3, and 4, respectively, in Fig. 6.4(a)). To facilitate observation of the deformation in the atomic layers adjacent to the surface, only atoms between vertical planes AA′ and BB′ (Fig. 6.1(b)) are shown in Fig. 6.6. For clarity, alternating atomic layers of the substrate are shown in gray and black color, while tip atoms are shown as smaller spheres. For relatively small interference (Fig. 6.6(a)), the crystal structure of the substrate is elastically compressed, and, hence, the normal force is mainly due to interactions between atoms on the flat base of the tip and the first atomic layer of the substrate. However, at greater interferences (Figs. 6.6(b) and 6.6(c)), the crystal structure below the contact region is altered permanently, and some atoms of the top atomic layer

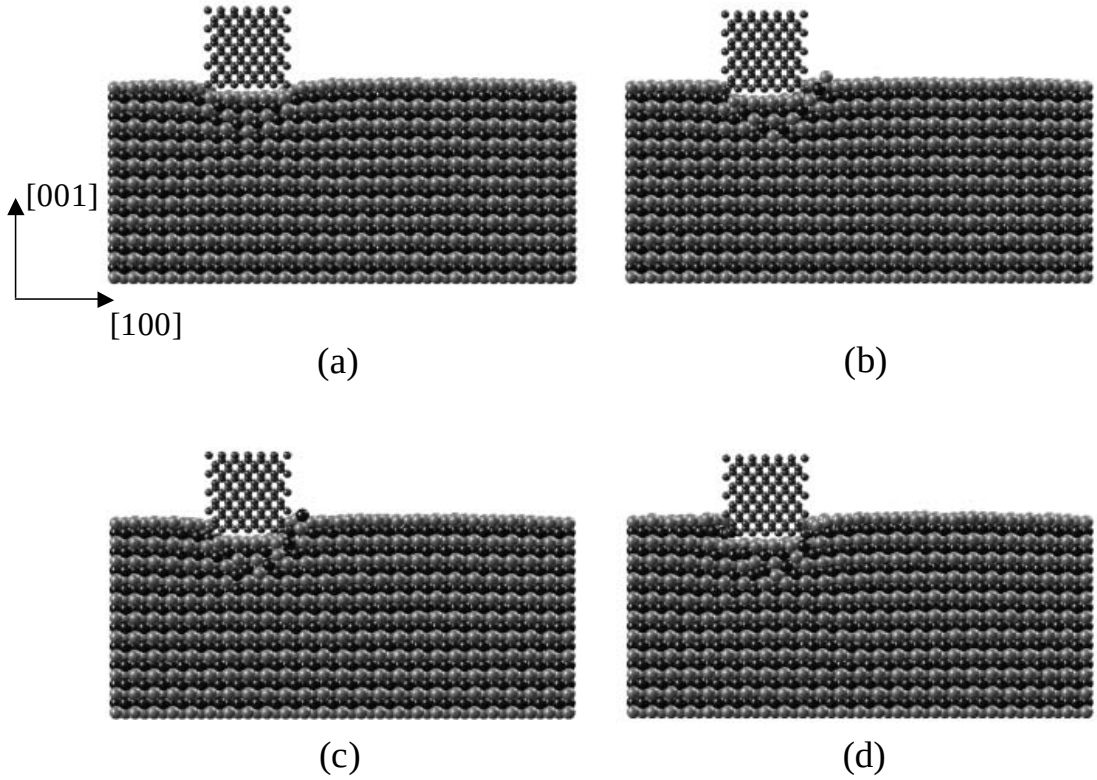

Fig. 6.6 Atomic configurations of a FCC copper-like substrate indented by a square-base prismatic diamond tip for tip-substrate interference equal to (a) $0.4a_s$, (b) $0.65a_s$, (c) $0.9a_s$, and (d) $1.15a_s$. Only atoms between vertical planes AA′ and BB′ (Fig. 6.1(b)) are shown for clarity. The initial atomic configuration and sliding direction are shown in Fig. 6.1.

are displaced towards the underlying atomic layers. The abrupt decrease of the normal force (point D in Fig. 6.4(a)) suggests that irreversible deformation occurred at these interferences. Therefore, the normal force is mainly due to interactions between atoms on the flat base of the tip and substrate atoms of the second atomic layer. At even larger interference (Fig. 6.6(d)), the normal force is mainly due to interactions between atoms on the flat base of the tip and substrate atoms of the third atomic layer.

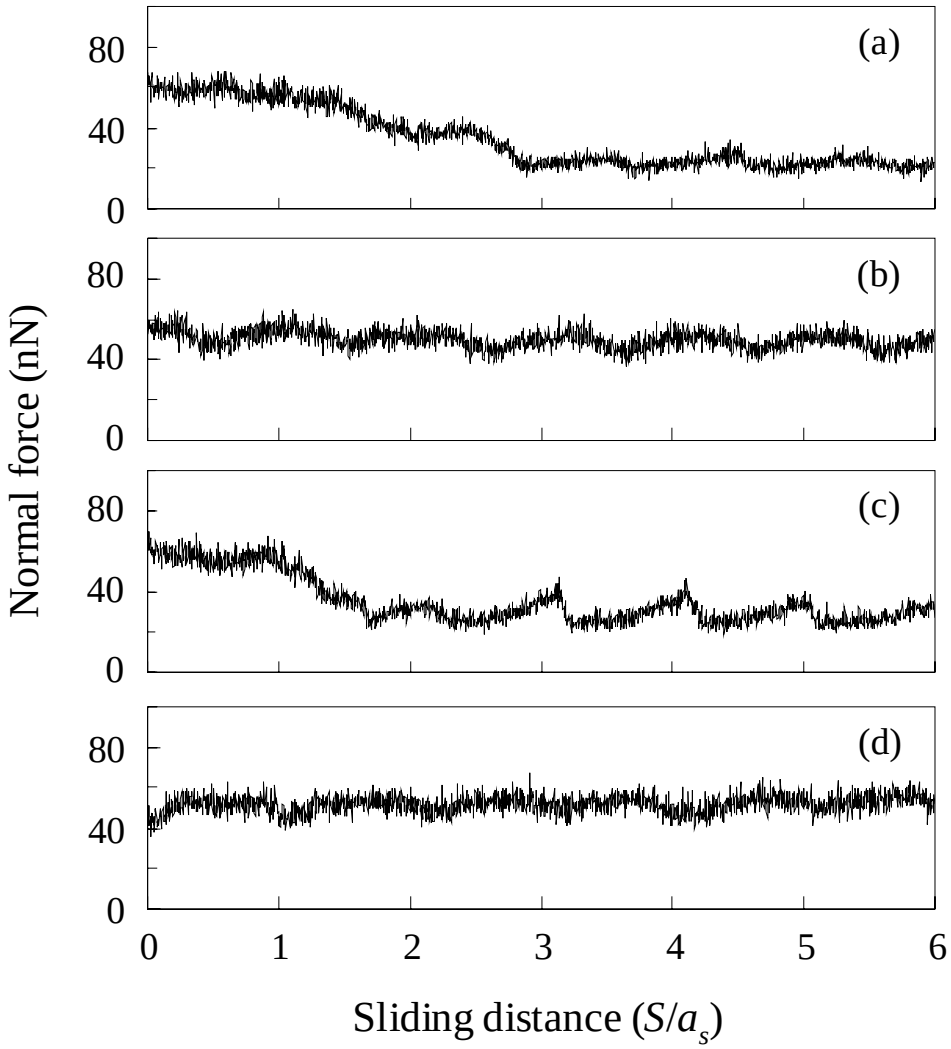

Fig. 6.7 Normal force versus dimensionless sliding distance for a square-base prismatic diamond tip sliding on a FCC copper-like substrate and tip-substrate interference equal to (a) $0.4a_s$, (b) $0.65a_s$, (c) $0.9a_s$, and (d) $1.15a_s$. The initial atomic configuration and sliding direction are shown in Fig. 6.1.

Figures 6.7 and 6.8 show the variation of the normal and friction forces, respectively, with the dimensionless sliding distance, S/a_s, for the previous prismatic tip sliding along the [100] direction of the FCC substrate. Figures 6.7(a) and 6.7(c) show a rapid decrease of the normal force with the increase of the sliding distance ($\delta/a_s = 0.4$ and

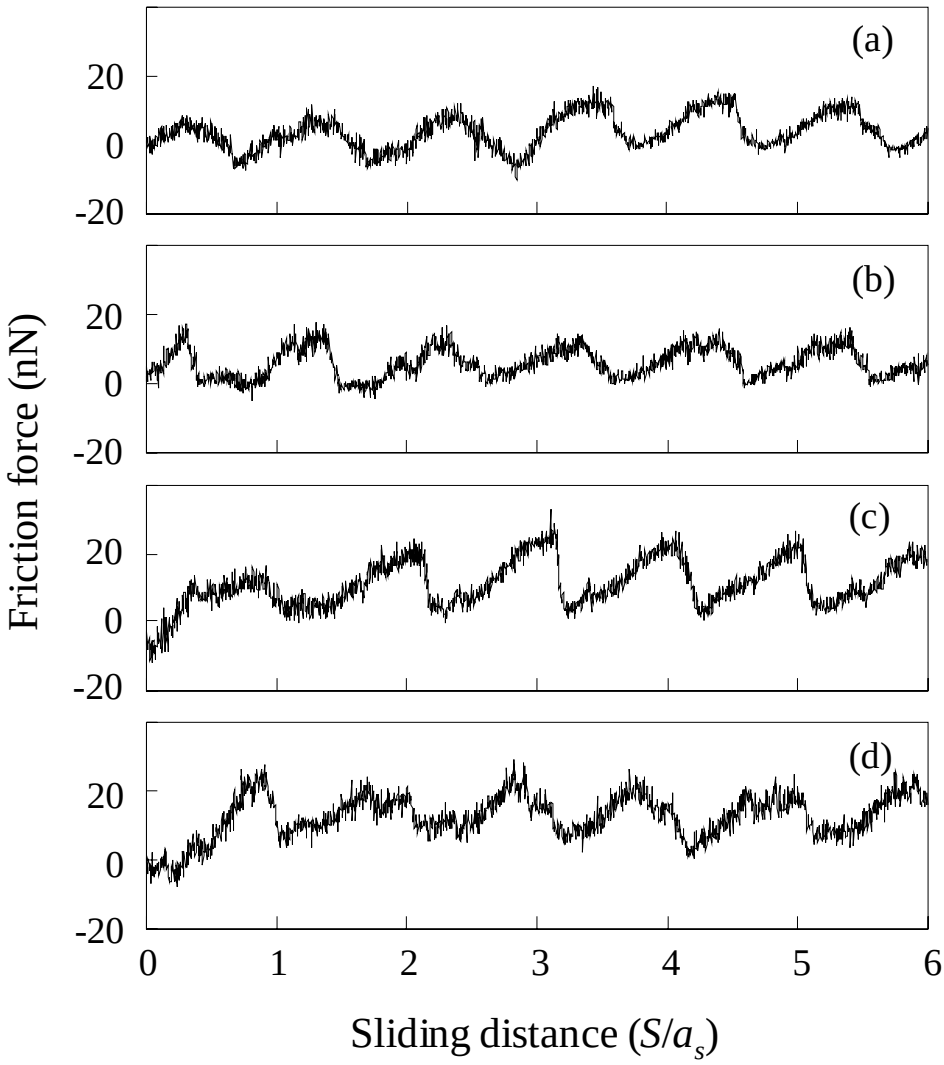

Fig. 6.8 Friction force versus dimensionless sliding distance for a square-base prismatic diamond tip sliding on a FCC copper-like substrate and tip-substrate interference equal to (a) $0.4a_s$, (b) $0.65a_s$, (c) $0.9a_s$, and (d) $1.15a_s$. The initial atomic configuration and sliding direction are shown in Fig. 6.1.

0.9), while Figs. 6.7(b) and 6.7(d) illustrate a periodic fluctuation of the normal force about a constant mean value (δ/a_s = 0.65 and 1.15). Figure 6.8 reveals that a stick-slip behavior occurred in all simulation cases. Similar to the normal force, periodic fluctuation of the friction force occurred after a sliding distance of ~$3a_s$. Hence, the

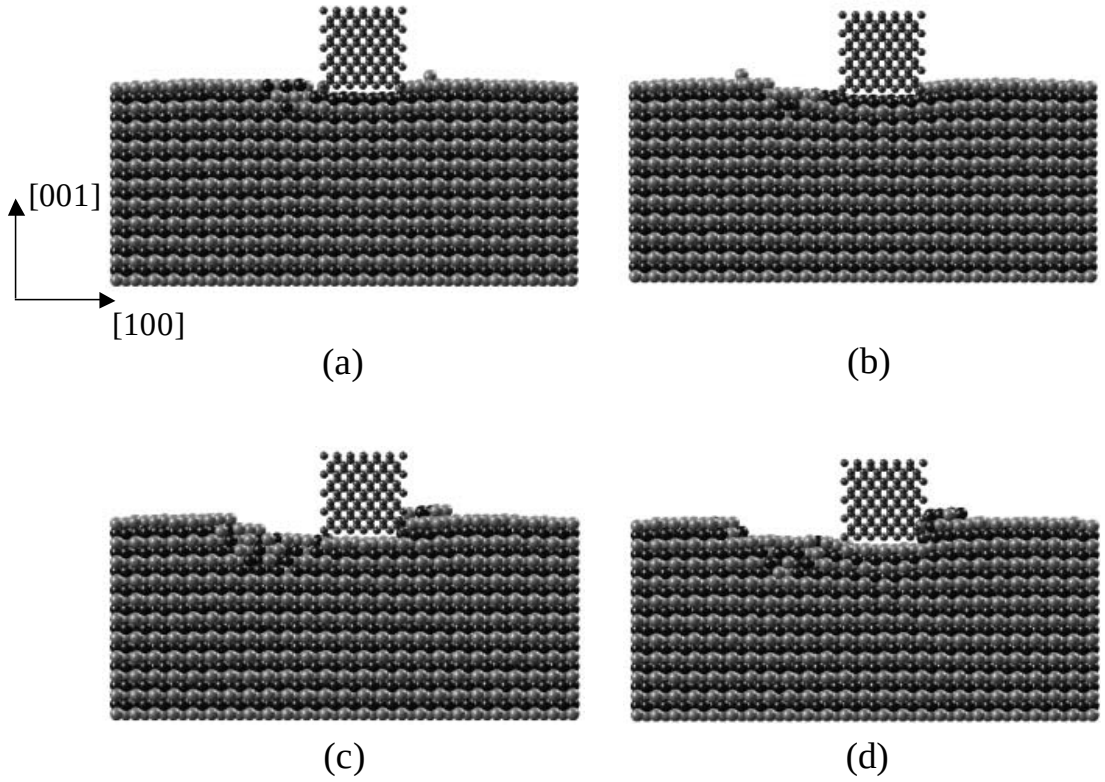

Fig. 6.9 Atomic configurations of a FCC copper-like substrate due to sliding of a square-base prismatic diamond tip for a distance of $6a_s$ and tip-substrate interference equal to (a) $0.4a_s$, (b) $0.65a_s$, (c) $0.9a_s$, and (d) $1.15a_s$. Only atoms between vertical planes AA′ and BB′ (Fig. 6.1(b)) are shown for clarity. The initial atomic configuration and sliding direction are shown in Fig. 6.1.

friction coefficient was estimated as the ratio of the average friction and normal forces calculated in the range of $3 < S/a_s < 6$.

Atomic configurations obtained at the end of sliding of the simulation that yielded the results shown in Figs. 6.7 and 6.8 are presented in Fig. 6.9. Similar to Fig. 6.6, only atoms between vertical planes AA′ and BB′ (Fig. 6.1(b)) are shown for clarity. For δ/a_s = 0.4 and 0.65, sliding resulted in the removal of atoms only from the first atomic layer (Figs. 6.9(a) and 6.9(b)). However, for δ/a_s = 0.9 and 1.15, surface damage was more

severe and atoms were removed from both first and second atomic layers, hence exposing the third atomic layer (Figs. 6.9(c) and 6.9(d)). For the prismatic tip shown in Fig. 6.9, the normal force is mainly due to interactions between atoms on the flat base of the tip and the exposed atomic layer of the substrate. For δ/a_s = 0.4 (0.9), the normal force at the inception of sliding is primarily due to interactions between atoms on the tip base and the first (second) atomic layer of the substrate. However, at the end of sliding, the normal force is mainly due to interactions between atoms on the tip base and the second (third) atomic layer because of the removal of the first (first and second) atomic layer(s), respectively. Since the tip-substrate interference was maintained constant during sliding, the normal force decreased during the initial stage of sliding (Figs. 6.7(a) and 6.7(c)) due to the increase of the distance between tip and substrate atoms resulting from the removal of the first (second) atomic layer. However, for δ/a_s = 0.65 (1.15), the average normal force exhibited less variation during sliding (Figs. 6.7(b) and 6.7(d)) because the exposed atoms resided on the second (third) layer at the inception of sliding (due to plastic deformation of the first (first and second) atomic layer during indentation), and this atomic layer was not removed during sliding.

Figure 6.10(a) shows the variation of the average normal and friction forces with the dimensionless tip-substrate interference. As mentioned earlier, the average normal and friction forces were obtained after sliding by a distance of ~3a_s. These results provide explanation for the tip-substrate interference effect on the force variations shown in Figs. 6.7 and 6.8. The saw tooth-like variation of the normal force can be associated with the removal of different atomic layers. As the tip penetrates the substrate, excessive damage of the outermost atomic layer occurs and, at some critical interference, the sliding tip

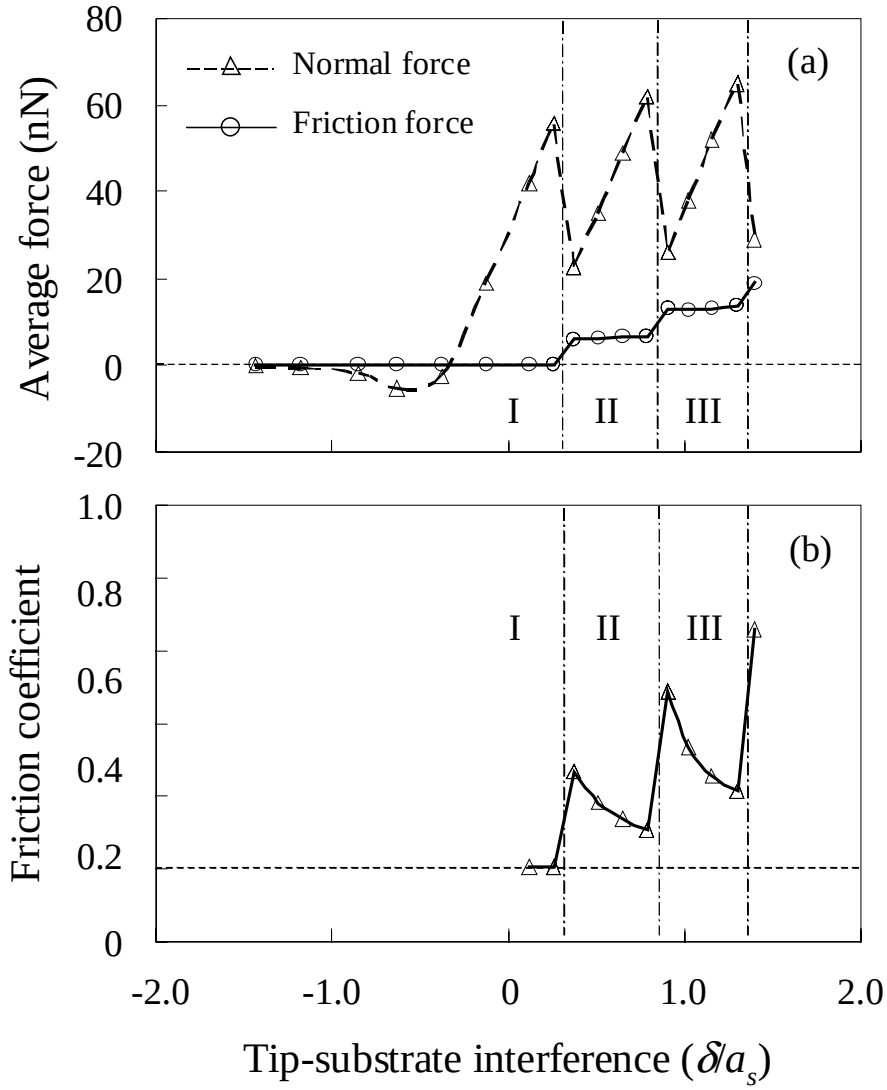

Fig. 6.10 (a) Average normal and friction forces and (b) friction coefficient versus dimensionless tip-substrate interference for a square-base prismatic diamond tip sliding on a FCC copper-like substrate. The initial atomic configuration and sliding direction are shown in Fig. 6.1.

removes atoms from the damaged layer, exposing the underlying atomic layer. Because of the fixed interference, the larger average distance between the exposed atomic layer and the tip base produces a marked decrease in the normal force. This is because the normal force is mainly due to interactions between atoms on the tip base and atoms on

the exposed atomic layer. This phenomenon leads to the development of regimes I, II, and III in Fig. 6.10(a), in which, the normal force exhibits qualitatively similar fluctuations. Compared to the normal force, a very different trend was obtained with the friction force (Fig. 6.10(a)). Examination of the atomic configurations obtained at the end of sliding showed that atoms were not removed from the first atomic layer during sliding in regime I, while in regimes II and III, atoms were removed from the first atomic layer and both first and second atomic layers, respectively. This explains the step-like increase of the friction force in regimes II and III and reveals a strong effect of the number of atomic layers removed during sliding.

Figure 6.10(b) shows the variation of the friction coefficient with the dimensionless tip-substrate interference. The fluctuations of the friction coefficient in regimes II and III are related to those of the normal force in the same regimes (Fig. 6.10(a)). These friction coefficient variations are attributed to the strong dependence of the interfacial forces (especially the normal force) on the distance between atoms on the tip base and atoms of the substrate atomic layer exposed by the prismatic diamond tip.

To examine the tip size effect on the friction behavior, MD simulations were performed with a prismatic diamond tip of square-base area between $a_t \times a_t$ and $5a_t \times 5a_t$. Figure 6.11 shows the variation of the friction coefficient with the dimensionless tip-base size, w/a_t, for δ/a_s = 0.9 and 1.15. In both cases, the friction coefficient decreases with the increase of the tip-base area. This can be explained by considering the strong dependence of the normal and friction forces on the number of atoms on the tip base and the substrate atoms removed by the plowing process, respectively. At the macroscale, these effects are analogous to those of the projected normal and plowing tip areas, respectively. For a

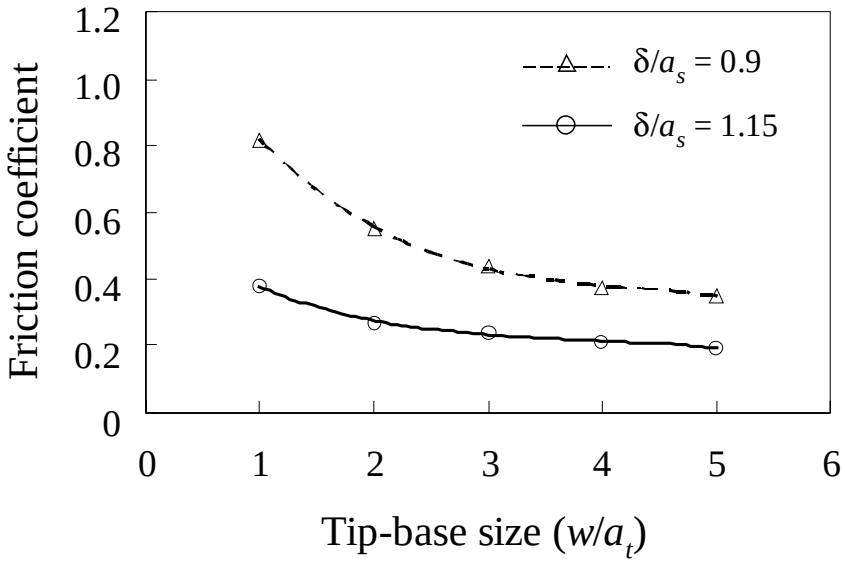

Fig. 6.11 Friction coefficient versus dimensionless tip-base size for edge-front sliding of a square-base prismatic diamond tip on a FCC copper-like substrate. The initial atomic configuration of the substrate and sliding direction are shown in Fig. 6.1.

given tip-substrate interference, the number of atoms on the tip base increases quadratically with the increase of the tip-base size, while the number of substrate atoms removed by the front face of the tip increases linearly. This implies that the increase of the (plowing) friction force is much slower than that of the normal force. In view of the relatively weak adhesion of the diamond/copper system, the adhesion force (that depends strongly on the number of atoms on the tip base) obtained with small prismatic tips is negligible compared to the friction force. Therefore, the increase of the friction force with the tip-base size is much slower compared to the normal force, resulting in lower friction coefficient. The results for δ/a_s = 0.9 and 1.15 show that lower friction coefficients were produced with the increase of the tip-substrate interference. This is a consequence of the

strong dependence of the interfacial forces on the tip-substrate atom distance, which fluctuates due to the removal of atomic layers from the substrate, as discussed previously.

6.3.2 Triangle-base prismatic diamond tip

After discussing the dependence of the friction coefficient on the tip-substrate interference and tip-base size, the effect of the front face of the tip on the friction

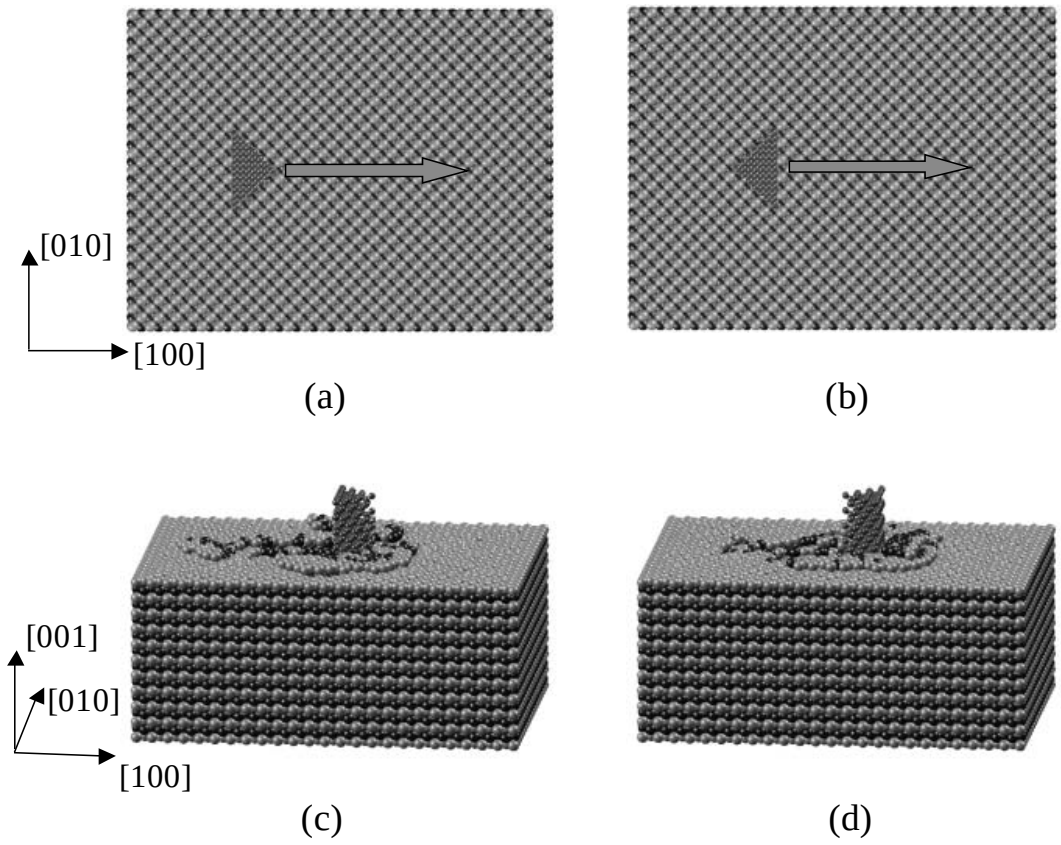

Fig. 6.12 Atomic configurations of a FCC copper-like substrate due to sliding of a triangle-base prismatic diamond tip: (a) and (b) top views of initial atomic configurations in edge- and plane-front sliding simulations, respectively, and (c) and (d) three-dimensional atomic configurations obtained after edge- and plane-front sliding by a distance of $6a_s$ for fixed tip-substrate interference ($\delta/a_s = 1.15$).

coefficient is examined in this section. Sliding simulations were performed with a triangle-base prismatic diamond tip consisting of four {100} surfaces and one {110} surface, and the FCC copper-like substrate used in the previous simulations. The cross section of the tip is a right isosceles triangle with perpendicular sides equal to $3a_t$. Sliding was simulated in the [100] direction with either the symmetric edge or the larger flat surface of the tip plowing the substrate, as shown in Figs. 6.12(a) and 6.12(b). For convenience, simulations performed with these tip orientations will be referred to as edge-front and plane-front sliding, respectively. For a given tip-substrate interference, the two tip orientations yield identical areas normal to the [100] direction, i.e., identical plowing surface areas. Figures 6.12(c) and 6.12(d) show three-dimensional atomic configurations obtained at the end of sliding for δ/a_s = 1.15. It can be seen that substrate atoms piled-up ahead of the tip, especially for plane-front sliding. The increase of the number of substrate atoms interacting with atoms on the front face of the tip intensified the friction force. Table 6.2 gives the average normal and friction forces obtained with

Table 6.2. Average normal and friction forces versus shape and orientation of the diamond tip and dimensionless tip-substrate interference δ/a_s.

Tip-substrate interference δ/a_s	Triangle-base prismatic tip				Square-base prismatic tip	
	Edge-front sliding		Plane-front sliding		Edge-front sliding	
	Normal force (nN)	Friction force (nN)	Normal force (nN)	Friction force (nN)	Normal force (nN)	Friction force (nN)
0.65	38.5	6.5	37.8	7.6	48.9	6.7
0.90	22.1	11.9	21.2	15.1	29.8	12.8
1.15	40.4	12.8	40.2	14.8	53.2	13.2

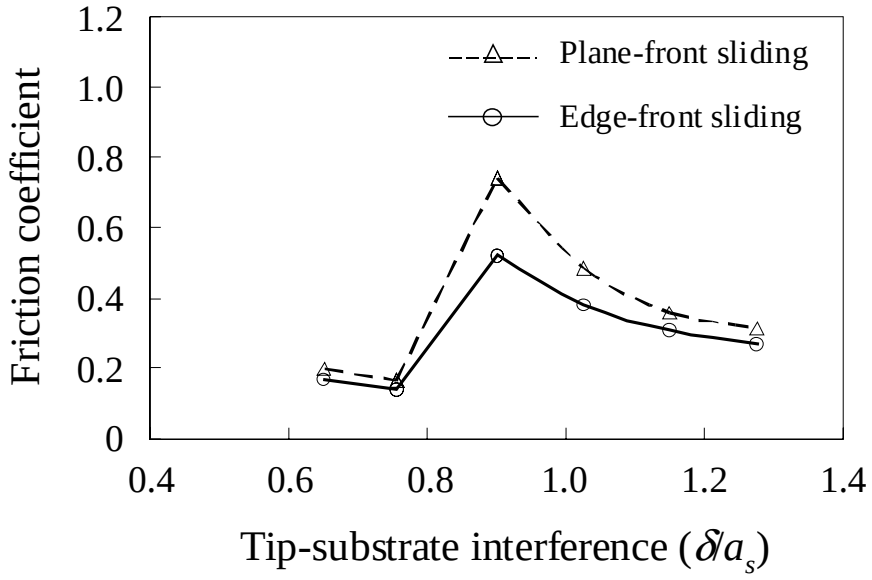

Fig. 6.13 Friction coefficient versus dimensionless tip-substrate interference for plane- and edge-front sliding of a triangle-base prismatic diamond tip on a FCC copper-like substrate. Top views of initial atomic configurations and the sliding direction are shown in Figs. 6.12(a) and 6.12(b).

different tip shapes and orientations in terms of the dimensionless tip-substrate interference. Edge- and plane-front sliding of a triangle-base prismatic tip yielded fairly similar normal forces. The higher friction forces produced from plane-front sliding than edge-front sliding suggest higher energy dissipation for plane-front sliding.

Figure 6.13 shows the dependence of the friction coefficient on the dimensionless tip-substrate interference for plane- and edge-front sliding. As discussed previously, for fixed interference, edge-front sliding leads to less energy dissipation, and, hence, lower friction force. The significant variation of the friction coefficient with the tip-substrate interference illustrates a strong dependence of atomic-scale friction on the effective distance between atoms on the outermost layers of the tip and the substrate, as discussed

earlier. Table 6.2 shows that the friction forces due to edge-front sliding of triangle- and square-base prismatic ($w = 3a_t$) tips are in fair agreement. This can be attributed to the identical plowing surface areas of the tips and suggests that interactions between atoms on the front face of the tip and substrate atoms dragged by the tip control the magnitude of the friction force. However, higher normal forces were obtained with the square-base tip, apparently due to the larger number of atoms on the tip base controlling the magnitude of the normal force.

6.3.3 Pyramidal diamond tip

To further analyze the friction coefficient dependence on the tip shape, simulations were performed with a pyramidal diamond tip consisting of {110} side surfaces and {100} top surface, shown in the inset of Fig. 6.14. The variation of the normal force with the dimensionless tip-substrate interference reveals significant differences from the indentation response obtained with a square-base prismatic tip (Fig. 6.4(a)) for the same interference range. First, the peak attractive force encountered when the tip is in the proximity of the substrate surface is less than that produced with the prismatic tip (point B in Fig. 6.4(a)). This difference illustrates the significant effect of the number of tip-base atoms on the magnitude of the normal force. Second, the interference at the first inception of irreversible deformation due to indentation by the pyramidal tip (evidenced from the rapid decrease of the normal force) is less than that observed with the prismatic tip. Third, higher peak forces were obtained with the prismatic tip at the first inception of irreversible deformation. The spacing of the abrupt decreases in the normal force is not constant in Fig. 6.14. Due to the sharpness of the pyramidal tip, abrupt damage of the substrate lattices adjacent to the lateral faces of the

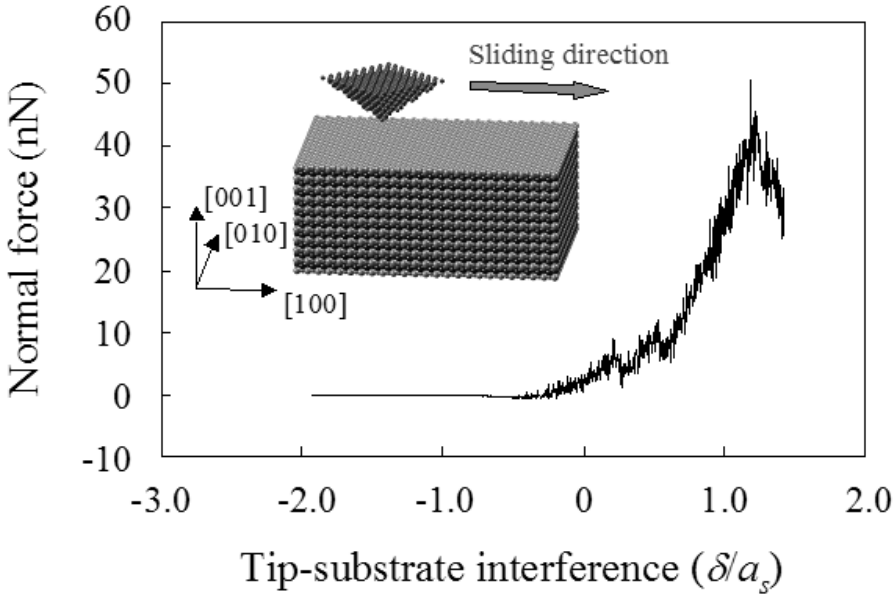

Fig. 6.14 Normal force versus dimensionless tip-substrate interference for a FCC copper-like substrate indented by a pyramidal diamond tip. The initial atomic configuration and sliding direction are shown in the inset of the figure.

tip may occur due to the high stress concentration at the tip apex. Such damage may involve atoms from several atomic layers.

As observed with the prismatic tip (Fig. 6.10(a)), both normal and friction forces obtained with the pyramidal tip demonstrated periodic variations after sliding for several lattice distances. The dependence of the average values of these forces on the dimensionless tip-substrate interference is shown in Fig. 6.15(a). Both forces exhibit similar trends; however, the pronounced force fluctuations observed with the prismatic tip (Fig. 6.10(a)) did not occur with the pyramidal tip. The similar trends in the average force responses seen in Fig. 6.15(a) are due to the fact that the forces produced with the pyramidal tip are manifestations of interactions between atoms on the side surfaces of the

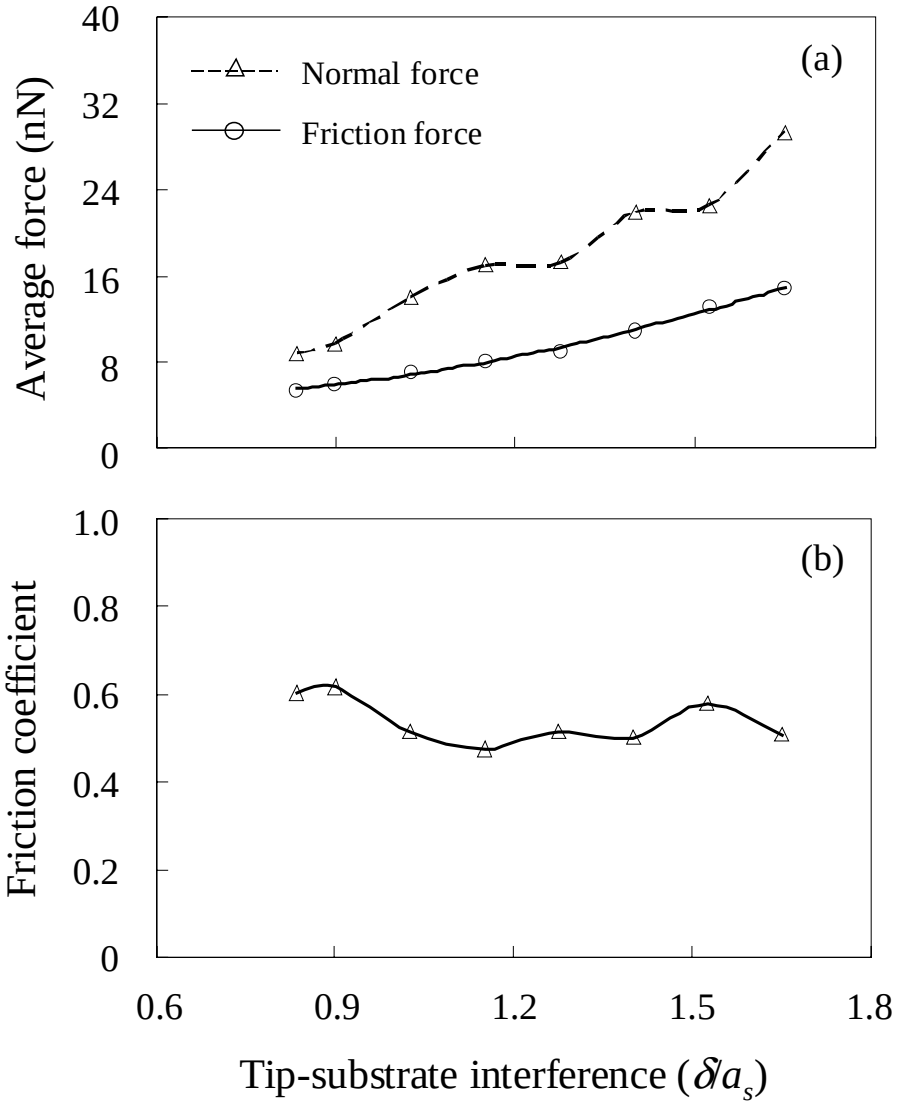

Fig. 6.15 (a) Average normal and friction forces and (b) friction coefficient versus dimensionless tip-substrate interference for edge-front sliding of a pyramidal diamond tip on a FCC copper-like substrate. The initial atomic configuration and sliding direction are shown in the inset of Fig. 6.14.

tip and substrate atoms in the tip vicinity. The relatively smooth change of the forces with increasing interference is associated with the gradually increasing number of atoms removed from different atomic layers. As a consequence, the friction coefficient exhibits less sensitivity to the tip-substrate interference (Fig. 6.15(b)) compared to the prismatic

tip (Fig. 6.10(b)). Zhang and Tanaka (1997) studied scratching of a copper substrate by a cylindrical tip with diamond-like material properties and observed that the coefficient of friction was insensitive to variations in the interference (cutting regime), in accord with the results shown in Fig. 6.15(b). Since the pyramidal and prismatic tips resemble plowing at rake angles of -45° and 0°, respectively, it may be postulated that the tip rake angle may also contribute to the anisotropic friction behavior usually observed at the atomic level.

The results shown in Figs. 6.10(b), 6.11, 6.13, and 6.15(b) demonstrate the important effects of the shape, base size, and front face of the tip and the local interference on the friction coefficient. Thus, atomic-scale friction anisotropies can be related to the dependence of lattice deformation on the aforementioned parameters. The findings of this analysis illustrate that friction at the atomic scale is not an intrinsic material property, as evidenced by the effects of the tip geometry and tip-substrate interference on the friction coefficient. Such dependencies may be associated with friction anisotropies typically encountered at the atomic and molecular levels.

6.4 Conclusions

Molecular dynamics simulations of indentation and sliding were performed with (rigid) diamond tips of different geometries and a copper-like FCC substrate in order to examine the effects of the tip-substrate interference and the shape, size, and front face of the tip on the variation of the friction and normal forces. Based on the presented results and discussion, the following main conclusions can be drawn.

(1) Irreversible deformation due to indentation is not a continuous process. The tip shape and size and the tip-substrate interference control the energy dissipated due to irreversible deformation of the atomic layers adjacent to the surface.

(2) Both normal and friction forces exhibit periodic fluctuations after sliding for several lattice distances. The magnitudes of these forces depend on the intensity of interactions between atoms on the bottom and side surfaces of the tip and substrate atoms below and ahead of the sliding tip.

(3) For a square-base prismatic tip, the spontaneous decrease (increase) of the average normal (friction) force with increasing interference is due to the removal of an atomic layer, while for a pyramidal tip, the relatively smooth change of the average normal and friction forces is a result of the gradually increasing number of atoms removed from different atomic layers.

(4) The effect of the tip-substrate interference on the friction coefficient depends on the tip geometry. For the simulated interference range, higher friction sensitivity on the tip-substrate interference was obtained with a square-base prismatic tip than a pyramidal tip.

(5) The decrease of the friction coefficient with the increase of the base area of the prismatic tip is due to the stronger dependence of the normal force on the tip-base size compared to the friction force.

(6) For a triangle-base prismatic tip, the shape of the front face plays a moderate role on the friction behavior. In general, edge-front sliding yields less energy dissipation than plane-front sliding and lower friction coefficient.

CHAPTER 7

Conclusions

Dynamic contact and friction analyses of homogeneous and/or layered media were performed in this dissertation. The following main conclusions can be drawn from the presented results and discussion.

Impact of a rigid sphere (cylinder) on elastic homogeneous half-space was studied in chapter 2 using dimensional analysis and finite element method. A dimensionless parameter, β, was introduced to account for the effect of wave propagation on the deformation response. For small surface interference ($\beta \leq 1$), the dilatational wave front is confined within the contact region, and the real contact area is equal to the truncated contact area. The contact pressure distribution is uniform, and the mean contact pressure is nearly constant (i.e., insensitive to β). However, for relatively large surface interference ($\beta > 1$), the wave front extends beyond the contact edge, and the real contact area is less than the truncated contact area. The contact pressure distribution is elliptic, and the mean contact pressure increases gradually with the surface interference. For a spherical indenter (axisymmetric analysis), when $\beta \rightarrow \infty$ (i.e., very large surface interference and/or very low indentation speed), the contact pressure distribution approaches the Hertz solution. In the small surface interference regime ($\beta \leq 1$), the stresses, strains, and velocities in the subsurface decrease abruptly in the vicinity of the dilatational wave front, but are nearly uniform in the wake of the wave front. Based on this observation, an approximate energy-based analysis was developed for small surface

interferences. Its validity was confirmed by the good agreement between the results for the strain and kinetic energy of the half-space and the mean contact pressure obtained from this approximate analysis and those obtained from finite element simulations. The analyses were conducted for both axisymmetric (spherical indenter) and plane strain (cylindrical indenter) conditions. The strong resemblance of the results obtained from both analyses for small β ($\beta \leq 1$), together with the fact that the results are independent of the indenter's radius for both analyses, suggests that most results (including contact pressure, subsurface stress, strain and velocity fields and strain and kinetic energy per unit volume) reported for $\beta \leq 1$ are independent of the principal radii of curvature. These results obtained for elastic homogeneous media are also applicable for elastic layered media (and elastic-plastic layered media if plastic deformation does not occur), provided the dilatational wave front resides within the surface layer during the time of dynamic analysis (i.e., small surface interference).

Finite element analysis of dynamic indentation of an elastic-plastic multi-layered medium by a rigid cylinder was performed in order to investigate the dynamic response of layered media for relatively large surface interferences (chapter 3). Sufficiently large meshes were employed such that the faster propagating dilatational waves reflected from the mesh boundaries did not reach the region of interest during the analysis. Hence, the obtained results were independent of mesh size. It was found that the contact load, contact pressure, and subsurface stresses and plastic strains (both loading and residual) intensify with the increase of the indentation depth and speed. For the simulated parameters, higher indentation speed resulted in premature yielding and plastic zone formation in the second (soft) layer and higher tensile stresses in the elastically deformed

surface (hard) layer. A sharper indenter produced a smaller critical indentation depth at the inception of yielding, higher peak contact pressure, lower contact load, and intensified subsurface stress-strain field. Due to the relatively high yield strength of the surface layer, the peak value of the maximum von Mises equivalent stress always occurred in this layer, whereas the peak equivalent plastic strain commenced always in the second layer. Results for the peak values and locations of the maximum von Mises equivalent stress, first principal stress, and maximum equivalent plastic strain, as well as the evolution of the plastic zone during indentation loading and unloading, were obtained in terms of indentation parameters. These results provide insight into the propensity for plastic flow and cracking in dynamically indented multi-layered media.

Simulations of a more realistic case involving an elastic-plastic layered medium in dynamic contact with a rough surface characterized by fractal geometry were presented in chapter 4. An approximate (truncated) Weierstrass-Mandelbrot function was used to describe the two-dimensional surface profile. Due to computational limitations, plane-strain conditions were assumed throughout the analysis. As anticipated, the dependence of the contact load, contact pressure, and subsurface stresses and plastic strains on indentation depth and speed was found to be similar to that for the dynamic contact of a cylindrical indenter, i.e., in both cases the contact load, pressure, and subsurface stress and strains intensified with the increase of the indentation depth and speed. Results for the maximum von Mises equivalent stress, first principal stress, and maximum equivalent plastic strain revealed that, under the simulated conditions, crack initiation and excessive plastic deformation are more likely to occur at the layer interface below the sharper and/or deeper indenting asperities. It was also shown that a high indentation speed and a

relatively thin surface layer promote the cyclic accumulation of plasticity in the soft second layer, especially in the region adjacent to the interface with the hard surface layer. This implies a higher possibility for crack initiation and delamination in this region, where excessive plastic deformation occurs due to the significant mismatch of the elastic and plastic properties of the two layers.

In chapter 5, static friction between rough surfaces was studied using a mechanics model based on fractal theory. A new approach for estimating the contact slope distribution and a modified contact size distribution were proposed, and a simplified mechanics model for contact and friction analysis was implemented. The numerical results illustrate that the static coefficient of friction decreases initially to a minimum value and then increases gradually with the increase of the normal load. The interfacial shear strength exhibits a strong effect on the static coefficient of friction, and significantly lower friction is produced with interfaces exhibiting low shear strength. At light loads, the static coefficient of friction decreases at the same rate regardless of the magnitude of the interfacial shear strength. For fixed fractal roughness, the increase of the fractal dimension results in higher static coefficient of friction at relatively high normal loads. However, for surfaces with constant surface height variance, higher fractal dimension yielded a lower static coefficient of friction at relatively high normal loads. The dependence of the static coefficient of friction on normal load and topography parameters was attributed to the transition from predominantly plastic to elastic deformation of the asperity contacts.

To study the atomic-scale friction behavior, molecular dynamics simulations of indentation and sliding were performed with (rigid) diamond tips of different geometries

and a copper-like FCC substrate. Irreversible deformation due to indentation was found to be a non-continuous process. The energy dissipation due to irreversible deformation of the atomic layers adjacent to the surface was shown to depend on the tip shape and size as well as the tip-substrate interference. After sliding for a few lattice distances, both normal and friction forces exhibited periodic fluctuations, and the friction coefficient was estimated as the ratio of the average friction and normal forces calculated in this range. The spontaneous decrease (increase) of the average normal (friction) force with increasing interference, observed with a square-base prismatic tip, was attributed to the removal of an atomic layer due to sliding. However, a relatively smooth change of the average normal and friction forces was observed for a pyramidal tip due to the gradual increase of the number of atoms removed from different atomic layers. Consequently, it was concluded that the effect of the tip-substrate interference on the friction coefficient depends on the tip geometry, and for the simulated interference range, higher friction sensitivity on the tip-substrate interference was obtained with a square-base prismatic tip than a pyramidal tip. For a prismatic tip, the friction coefficient decreased with increasing base area because of the stronger dependence of the normal force on the tip-base size than the friction force. The shape of the front surface of the tip played a moderate role on the friction behavior. Usually, edge-front sliding yielded lower friction coefficients than plane-front sliding due to less energy dissipation.

In summary, this dissertation produced comprehensive analyses for a few contact and friction problems. The presented results provide basic understanding of the dynamic response of homogeneous and multi-layered media subjected to contact loads and elucidate the friction behavior at various scales, from the atomic level to macroscopic

levels. This study is relevant to various engineering applications involving repetitive contact and friction, such as head-disk interface in computer hard drive and microelectromechanical systems (e.g. switches, relays, vibromotors, and micromirror displays).

REFERENCES

Aboudi, J., 1977, "The Dynamic Indentation of an Elastic Half-Space by a Rigid Punch," *International Journal of Solids and Structures*, **13**, pp. 995-1005.

Alfredsson, B., and Olsson, M., 2000, "Initiation and Growth of Standing Contact Fatigue Cracks," *Engineering Fracture Mechanics*, **65**, pp. 89-106.

Barenblatt, G. I., 1987, *Dimensional Analysis*, Gordon and Breach Science, New York.

Bedding, R. J., and Willis, J. R., 1973, "The Dynamic Indentation of an Elastic Half-Space," *Journal of Elasticity*, **3**, pp. 289-309.

Bedding, R. J., and Willis, J. R., 1976, "High Speed Indentation of an Elastic Half-Space by Conical or Wedge-Shaped Indentors," *Journal of Elasticity*, **6**, pp. 195-207.

Belak, J., and Stowers, I. F., 1992, "The Indentation and Scraping of a Metal Surface: a Molecular Dynamics Study," *Fundamentals of Friction: Macroscopic and Microscopic Processes*, Singer, I. L., and Pollock, H. M., Eds., Kluwer Academic, The Netherlands, pp. 511-520.

Beltzer, A. I., 1988, *Acoustics of Solids*, Springer-Verlag, Berlin Heidelberg, Germany.

Berry, M. V., and Lewis, Z. V., 1980, "On the Weierstrass-Mandelbrot Fractal Function," *Proceedings of the Royal Society of London Series A*, **370**, pp. 459-484.

Bhushan, B., and Majumdar, A., 1992, "Elastic-Plastic Contact Model for Bifractal Surfaces," *Wear*, **153**, pp.53-64

Brach, R. M., and Dunn, P. F., 1992, "A Mathematical Model of the Impact and Adhesion of Microspheres", *Aerosol Science and Technology*, **16**, pp. 51-64.

Brock, L. M., 1978, "Frictionless Indentation by an Elastic Punch: A Dynamic Hertzian Contact Problem," *Journal of Elasticity*, **8**, pp. 381-392.

Brock, L. M., Georgiadis, H. G., 1994, "Dynamic Frictional Indentation of an Elastic Half-Plane by a Rigid Punch," *Journal of Elasticity*, **35**, pp 223-249.

Burmister, D. M., 1945, "The General Theory of Stresses and Displacements in Layered Systems," *Journal of Applied Physics*, **16**, pp. 89-94, 126-127, and 296-302.

Chang, W. R., Etsion, I., and Bogy, D. B., 1987, "An Elastic-Plastic Model for the Contact of Rough Surfaces," ASME *Journal of Tribology*, **109**, pp. 257-263.

Cheng, A., and Klein, M. L., 1991, "Molecular Dynamics Simulations of Solid Buckminsterfullerenes," *Journal of Physical Chemistry*, 95, pp. 6750-6751.

Cheng, Y.-T., and Cheng, C.-M., 1998, "Analysis of Indentation Loading Curves Obtained Using Conical Indenters," *Philosophical Magazine Letters*, pp. 39-47.

Dhaliwal, R. S., and Rau, I. S., 1970, "Axisymmetric Boussinesq Problem for a Thick Elastic Layer under a Punch of Arbitrary Profile," *International Journal of Engineering Science*, **8**, pp. 843-856.

Faulkner, A., Tang, K. C., Sen, S., and Arnell, R. D., 1998, "Finite Element Solutions Comparing the Normal Contact of an Elastic-Plastic Layered Medium under Loading by (a) a Rigid and (b) a Deformable Indenter," *Journal of Strain Analysis for Engineering Design*, **33**, pp. 411-418.

Gan, L., and Ben-Nissan, B., 1997, "The Effects of Mechanical Properties of Thin Films on Nano-Indentation Data: Finite Element Analysis," *Computational Materials Science*, **8**, pp. 273-281.

Greenwood, J. A., and Tripp, J. H., 1967, "The Elastic Contact of Rough Spheres," *Journal of Applied Mechanics*, **34**, pp. 153-159.

Greenwood, J. A., and Williamson, J. B. P., 1966, "Contact of Nominally Flat Surfaces," *Proceedings of the Royal Society of London Series A*, **295**, pp. 300-319.

Gupta, P. K., and Walowit, J. A., 1974, "Contact Stresses between an Elastic Cylinder and a Layered Elastic Solid," ASME *Journal of Lubrication Technology*, **96**, pp. 250-257.

Harrison, J. A., Colton, R. J., White, C. T., and Brenner, D. W., 1993, "Effect of Atomic-Scale Surface Roughness on Friction: a Molecular Dynamics Study of Diamond Surfaces," *Wear*, **168**, pp. 127-133.

Harrison, J. A., White, C. T., Colton, R. J., and Brenner, D. W., 1992, "Molecular-Dynamics Simulations of Atomic-Scale Friction of Diamond Surfaces," *Physical Review B*, **46**, pp. 9700-9708.

Hertz, H., 1882, "Über die Bierührung Fester Elastischer Körper" ("On the Contact of Elastic Solids"), J. reine und angewandte Mathematik, **92**, pp. 156-171. [For English Translation see *Miscellaneous Papers by H. Hertz*, Eds. Jones and Schott, 1896, Macmillan, London, UK.]

Hisakado, T., 1974, "Effect of Surface Roughness on Contact Between Solid Surfaces," *Wear*, **28**, pp. 217-234.

Johnson, K. L, 1985, *Contact Mechanics*, Cambridge University Press, Cambridge, UK.

Johnson, K. L., 1997, "Adhesion and Friction Between a Smooth Elastic Spherical Asperity and a Plane Surface," *Proceedings of the Royal Society of London Series A*, **453**, pp. 163-179

Johnson, K. L., and Pollock, H. M., 1994, "The Role of Adhesion in the Impact of Elastic Spheres", *Journal of Adhesion Science and Technology*, **8**, pp. 1323-1332.

Kallman, J. S., Hoover, W. G., Hoover, C. G., De Groot, A. J., Lee, S. M., and Wooten, F., 1993, "Molecular Dynamics of Silicon Indentation," *Physical Review B*, **47**, pp. 7705-7709.

Kaye, G. W. C., 1986, *Tables of Physical and Chemical Constants and Some Mathematical Functions*, Longman, New York, NY.

Kennedy, F. E., and Ling, F. F., 1974, "Elasto-Plastic Indentation of a Layered Medium," ASME *Journal of Engineering Materials and Technology*, **96**, pp. 97-103.

King, R. B., and O'Sullivan, T. C., 1987, "Sliding Contact Stresses in a Two-Dimensional Layered Elastic Half-Space," *International Journal of Solids and Structures*, **23**, pp. 581-597.

Komanduri, R., Chandrasekaran, N., and Raff, L. M., 2000, "Molecular Dynamics Simulation of Atomic-Scale Friction," *Physical Review B*, **61**, pp. 14007-14019.

Komvopoulos, K., 1988, "Finite Element Analysis of a Layered Elastic Solid in Normal Contact With a Rigid Surface," ASME *Journal of Tribology*, **110**, pp. 477-485.

Komvopoulos, K., 1989, "Elastic-Plastic Finite Element Analysis of Indented Layered Media," ASME *Journal of Tribology*, **111**, pp. 430-439.

Komvopoulos, K., 1991, "Sliding Friction Mechanisms of Boundary-Lubricated Layered Surfaces: Part II-Theoretical Analysis," *Tribology Transactions*, **34**, pp. 281-291.

Komvopoulos, K., 2000, "Head-Disk Interface Contact Mechanics for Ultrahigh Density Magnetic Recording," *Wear*, **238**, pp. 1-11.

Komvopoulos, K., and Yan, W., 1997a, "A Fractal Analysis of Stiction in Microelectromechanical Systems," ASME *Journal of Tribology*, **119**, pp. 391-400.

Komvopoulos, K., and Yan, W., 1997b, "Molecular Dynamics Simulation of Single and Repeated Indentation," *Journal of Applied Physics*, **82**, pp. 4823-4830.

Komvopoulos, K., and Yan, W., 1998, "Three-Dimensional Elastic-Plastic Fractal Analysis of Surface Adhesion in Microelectromechanical Systems," ASME *Journal of Tribology*, **120**, pp. 808-813.

Komvopoulos, K., and Ye, N., 2001, "Three-Dimensional Contact Analysis of Elastic-Plastic Layered Media with Fractal Surface Topographies," ASME *Journal of Tribology*, **123**, pp. 632-640.

Komvopoulos, K., and Ye, N., 2002, "Elastic-Plastic Finite Element Analysis for the Head-Disk Interface With Fractal Topography Description," ASME *Journal of Tribology*, **124**, pp. 775-784.

Kral, E. R., Komvopoulos, K., and Bogy, D. B., 1993, "Elastic-Plastic Finite Element Analysis of Repeated Indentation of a Half-Space by a Rigid Sphere," ASME *Journal of Applied Mechanics*, **60**, pp. 829-841.

Kral, E. R., Komvopoulos, K., and Bogy, D. B., 1995a, "Finite Element Analysis of Repeated Indentation of an Elastic-Plastic Layered Medium by a Rigid Sphere, Part I: Surface Results," ASME *Journal of Applied Mechanics*, **62**, pp. 20-28.

Kral, E. R., Komvopoulos, K., and Bogy, D. B., 1995b, "Finite Element Analysis of Repeated Indentation of an Elastic-Plastic Layered Medium by a Rigid Sphere, Part II: Subsurface Results," ASME *Journal of Applied Mechanics*, **62**, pp. 29-42.

Landman, U., Luedtke, W. D., Burnham, N. A., Colton, R. J., 1990, "Atomistic Mechanisms and Dynamics of Adhesion, Nanoindentation and Fracture," *Science*, **248**, pp. 454-461.

Leng, Y., Yang, G., Hu, Y., and Zheng, L., 2000, "Computer Experiments on Nano-Indentation: A Molecular Dynamics Approach to the Elasto-Plastic Contact of Metal Copper," *Journal of Materials Science*, **35**, pp. 2061-2067.

Majumdar, A., and Bhushan, B., 1990, "Role of Fractal Geometry in Roughness Characterization and Contact Mechanics of Surfaces," ASME *Journal of Tribology*, **112**, pp. 205-216.

Majumdar, A., and Bhushan, B., 1991, "Fractal Model of Elastic-Plastic Contact Between Rough Surfaces," ASME *Journal of Tribology*, **113**, pp. 1-11.

Majumdar, A., and Tien, C. L., 1990, "Fractal Characterization and Simulation of Rough Surfaces," *Wear*, **136**, pp. 313-327.

Majumdar, A., and Tien, C. L., 1991, "Fractal Network Model for Contact Conductance," ASME *Journal of Heat Transfer*, **113**, pp. 516-525.

Mandelbrot, B. B., 1967, "How Long Is the Coast of Britain? Statistical Self-Similarity and Fractional Dimension," *Science*, **156**, pp. 636-638.

Mandelbrot, B. B., 1975, "Stochastic Models for the Earth's Relief, the Shape and the Fractal Dimension of the Coastlines, and the Number-Area Rule for Islands," *Proceedings National Academy of Sciences*, **72**, pp. 3825-3828.

Mandelbrot, B. B., 1983, *The Fractal Geometry of Nature*, Freeman, New York, NY, pp. 1-83 and 116-118.

Matthey, T., and Hansen, J. P., 1998, "Molecular Dynamics Simulations of Sliding Friction in a Dense Granular Material," *Modelling and Simulation in Materials Science and Engineering*, **6**, pp.701-707.

Montmitonnet, P., Edlinger, M. L., and Felder, E., 1993, "Finite Element Analysis of Elastoplastic Indentation: Part II-Application to Hard Coatings," ASME *Journal of Tribology*, **115**, pp. 15-19.

Pollard, H. F., 1977, *Sound Waves in Solids*, Pion, London, UK.

Rogers, L. N., and Reed, J., 1984, "The Adhesion of Particles Undergoing an Elastic-Plastic Impact with a Surface", *Journal of Physics D – Applied Physics*, **17**, pp. 677-689.

Roy Chowdhury, S. K., and Ghosh, P., 1994, "Adhesion and Adhesional Friction at the Contact Between Solids," *Wear*, **174**, pp. 9-19.

Sahoo, P., and Roy Chowdhury, S. K., 1996, "A Fractal Analysis of Adhesion at the Contact between Rough Solids," *Proceedings of the Institution of Mechanical Engineers, Part J: Journal of Engineering Tribology*, **210**, pp. 269-279

Sahoo, P., and Roy Chowdhury, S. K., 2000, "A Fractal Analysis of Adhesive Friction between Rough Solids in Gentle Sliding," *Proceedings of the Institution of Mechanical Engineers, Part J: Journal of Engineering Tribology*, **214**, pp. 583-595.

Sen, S., Aksakal, B., and Ozel, A., 1998, "A Finite-Element Analysis of the Indentation of an Elastic-Work Hardening Layered Half-Space by an Elastic Sphere," *International Journal of Mechanical Sciences*, **40**, pp. 1281-1293.

Shimizu, J., Eda, H., Yoritsune, M., and Ohmura, E., 1998, "Molecular Dynamics Simulation of Friction on the Atomic Scale," *Nanotechnology*, **9**, pp. 118-123.

Shukla, A., and Rossmanith, H. P., 1986, "Dynamic Photoelastic Investigation of Wave Propagation and Energy Transfer Across Contacts," *Journal of Strain Analysis for Engineering Design*, **21**, pp. 213-218.

Souza, R. M., Mustoe, G. G. W., and Moore, J. J., 1999, "Finite-Element Modeling of the Stresses and Fracture during the Indentation of Hard Elastic Films on Elastic-Plastic Aluminum Substrates," *Thin Solid Films*, **335-336**, pp. 303-310.

Stephens, L. S., Liu, Y., and Meletis, E. I., 2000, "Finite Element Analysis of the Initial Yielding Behavior of a Hard Coating/Substrate System With Functionally Graded Interface under Indentation and Friction," ASME *Journal of Tribology*, **122**, pp. 381-387.

Streator, J. L., 2003, "Dynamic Contact of a Rigid Sphere With an Elastic Half-Space: A Numerical Simulation," ASME *Journal of Tribology*, **125**, pp. 25-32.

Tamura, H., Yoshida, M., Kusakabe, K., Chung, Y.-M., Miura, R., Kubo, M., Teraishi, K., Chatterjee, A., and Miyamoto, A., 1999, "Molecular Dynamics Simulation of Friction of Hydrocarbon Thin Films," *Langmuir*, **15**, pp. 7816-7821.

Torrens, I. M., 1972, *Interatomic Potentials*, Academic Press, New York, NY.

Wall, S., John, W., Wang, H.-C., and Goren, S. L., 1990, "Measurements of Kinetic Energy Loss for Particles Impacting Surfaces", *Aerosol Science and Technology*, **12**, pp. 926-946.

Wang, S., and Komvopoulos, K., 1994, "A Fractal Theory of the interfacial temperature Distribution in the slow silding Regime: Part I: Elastic Contact and Heat transfer Analysis," ASME *Journal of Tribology*, **116**, pp. 812-823.

Webster, M. N., and Sayles, R. S., 1986, "A Numerical Model for the Elastic Frictionless Contact of Real Rough Surfaces," ASME *Journal of Tribology*, **108**, pp. 314-320.

Yan, W., and Komvopoulos, K., 1998a, "Contact Analysis of Elastic-Plastic Fractal Surfaces," *Journal of Applied Physics*, **84**, pp. 3617-3624.

Yan, W., and Komvopoulos, K., 1998b, "Three-Dimensional Molecular Dynamics Analysis of Atomic-Scale Indentation," ASME *Journal of Tribology*, **120**, pp. 385-392.

Yang, J., and Komvopoulos, K., 2004, "Dynamic Indentation of an Elastic-Plastic Multi-Layered Medium by a Rigid Cylinder," ASME *Journal of Tribology*, **126**, pp. 18-27.

Zhang, L., and Tanaka, H., 1997, "Towards a Deeper Understanding of Wear and Friction on the Atomic Scale—A Molecular Dynamics Analysis," *Wear*, **211**, pp. 44-53.

Zhang, L., and Tanaka, H., 1998, "Atomic Scale Deformation in Silicon Monocrystals Induced by Two-Body and Three-Body Contact Sliding," *Tribology International*, **31**, pp. 425-433.

Zhang, L. C., Johnson, K. L., and Cheong, W. C. D., 2001, "A molecular Dynamics Study of Scale Effects on the Friction of Single-Asperity Contacts," *Tribology Letters*, **10**, pp. 23-28.

APPENDIX A

Height and Slope Variances of Fractal Surfaces

A two-dimensional fractal surface profile can be represented by a surface function, $z(x)$, given by (Majumdar and Tien, 1990; Majumdar and Bhushan, 1990),

$$z(x) = A^{(D-1)} \sum_{n=n_{\min}}^{n_{\max}} \frac{\cos 2\pi\gamma^n x}{\gamma^{(2-D)n}}.$$

The power spectrum of $z(x)$, i.e., the Fourier transformation of the autocorrelation function of $z(x)$, is

$$\hat{P}(\omega) = \frac{A^{2(D-1)}}{2} \sum_{n=n_{\min}}^{n_{\max}} \frac{\delta(\omega - \gamma^n)}{\gamma^{2(2-D)n}} \tag{A1}$$

and

$$\hat{P}_c(\omega_c) = \frac{A^{2(D-1)}}{2} \sum_{n=n_{\min}}^{n_{\max}} \frac{\delta(\omega_c - 2\pi\gamma^n)}{\gamma^{2(2-D)n}}, \tag{A2}$$

where ω and ω_c are spatial and circular frequencies, respectively. These discrete power spectrum functions can be approximated by the following continuous functions (Berry and Lewis, 1980):

$$\overline{P}(\omega) = \frac{A^{2(D-1)}}{2\ln\gamma} \frac{1}{\omega^{(5-2D)}} \tag{A3}$$

and

$$\overline{P}_c(\omega_c) = (2\pi)^{2(2-D)} \frac{A^{2(D-1)}}{2\ln\gamma} \frac{1}{\omega_c^{(5-2D)}}. \tag{A4}$$

Therefore, the height and slope variances, $\left\langle (z)^2 \right\rangle$ and $\left\langle (dz/dx)^2 \right\rangle$, respectively, can be calculated from the power spectrum as following:

$$\left\langle (z)^2 \right\rangle = \int_{\omega_{cl}}^{\omega_{ch}} \hat{P}_c(\omega_c) d\omega_c = \int_{\omega_{cl}}^{\omega_{ch}} \frac{A^{2(D-1)}}{2} \sum_{n=n_{\min}}^{n_{\max}} \frac{\delta(\omega_c - 2\pi\gamma^n)}{\gamma^{2(2-D)n}} d\omega_c = \frac{A^{2(D-1)}}{2} \sum_{n=n_{\min}}^{n_{\max}} \frac{1}{\gamma^{2(2-D)n}} \tag{A5}$$

and

$$\left\langle \left(\frac{dz}{dx} \right)^2 \right\rangle = \int_{\omega_{cl}}^{\omega_{ch}} {\omega_c}^2 \hat{P}_c(\omega_c) d\omega_c = \int_{\omega_{cl}}^{\omega_{ch}} \frac{A^{2(D-1)}}{2} {\omega_c}^2 \sum_{n=n_{\min}}^{n_{\max}} \frac{\delta(\omega_c - 2\pi\gamma^n)}{\gamma^{2(2-D)n}} d\omega_c = \frac{A^{2(D-1)}}{2} \sum_{n=n_{\min}}^{n_{\max}} \frac{\left(2\pi\gamma^n\right)^2}{\gamma^{2(2-D)n}}$$

$$= (2\pi)^2 \frac{A^{2(D-1)}}{2} \sum_{n=n_{\min}}^{n_{\max}} \frac{1}{\gamma^{2(1-D)n}}. \tag{A6}$$

Using the approximate continuous power spectrum functions, the following relationships for the height and slope variances were obtained:

$$\left\langle (z)^2 \right\rangle \approx \int_{\omega_{cl}}^{\omega_{ch}} \overline{P}_c(\omega_c) d\omega_c = \int_{\omega_{cl}}^{\omega_{ch}} (2\pi)^{2(2-D)} \frac{A^{2(D-1)}}{2\ln\gamma} \frac{1}{{\omega_c}^{(5-2D)}} d\omega_c$$

$$= (2\pi)^{2(2-D)} \frac{1}{4\ln\gamma} \frac{A^{2(D-1)}}{(2-D)} \left[\frac{1}{{\omega_{cl}}^{2(2-D)}} - \frac{1}{{\omega_{ch}}^{2(2-D)}} \right] = \frac{1}{4\ln\gamma} \frac{A^{2(D-1)}}{(2-D)} \left[\frac{1}{{\omega_l}^{2(2-D)}} - \frac{1}{{\omega_h}^{2(2-D)}} \right] \tag{A7}$$

and

$$\left\langle \left(\frac{dz}{dx} \right)^2 \right\rangle \approx \int_{\omega_{cl}}^{\omega_{ch}} {\omega_c}^2 \overline{P}_c(\omega_c) d\omega_c = \int_{\omega_{cl}}^{\omega_{ch}} (2\pi)^{2(2-D)} \frac{A^{2(D-1)}}{2\ln\gamma} \frac{{\omega_c}^2}{{\omega_c}^{(5-2D)}} d\omega_c =$$

$$= (2\pi)^{2(2-D)} \frac{1}{4\ln\gamma} \frac{A^{2(D-1)}}{(D-1)} \left[{\omega_{ch}}^{2(D-1)} - {\omega_{cl}}^{2(D-1)} \right] = (2\pi)^2 \frac{1}{4\ln\gamma} \frac{A^{2(D-1)}}{(D-1)} \left[{\omega_h}^{2(D-1)} - {\omega_l}^{2(D-1)} \right] \tag{A8}$$

It is noted that ω_c should be used in Eq. (A8) instead of ω that was used by Majumdar and Tien (1990) and Majumdar and Bhushan (1990). Therefore, the slope

variance derived from the equation given in these references differs from that given by Eq. (A8) by a factor of $(2\pi)^2$.

The validity of Eqs. (A7) and (A8) can be demonstrated by examining the simple case of a surface profile represented by a single cosine term (i.e., $n_{max} = n_{min} = m$):

$$z(x) = A^{(D-1)} \frac{\cos 2\pi\gamma^m x}{\gamma^{(2-D)m}}.$$

For this function, the height and slope variances are given by

$$\left\langle (z)^2 \right\rangle = \frac{1}{T}\int_0^T z^2(x)dx = \frac{1}{T}\int_0^T \frac{A^{2(D-1)}}{\gamma^{2(2-D)m}}\left(\frac{1-\cos 4\pi\gamma^m x}{2}\right)dx = \frac{A^{2(D-1)}}{2}\frac{1}{\gamma^{2(2-D)m}}$$

and

$$\left\langle (\frac{dz}{dx})^2 \right\rangle = \frac{1}{T}\int_0^T \left(\frac{dz}{dx}\right)^2 dx = \frac{1}{T}\int_0^T \left(\frac{A^{(D-1)}}{\gamma^{(2-D)m}} 2\pi\gamma^m \sin 2\pi\gamma^m x\right)^2 dx = (2\pi)^2 \frac{A^{2(D-1)}}{2}\frac{1}{\gamma^{2(1-D)m}},$$

where $T = 1/\gamma^m$ is the period of both $z(x)$ and $dz(x)/dx$. The above equations are identical to those obtained from Eqs. (A5) and (A6) for the special case of a surface profile represented by a single cosine function. Therefore, the circular frequency must be used in the relationship of the slope variance (Eq. (A8)).